

Skeletal Muscle's Wobbling Response to Impact in Legged Locomotion: From Macroscopic Work-Loops to Cross-Bridge Mechanics

Von der Fakultät für Wirtschafts- und Sozialwissenschaften der Universität Stuttgart
zur Erlangung der Würde eines Doktors der
Philosophie (Dr. phil.) genehmigte Abhandlung

Vorgelegt von

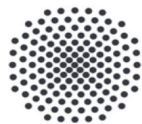
Kasper B. Christensen

aus Graasten (Dänemark)

Hauptberichter: Prof. Dr. Tobias Siebert

Mitberichter: Prof. Dr. Syn Schmitt

Tag der mündlichen Prüfung: 13.04.2022



Universität Stuttgart

*Institut für Sport- und Bewegungswissenschaft
Abteilung für Bewegungs- und Trainingswissenschaft*

2022

Table of Contents

List of Figures	v
List of Tables	vii
List of Symbols and Abbreviations	viii
Abstract	xv
Zusammenfassungxviii
Overview	xxii
1 General introduction	27
1.1 Introduction	27
1.1.1 Aim of Study 1	31
1.1.2 Aim of Study 2	32
1.2 Physiological background	33
1.2.1 Skeletal muscle	33
1.2.1.1 The half-sarcomere	34
1.2.1.2 Sliding-filament theory	35
1.2.1.3 Titin arrangement's within the sarcomere	35
1.2.1.4 Force generation in a half-sarcomere	36
1.2.2 Ischaemia and fatigue	41
1.2.3 Animals used	43
1.3 Mechanical background	44
1.3.1 Criteria for the construction of the frame	44
1.3.2 Theory behind frame	46
1.3.3 Inferring kinematics of a running rat	58
1.3.4 Determining the impact	59

2	Methods	63
2.1	Experimental setup and muscle preparation	63
2.1.1	Schematic diagram of the experimental setup	63
2.1.2	The experimental setup in detail	64
2.1.2.1	High-speed cameras	65
2.1.2.2	Stimulator	66
2.1.2.3	Stroboscopes	67
2.1.2.4	Switch, magnets and DAQ	67
2.1.3	The aluminium frame in detail	68
2.1.4	Ethical approval	70
2.1.5	Preparation of the muscle (GAS)	71
2.1.6	Direct muscle stimulation	74
2.2	Methods (Study 1)	75
2.2.1	Data acquisition, marker tracking, and digital filtering	76
2.2.2	Detecting touch-down (TD) and calculating strain	76
2.2.3	Calculating ΔF , the CE stiffness (K_{CE}), the MTC stiffness (K_{MTC}), and inferring the tendon-aponeurosis-complex stiffness (K_{TAC})	78
2.2.4	Exclusion criteria	82
2.3	Methods (Study 2)	85
2.3.1	Lowering the falling height	85
2.3.2	Determining work-loop	86
2.3.3	Dealing with the non-synchronicity of cameras and the critical choice of the marker on the frame	87
2.3.4	Scaling the MTC and CE findings	92
2.3.5	Model ideas (short version)	94
3	Study 1: strain in shock-loaded skeletal muscle	98

3.1	Results	98
3.2	Discussion	108
3.2.1	The isometric force in isolated muscle	108
3.2.2	Fibre material strain in response to TD	109
3.2.2.1	Young's moduli – a comparison to literature	112
3.2.3	Regional stiffnesses in whole muscle	114
3.2.4	Determining the MTC eigenfrequency	116
3.2.4.1	A reflection on muscle-internal mechanics during impact	118
4	Study 2: dissipative responses and cross-bridge mechanics	121
4.1	Results	121
4.2	Discussion	130
4.2.1	The influence of muscle stimulation on ischaemia	130
4.2.2	ΔF scaled to half-sarcomere level	130
4.2.2.1	Titin's property in passive muscle fibre	132
4.2.3	Wobbling mass findings fitted to two half-sarcomere model ideas	136
4.2.4	Work done in MTC, CE and half-sarcomere	139
4.2.5	The damping coefficient in MTC, CE and half-sarcomere	141
5	Comparing studies: fibre material responses to changes in impact amplitude	144
5.1	Relationship between critical strain and Coulomb force	144
5.2	Fibre strain: a comparison between two falling heights	149
5.3	From quadruped to human locomotion	152
5.3.1	The fibre strain in human GAS	152
6	Conclusion	156

6.1	Study 1	156
6.2	Study 2	158
6.3	Comparing studies	159
6.4	Prospects	160
	Acknowledgements	163
	Appendix	164
	Pictures of experimental setup and muscle	164
	Installation of HCC Control V5.0.0	166
	Static hand-calculations of the frame deflection	168
	Least-square fitting	175
	Model ideas(extended)	178
	Sub-pixel resolution	185
	Radial distances between myosin and actin	187
	Author contributions	188
	List of publications	189
	Declaration of agreement	

List of Figures

Figure 1	Overview of contentxxiv
Figure 1.1	Muscle from macro to micro	38
Figure 1.2	Spacing and dimensions in a sarcomere	39
Figure 1.3	Schematic drawing of a sarcomere	40
Figure 1.4	Muscle tension relative to sarcomere length	41
Figure 1.5	A cantilever beam	47
Figure 1.6	A deflected centerline in a beam	50
Figure 1.7	An example of calculating inertia in a square	54
Figure 1.8	Clamp deflection as response to a static compression	57
Figure 2.1	Schematics of the experimental setup	64
Figure 2.2	Depth of field	66
Figure 2.3	Technical drawing of the C-shaped frame	69
Figure 2.4	Drawing of the experimental frame	79
Figure 2.5	Force change versus displacement of the MTC's COM	81
Figure 2.6	force and length changes of MTC at touch-down	83
Figure 2.7	An example of CE strain inclusion or exclusion	84
Figure 2.8	Isometric force traces in two different falling heights	86
Figure 2.9	Example of noise and delay in frame marker	87
Figure 2.10	An example of time delays effecting the work-loop	89
Figure 2.11	Model ideas for determining cross-bridge stiffness	95
Figure 3.1	Muscle force at TD versus time after muscle extraction	100
Figure 3.2	CE strain and accelerations of COM and frame	102

Figure 3.3	Peak dynamic force change versus isometric force	103
Figure 3.4	Maximum fibre material strain versus isometric force	105
Figure 3.5	Measured stiffness values of MTC and CE	107
Figure 3.6	TAC stiffness (k_{TAC}) in 4 cm trias	108
Figure 4.1	The decline of the isometric muscle force	124
Figure 4.2	Contractile element stiffness (k_{CE})	125
Figure 4.3	CE and MTC: energy dissipated and damping coefficient	128
Figure 4.4	Passive CE and MTC work-loops	129
Figure 4.5	An example of titin contribution in the passive CE	134
Figure 4.6	TAC stiffness (k_{TAC}) in 1 cm trias	141
Figure 5.1	Comparison of stiffnesses calculation methods	146
Figure 5.2	Maximum fibre material strain in study 2 trials	150
Figure 5.3	The fibre material strain response to increasing ΔF	151
Figure 6.1	Experimental setup (frontal view)	164
Figure 6.2	Experimental setup (side view 1)	165
Figure 6.3	Experimental setup (side view 2)	166
Figure 6.4	Side view of the frame	169
Figure 6.5	Frontal view of the aluminium frame	170
Figure 6.6	Frontal view of the aluminium frame	172
Figure 6.7	Model predicted stiffnesses	180
Figure 6.8	Non-linear $F_{CB}(L_{CB})$ (<i>model2</i>)	184
Figure 6.9	Number of myosins in cross-sections of the A-band	187

List of Tables

Table 1.1	Comparison of data for similar size mammals	59
Table 1.2	The data used to infer impulse and impact material . . .	60
Table 2.1	Camera recording inconsistencies	92
Table 3.1	Anatomical data in Study 1	99
Table 4.1	Anatomical data in Study 2	122
Table 4.2	Parameter estimations in <i>model2</i>	126
Table 4.3	Literature data to infer F_{hs}	131
Table 4.4	$F_{hs,max}$ estimations	132
Table 5.1	The Coulomb force's influence on CE strain	148

Symbols and Abbreviations

α	pennation angle, proportionality factor
a	parameter to fit a linear function
A	area, matrix
A^+	Moore-Penrose inverse of matrix A
A^t	transpose of matrix A
$A_{CE,0,max}$	Maximum belly area measured in the anatomical cross-section
$A_{CE,0,min}$	minimum belly area measured in the anatomical cross-section
$A_{CE,avr,0}$	average belly measured for the anatomical cross sectional area
a_{COM}	acceleration of the centre of mass
$a_{COM,max}$	maximum centre of mass acceleration
$ACSA$	anatomical cross-sectional area
a_{frame}	acceleration of frame
A_{hs}	area on an elementary cell
$A_{TAC,0}$	area of the tendon-aponeurosis-complex at touch-down
$A_{tendon,0}$	Tendon in anatomical cross-sectional area
$A_{thigh,max}$	maximum acceleration of the thigh COM after TD
ATS	mean amplitude template step
$A_{shank,max}$	maximum acceleration of the shank COM after TD
β	proportionality factor
b	parameter to fit a linear function
C_1, C_2	added constants for solving integrals
c_1, c_2, c_3	constants assuming the lever arm position to be 7 nm
CE	contractile element
CI	confidence interval

C_{fil}	<i>in-series</i> myofilament compliance
COM	centre of mass
δ	deflection
δ_1	vertical deflection of the frame backbone due to bending
δ_2	vertical deflection of the frame extrusion due to rotation
δ_3	vertical deflection of the part <i>p4</i>
δ_{crit}	critical strain limit in fibre material
ΔF	dynamic force change
ΔF_{hs}	dynamic force change in a half-sarcomere
ΔF_{hum}	dynamic force change in human
ΔG_{ATP}	freed energy available from ATP hydrolysis
ΔL_{CB}	cross-bridge deflection
ΔL_{CE}	contractile element elongation ($L_{CE} - L_{CE,0}$)
ΔL_{MTC}	The COM displacement after TD ($L_{COM} - L_{COM,0}$)
δ_{max}	maximum frame deflection ($\delta_1 + \delta_2 + \delta_3$)
$\delta_{\theta,i}$	deflection due to bending in a structure
d	element, distance, damping, damping coefficient
$d(1, 0)$	elementary cell's interplanar distance
dA	elemental area
DAQ	data acquisition device
d_{CE}	damping coefficient in the contractile element
d_{crit}	critical damping
d_{hs}	damping coefficient in the half-sarcomere
dh, dw	elemental height, elemental width
d_{MTC}	damping coefficient in the muscle-tendon-complex
dt	delta-time
ϵ	strain, grey noise factor

ϵ_x	strain, strain in the x-direction
ϵ_{CE}	strain in the contractile element
$\epsilon_{CE,max}$	maximum dynamic strain
$\epsilon_{GAS,hum}$	GAS CE strain in humans
E	Young's modulus
E_{CE}	Young's modulus in the contractile element
E_{TAC}	Young's modulus in the tendon-aponeurosis-complex
E_{tendon}	Young's modulus in the tendon
f	frequency
F	force
F_1, F_2	forces acting on the frame
F_{CB}	force generated by a cross-bridge ensemble
$F_{CB,1}$	force generated by a single cross-bridge
$F_{CB,max}$	maximum force generated by the cross-bridge ensemble
FEA	finite element analysis
f_{human}	muscular wobbling mass eigenfrequency in humans
F_{hs}	force per half-sarcomere
$F_{hs,max}$	maximum force per half-sarcomere
F_{imp}	impact force
$flex, h$	abbreviation for human <i>m. flexor hallucis longus</i>
$flex, d$	abbreviation for human <i>m. flexor digitorum longus</i>
F_{max}	maximal isometric force of <i>m. gastrocnemius medialis</i> <i>and lateralis</i>
f_{rat}	muscular wobbling mass eigenfrequency in rats
g	gravity
GAS	<i>m. gastrocnemius medialis and lateralis</i>
GAS, <i>l</i>	abbreviation for human <i>m. gastrocnemius lateralis</i>

GAS, m	abbreviation for human <i>m. gastrocnemius medialis</i>
GRF	ground reaction force
h, h_{in}	height, inner height
$hook$	marker on the hook
I, I_z	inertia, inertia of an object rotated around its centroidal z-axis
$ImpIdx$	detecting camera non-synchronicity using TD instant as reference
$insulator$	marker on the insulator
I_{p1}, I_{p2}	inertia in part $p1$, inertia in part $p2$
I_{p3}, I_{p4}	inertia in part $p3$, inertia in part $p4$
I'_z	inertia of an object rotated around a z-axis that is <i>not</i> the centroidal axis
κ	curvature (kappa, not to be confused with k)
k	stiffness
k_{CE}	contractile element stiffness
$k_{CE,hum}$	contractile element stiffness in humans
$k_{CB,1}$	stiffness in a single cross-bridge
$k_{CB,max}$	maximum stiffness of the cross-bridge ensemble
k_{hs}	half-sarcomere stiffness
k_{fil}	myofilament stiffness
k_{MTC}	muscle-tendon-complex stiffness
k_{TAC}	tendon-aponeurosis-complex stiffness $(\frac{1}{k_{CE}} + \frac{1}{k_{MTC}})^{-1}$
k_{tendon}	tendon stiffness
k_{SEC}	serial elastic compartment stiffness
L, L_y	length, length in the y-direction
\dot{L}	velocity
L_1	lever arm for $\Delta l'_{AE}$ in the S1-part of the myosin head, length of frame part

L_2	length part of the frame backbone used to calculate frame deflection
$L_{belly,0}$	Belly length
L_{CB}	lever coordinate (cross-bridge position)
$L_{CB,opt}$	optimal lever coordinate (cross-bridge position)
L_{CE}	vertical distance between two horizontal ranges ($y_u - y_l$)
$L_{CE,0}$	The CE reference length at TD ($y_u - y_l$)
L_{COM}	COM's vertical distance to the frame marker
$L_{COM,0}$	COM's vertical distance to the frame marker at TD
$L_{dist,0}$	Distal tendon length in frame
L_{fil}	length of the myofilament
L_{hs}	half-sarcomere length
$L_{MTC,90^\circ}$	MTC length at 90°
L_{p3}, L_{p4}	length of part $p3$, length of part $p4$
$L_{per}, L_{sol}, L_{tib}$	muscle belly length of human <i>per</i> , <i>sol</i> or <i>tib</i> , respectively
$L_{prox,0}$	Proximal tendon length in frame
$L_{TAC,0}$	tendon length at touch-down
$L_{tendon,0}$	Total tendon length in frame
m	mass, <i>GAS</i> mass
M	bending moment, pixels in a template
M_1, M_2	bending moments in the frame
m_{animal}	animal mass
$MinAcc$	detecting camera non-synchronicity using peak acceleration instant as reference
$MinPos$	detecting camera non-synchronicity using maximum elongation instant as reference
<i>model1</i>	cross-bridge model idea by Fusi <i>et al.</i> (2014) [1]

<i>model2</i>	cross-bridge model idea by Günther <i>et al.</i> (2018) [2]
<i>MTC</i>	muscle-tendon-complex
M_z	bending moment with respect to the z-axis
ω	angular frequency, circular eigenfrequency
n_{CB}	number of cross-bridges
$n_{CB,max}$	maximum number of cross bridges
p	impulse, mass density, momentum
$p1, p2, p3, p4$	the frame separated into parts $p1, p2, p3, p4$, respectively
PCSA	physiological cross-sectional area
<i>per</i>	abbreviation for human <i>m. peroneals</i>
q	proportionality factor
$q_{GAS,l}$	proportionality factor for $L_{GAS,l}$
$q_{GAS,m}$	proportionality factor for $L_{GAS,m}$
r	radius, percentage of $A_{CE,0,max}$ that contains fibre material
σ, σ_x	stress, plane stress perpendicular to x-axis
$S1, S2$	myosin fragment and myosin sub-fragment, respectively
<i>sol</i>	abbreviation for human <i>m. soleus</i>
θ_{p1}, θ_{p2}	angle of rotation in part $p1$, angle of rotation in part $p2$
θ_{p3}, θ_{p4}	angle of rotation in part $p3$, angle of rotation in part $p4$
t	thickness, time
T	period
<i>TAC</i>	tendon-aponeurosis-complex
<i>TD</i>	touch-down
<i>tib</i>	abbreviation for human <i>m. tibialis posterior</i>
t_{rat}	time between TD and the end of one full oscillation of wobbling mass in rat GAS
t_{hum}	time between TD and the end of one full oscillation of

	wobbling mass in human GAS
u	proportionality factor
v	velocity
w	width, work (energy dissipation)
w_{CE}	energy dissipated in the contractile element
w_{hs}	energy dissipated in a half-sarcomere
w_{in}	inner width
w_{MTC}	work (energy dissipation) in the muscle-tendon-complex
x, y, z	rectangular axes (origin at point O)
x	distance from beam tip towards fixation point, length
x_{max}	beam's total length
y	distance, deflection, distance between axis of rotation and nearest limit of dh
y_{COM}	centre of mass position
y_{frame}	position of the frame
y_l, y_u	lower sub-array, upper sub-array
y_{max}	maximum distance to the centreline, maximum deflection in the y-direction
ζ	damping ratio

Abstract

Legged locomotion has evolved into the most common form of terrestrial locomotion. When the leg makes contact with a solid surface, muscles absorb some of the shock-wave accelerations (impacts) that propagate through the body, causing the muscle material to wobble. To improve our understanding of how the superposition of impact shock-waves affects the contractile machinery in the muscle fibre, a custom build C-shaped frame, with isolated rat (*Rattus norvegicus*, Wistar) muscle (*m. gastrocnemius medialis and lateralis*: GAS), was dropped from two different heights (Study 1: 4 cm and Study 2: 1 cm). The frontal area of the muscle was patterned with high-grade steel markers, and high-speed cameras recorded local muscle wobbling to describe fibre internal kinematics by strain. Further, with Newton's second law (force = mass·acceleration), the dynamic force difference between the muscle-tendon-complex ends in response to the impact was used to determine stiffness, damping and energy dissipation in the whole muscle and the fibre material during wobbling after impact.

Only equating the frame to leg bone kinematics, the impact duration of ca. 10–15 ms is practically the same in the hindlimbs of running rats, comparably small mammals, and humans. Peak values of the centre of mass accelerations are also similar for a running rat's GAS $\approx 165 \text{ m s}^{-2}$ and running human's leg muscles (in shank $\approx 270 \text{ m s}^{-2}$ and thigh $\approx 160 \text{ m s}^{-2}$). Yet, the phase relations of the leg's wobbling masses in response to the impact differ. In humans, the maximum vertical accelerations of the segmental muscle masses occur ca. 5 ms (shank) and 20 ms (thigh) after maximum leg bone acceleration. During impacts wobbling mass dynamics have higher functional relevance in larger animals because there is an increasing temporal separation of bone and muscular movement. For a fully active and fresh muscle,

the fibre strain in rat's GAS running at 1 m s^{-1} (Study 1) is 0.2% in response to impact. Accordingly, cross-bridges are bound down to 11.8 N (40% of the maximum isometric muscle force). This is practically the same force boundary value $F = 12 \text{ N}$ found in the stiffness analysis. That is, where the changes in fibre material and the muscle-tendon-complex stiffness characteristics, as a function of the isometric muscle force, saturates. Specifically, the found fibre material stiffnesses decreased from 9050 N m^{-1} to 3700 N m^{-1} , and in the muscle-tendon-complex from 3450 N m^{-1} to 2400 N m^{-1} , from 100% to about 40% of the maximum isometric muscle force.

For an almost constant dynamic force change of 0.2 N across all trials, the energy dissipated by the muscle-tendon-complex at maximum isometric muscle force was $17 \mu\text{J}$, which rose to $50 \mu\text{J}$ in the passive muscle-tendon-complex in one work-loop after ground contact. In all trials, a work-loop encompasses one oscillation period that spans between touch-down (TD) and the instant closest to zero when the wobbling GAS's centre of mass acceleration returns to zero for the second time. For the fibre material, the dissipated energy changed from $3.5 \mu\text{J}$ to $23 \mu\text{J}$ from fully stimulated to passive, respectively. Therefore, a half-sarcomere dissipates from 10.4 zJ to 68 zJ ranging from fresh and fully active to a passive muscle, respectively. At the maximum activity, a single cross-bridge would, thus, dissipate 0.6% of the mechanical work available per ATP split per impact, and up to 16% energy in common, submaximal, activities.

Although the isometric force values in a whole muscle (23 N) scaled to the half-sarcomere (445 pN) is in perfect agreement with similar estimations in single fibre experiments in literature, the half-sarcomere stiffness at maximum isometric muscle force is only 2.2 pN nm^{-1} , which decreased

to 0.4 pN nm^{-1} in a passive half-sarcomere. These low stiffness values are not consistent with simple half-sarcomere model used in single fibre experiments. The discrepancy between the 2.2 pN nm^{-1} and single fibre experiments is most likely because the single fibre experiments (perturbations at 4000 Hz) do not necessarily meet the working conditions of an *in-vivo* half-sarcomere (superimposed oscillations in fibre material caused by the impact are around 50 Hz). Fitting the data with a Coulomb-force model (named *model2*) suggests that the Coulomb-actuating part in the cross-bridge dominates cross-bridge stiffness. The influence of perturbation frequency between experimental and *in-vivo* conditions has been hinted at in literature before. Though never been put into the context of cross-bridge modelling.

Two model assumptions were used to assess titin's contribution in passive fibre material: first, that titin is solely responsible for the passive half-sarcomere stiffness with the sub-cases of being elastic or visco-elastic. If being elastic, then titin accounts for 75% of the work-loop stiffness. In the sub-case of visco-elasticity, titin accounts for 50% of the dissipated energy in a half-sarcomere. The second model assumption is that titin makes up the half-sarcomere stiffness partly in conjunction with myosin filament. For the latter, the scaled titin stiffness equals the elongation slope in the fibre material work-loop and 100% of the dissipated energy in a passive half-sarcomere if titin is visco-elastic.

Scaling the fibre strain values from rat GAS to human GAS suggests that the passive properties have a more dominant role in limiting the fibre strain in human GAS when sprinting. The fibre strains in human GAS fibre material is likely higher than in rat because the difference in the dynamic force change between humans and rats is much higher than the difference in the anatomical cross-sectional area between the two species.

Zusammenfassung

Der Gang auf Beinen hat sich zur häufigsten Form der terrestrischen Fortbewegung entwickelt. Wenn ein Bein auf einer festen Oberfläche aufkommt, absorbieren die Muskeln einen Teil der Stoßwellenbeschleunigungen (Impacts), die sich durch den Körper ausbreiten, wodurch das Muskelmaterial schwingt. Um unser Verständnis davon zu verbessern, wie sich die Überlagerung von Stoßwellen auf die kontraktile Maschinerie in der Muskelfaser auswirkt, wurde ein speziell angefertigter C-förmiger Rahmen zusammen mit einem isolierten Rattenmuskel (*Rattus norvegicus*, Wistar, *M. gastrocnemius medialis und lateralis*: GAS) aus zwei verschiedenen Höhen (Studie 1: 4 cm und Studie 2: 1 cm) fallen gelassen. Am vorderen Bereich des Muskels wurde ein Muster aus Edelstahlmarkern angebracht, und Hochgeschwindigkeitskameras nahmen die lokalen Muskelschwingungen auf, um die interne Kinematik der Fasern infolge des Impact zu beschreiben. Weiterhin wurde mit dem zweiten Newtonschen Gesetz (Kraft = Masse · Beschleunigung) die dynamische Kraftdifferenz zwischen den Muskel-Sehnen-Komplex-Enden als Reaktion auf den Aufprall verwendet, um aus der Muskelschwingung nach dem Aufprall die Steifigkeit, Dämpfung und Energiedissipation im gesamten Muskel, und im Fasermaterial zu bestimmen.

Setzt man die Kinematik von Rahmen zu Beinknochen gleich, ist die Aufpralldauer von ca. 10-15 ms praktisch gleich derer in den Hinterbeinen von laufenden Ratten, anderen kleinen Säugetieren und Menschen. Spitzenwerte der Schwerpunktbeschleunigungen sind auch ähnlich zwischen dem GAS einer laufenden Ratte $\approx 165 \text{ m s}^{-2}$ und dem eines laufenden Menschen (im Unterschenkel $\approx 270 \text{ m s}^{-2}$ und Oberschenkel $\approx 160 \text{ m s}^{-2}$). Die Phasenrelationen der Schwabbelmassen des Beins als Reaktion auf den Aufprall sind jedoch unterschiedlich. Beim Menschen treten die maximalen vertikalen Beschleu-

nigungen der segmentalen Muskelmasse ca. 5 ms (Unterschenkel) und 20 ms (Oberschenkel) nach maximaler Beinbeschleunigung auf. Beim Aufprall hat die schwingende Massendynamik bei größeren Tieren eine höhere funktionelle Relevanz, da es zu einer zunehmenden zeitlichen Trennung von Knochen- und Muskelbewegung kommt. Für einen vollständig aktivierten, frischen Muskel beträgt die Faserdehnung beim Ratten GAS mit 1 m s^{-1} (Studie 1) 0,2% als Reaktion auf einen Aufprall. Dementsprechend werden Querbrücken bis 11,8 N (40% der maximalen isometrischen Muskelkraft) gebunden. Dies ist praktisch derselbe Kraftgrenzwert $F = 12 \text{ N}$, der in der Steifigkeitsanalyse gefunden wurde. Dieser beschreibt, wo die Änderungen des Fasermaterials und die Steifigkeitseigenschaften des Muskel-Sehnen-Komplexes als Funktion der isometrischen Muskelkraft gesättigt sind. Konkret verringerten sich bei einer Kraftabnahme von der maximalen isometrischen Muskelkraft bis etwa 40% der maximalen isometrischen Muskelkraft, die gefundenen Fasermaterialsteifigkeiten von 9050 N m^{-1} auf 3700 N m^{-1} , und im Muskel-Sehnen-Komplex von 3450 N m^{-1} auf 2400 N m^{-1} .

Bei einer nahezu konstanten dynamischen Kraftänderung von 0,2 N über alle Versuche betrug die vom Muskel-Sehnen-Komplex dissipierte Energie bei maximaler isometrischer Muskelkraft $17 \mu\text{J}$, welche nach dem Aufprall im passiven Muskel-Sehnen-Komplex in einem Arbeitszyklus auf $50 \mu\text{J}$ anstieg. In allen Versuchen umfasst ein Arbeitszyklus eine Schwingungsperiode zwischen dem Aufprall (TD) und dem Moment des nächsten Nullpunkts, wenn die Massenschwerpunktbeschleunigung des GAS zum zweiten Mal auf Null zurückkehrt. Für das Fasermaterial änderte sich die dissipierte Energie von $3,5 \mu\text{J}$ im voll stimulierten Muskel, auf $23 \mu\text{J}$ im passiven Zustand. Daher dissipiert ein Halbsarkomer $10,4 \text{ zJ}$ im frischen, voll aktiven Muskel und bis zu 68 zJ im passiven Muskel. Bei maximaler Aktivität würde eine einzelne

Querbrücke somit 0,6% der pro ATP-Spaltung pro Aufprall verfügbaren mechanischen Arbeit abbauen, bei submaximaler Aktivität bis zu 16%.

Obwohl die isometrischen Kraftwerte in einem ganzen Muskel (23 N) skaliert auf das halbe Sarkomer (445 pN) perfekt mit ähnlichen Schätzungen in Einzelfaserexperimenten in der Literatur übereinstimmen, ist die Steifigkeit eines Halb-Sarkomers bei maximaler isometrischer Muskelkraft nur $2,2 \text{ pN nm}^{-1}$, die bei einem passiven Halb-Sarkomer auf $0,4 \text{ pN nm}^{-1}$ abnahm. Diese niedrigen Steifigkeitswerte stimmen nicht mit dem einfachen Halb-Sarkomer Modell überein, welches in Einzelfaserexperimenten verwendet wird. Die Diskrepanz zwischen $2,2 \text{ pN nm}^{-1}$ und Einzelfaserexperimenten ist höchstwahrscheinlich darauf zurückzuführen, dass die Einzelfaser-Experimente (induzierte 4000 Hz Schwingungen) nicht unbedingt die Arbeitsbedingungen eines *in-vivo* Halb-Sarkomers beim Aufprall erfüllen (überlagerte Schwingungen im Fasermaterial, liegen bei ca. 50 Hz). Die Anpassung der Daten an ein Coulomb-Kraftmodell (genannt *model2*) legt nahe, dass der Coulomb-Kraft getriebene Teil in der Querbrücke die Querbrückensteifigkeit dominiert. Der Unterschied in der Schwingungsfrequenz zwischen experimentellen und *in-vivo* Bedingungen wurde bereits in der Literatur angedeutet, wurde jedoch nie im Kontext der Cross-Bridge-Modellierung untersucht.

Um den Beitrag von Titin in passiven Fasermaterialien zu beurteilen, wurden zwei Modellannahmen verwendet: Erstens ist Titin allein verantwortlich für die passive Steifigkeit eines Halb-Sarkomers, dabei ist Titin entweder elastisch oder viskoelastisch. Wenn es elastisch ist, macht Titin 75% der Steifigkeit des Arbeitszyklusses aus. Im Falle der Viskoelastizität macht Titin 50% der dissipierten Energie in einem Halb-Sarkomer aus. Die zweite Modellannahme ist, dass Titin die Steifigkeit des Halb-Sarkomers teilweise in Verbindung mit Myosinfilamenten ausmacht. Für die zweite Modellannahme

ist die skalierte Titinsteifigkeit gleich der Dehnungssteigung im Arbeitszyklus. In einem passiven Halb-Sarkomer werden 100% Energie dissipiert, wenn Titin viskoelastisch ist.

Die Skalierung der Faserdehnungswerte vom Ratten GAS auf menschliche GAS legt nahe, dass die passiven Eigenschaften eine dominantere Rolle bei der Limitierung der Faserdehnung des menschlichen GAS beim Sprinten spielen. Die Faserdehnungen im menschlichem GAS Fasermaterial sind wahrscheinlich höher als in Ratten, da der Unterschied in der dynamischen Kraftänderung zwischen Menschen und Ratten viel größer ist, als der Unterschied in der anatomischen Querschnittsfläche zwischen den beiden Spezies.

Overview

Chapter 1

The 'General introduction' presents the background for creating this work, its necessity and the aims that must be achieved to reach the overall goal: a better understanding of skeletal muscle's wobbling response to impact in legged locomotion. To convey this work, the general introduction contains a short but detailed review of the relevant muscle physiology literature, including the structures and spacing on the microscopic level of the half-sarcomere. Subsequently, the chapter ends with a detailed description of the construction and functionality of the apparatus needed to study the muscle's wobbling mass in legged locomotion.

Chapter 2

The chapter that follows the 'general introduction' contains the methodological part of the work: how to conduct the experimental trials, the muscle preparation and the subsequent data processing.

Chapter 3 and Chapter 4

After Chapter 2, this work "splits" into two chapters, each designed to answer a specific aim presented in the introduction (Chapter 3: Study 1 and Chapter 4: Study 2)

Chapter 5

Discussion and comparison of results (Study 1 and Study 2) in order to compare muscle fibre responses to changes in impact amplitude (falling heights) and the stretch rate's influence on the critical fibre strain limit. This chapter also includes an estimation of the fibre strain in human GAS based on the

fibre strains determined in this work.

Chapter 6

Concludes Chapters 3-5 and delivers the prospects associated with this work.

The structure of this work, together with a general heading, is visualised in Fig. 1.

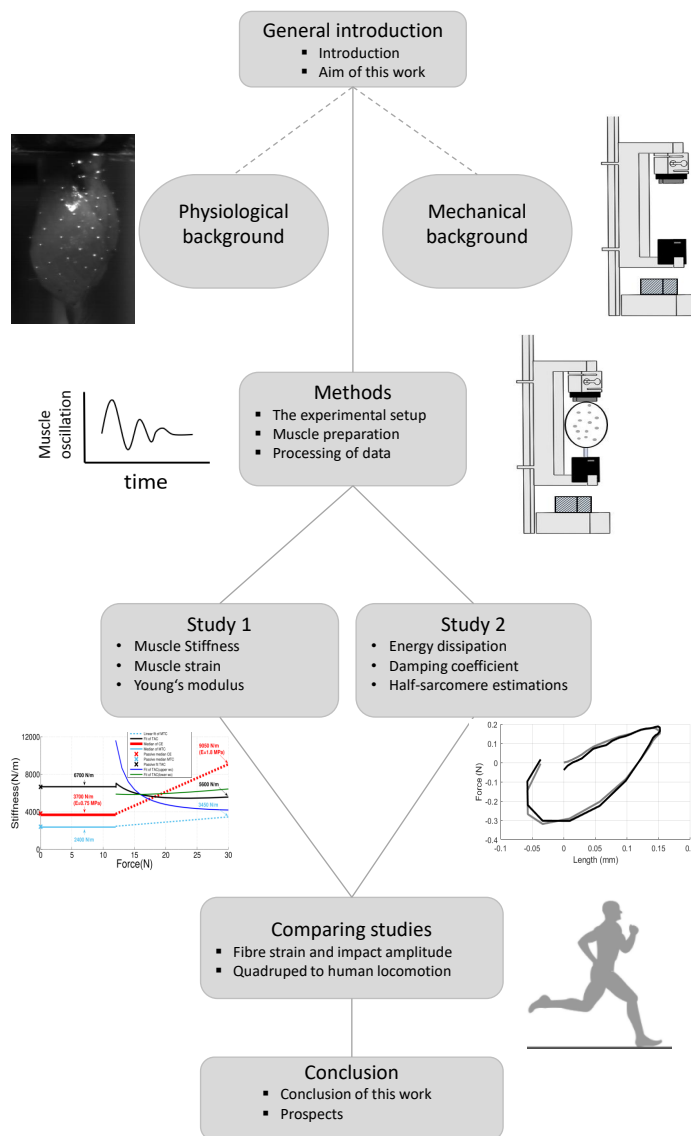


Figure 1 | Overview of all chapters. Each grey square, along with a small figure, illustrates a Chapter and a few keywords of what that Chapter includes. The grey, thin lines indicate the common thread throughout this work and which Chapters are directly related to the following Chapter. Both oval boxes, connected to the 'General introduction' via dashed lines, are subparts of the 'General introduction'.

Chapter 1

General introduction

1.1 Introduction

In more recent times, musculoskeletal models have become an increasingly vital tool to emulate limb movements to analyse movement efficiency [3], movement stability [4, 5] and movement performance [6]. Moreover, musculoskeletal models are also used for analysing limb movement under more specific circumstance such as injuries inflicted in car crash crashes [7] or the outcome of medical interventions [7]. Despite the benefits and advantages of musculoskeletal models, the output of a such a model is only as good as the rules and boundary conditions used to create it. For this reason, describing and understanding biological tissue relative to the environmental situation is of the utmost importance when trying to emulate musculoskeletal behaviour with computer modelling.

The two most popular approaches to understanding and emulating isolated muscle properties, ignoring the finite element approach, are the Hill-type and Huxley-type muscle models, named after Archibald Vivian Hill [8] and Andrew Fielding Huxley [9], respectively. A. V. Hill was the first to show

that the relationship between muscle force and velocity during concentric contractions has a hyperbolic shape, which he then described mathematically [10]. Later, A. F. Huxley presented the first comprehensive theoretical model [9] on muscle contraction, based on the *sliding filament theory* (see Sect. 1.2.1.2). In more recent times, there have been several successful attempts to combine or link Hill and Huxley muscle models with more micro-mechanical models of the muscle [11, 12]. These micro-mechanical models often contain *in-parallel* and *in-series* visco-elastic elements [13, 14]. More hybrid formulations combine the mechanical and thermodynamic properties [15]. While others exclusively derive the relation between force and velocity during contraction from assuming the muscle to fulfil thermodynamic equilibrium [16]. Yet, these mentioned muscle model combinations describe Hill- and Huxley-type muscle properties during contractions by first-order equations, thus, excluding muscle mass.

Probably the most common method to include mass properties in muscle modelling is visco-elastic coupling gross dynamics of accelerated soft tissue with skeletal structures represented by rigid bodies. This way of mass inclusion originated in 1985 [17, 18] when demonstrated that without an inclusion of visco-elastic coupling between a rigid and soft tissue segment (wobbling mass), estimated joint loads will be beyond tolerance during sports activities with high accelerations. Thus, such "wobbling" models are often used to examine legs impacting with the ground by either reproduction of direct measurement of soft-tissue vibrations [19, 20, 21, 22], reproducing ground reaction forces (GRF) in forward dynamics [23, 24, 25], or tissue vibration responses [26, 27]. The existence of soft tissue wobbling has also been measured experimentally [28, 19], and the idea of the muscle being a wobbling

mass was a keystone in conceiving the muscle tuning paradigm [29] (described in further detail later in the introduction). After establishing the introduction of the muscle as a wobbling mass in literature, it is generally accepted that when the leg makes contact with the solid surface (an impact), muscles absorb some of the shock-wave accelerations that propagate through the body. These shock-waves are transmitted to the limb muscle via their suspensions and contact areas to the bones and adjacent muscles, causing the soft-tissue masses of the body to undergo damped oscillations [30, 31, 32, 19].

However, the visco-elastic coupling between a rigid and soft segment does not explain how high-frequency shock-waves caused by an impact interfere with the contractile machinery within a muscle fibre that is the asynchronous work of many myosin heads building cross-bridges [9] between myosin and actin filaments within the sarcomeres. Until now, only a few studies have demonstrated the importance of the muscle's internal mass inertia influence on the contractile machinery. Günther *et al.* (2012) [33] used their second-order dynamic model to show that time-delays in force development were due to the muscle's internal mass inertia. They argued that direct measurement of maximum concentric contraction velocity is not possible in whole muscle preparations of large mammals without considering the muscle's internal mass inertia. Later, the model idea, introduced in Günther *et al.* (2012) [33], was expanded upon to demonstrate that the muscle's maximum shortening velocity is slower for lower activations and larger muscle sizes and larger sized muscles will have a higher inertial contraction cost.

Despite these recent findings, the interplay between muscle's internal mass and the contractile mechanism is still poorly understood. For example, in the contractile machinery, the net strain of all fibre-internal serial elasticities

in the actin and myosin filaments and the cross-bridges at maximum isometric force is approx. 0.4% [34, 1] in the non-fatigued case. Forces to disrupt one myosin head from actin have been measured to scatter around 9 pN [35], whereas estimations of the maximum isometric force of a cross-bridge is about 4-5 pN [36, 37, 38]. Additionally, force saturation in eccentric contractions, as another possible measure for a disruptive force limit of myosin heads indicating muscle 'giving', has been quantified to be 1.4-2.0 times the isometric force [39, 40, 41, 42]. It is unknown whether the contractile machinery will near the strain limit or even forcibly disrupt cross-bridges due to excessive fibre material strain caused by shock-waves during impacts in ordinary locomotion (see 'Aim of Study 1').

According to the muscle-tuning paradigm mentioned earlier, changes in muscle activity alter the mechanical properties of the muscle during the impact [24], therefore, affect both frequency and damping coefficient of its vibrations after TD [28]. Following the theory, the muscle can adjust the damping of its eigenfrequency vibrations after TD [29, 43]. Damping of oscillations superposed to muscle contraction results in a dissipation of mechanical energy. In whole muscles, Ettema *et al.* (1994) [44] calculated the energy dissipated in small-amplitude sinusoidal work-loops (ranging from 5-180 Hz) of rat gastrocnemius medialis. In the 5-180 Hz frequency range, the corresponding energy dissipated decreased from 55 μJ to 40 μJ in fully activated muscle [44]. However, using this experimental approach, oscillations are imposed on the distal tendon, which differs from *in-vivo* muscle wobbling responses induced by impacts. There seem to be no experimental data of directly measured damping strengths and energy dissipation associated with muscle wobbling in response to an impact. However, to explain microscopic sarcomere prop-

erties based on macroscopic wobbling measurements during impact requires the application of muscle models.

Based on muscle fibre experiments, Fusi *et al.* (2014) [1] determined cross-bridge stiffnesses and strains using a muscle model consisting of myofilament stiffness *in-series* with the stiffness of the cross-bridge ensemble. In their model, the force generated by a single cross-bridge is assumed a constant, with an attributed constant deflection. Thus, the overall cross-bridge stiffness scales linearly with the number of attached myosin heads. An alternative for determining cross-bridge stiffnesses is the model from Günther *et al.* (2018) [2]. This model can reproduce the early half-sarcomere force recovery phase (also known as the T2 curve [45, 46]) following rapid step-in-length experiments. According to their model, the ensemble of cross-bridges is *in-series* with a collective of passive stiffnesses, denoted there as a combined myosin head and myofilament stiffness. The cross-bridge itself is divided into a catalytic domain and a light chain domain that can rotate, actuated by a Coulomb force drive, with respect to the catalytic domain. In contrast to Fusi *et al.* (2014) [1], the force-length relation of this cross-bridge drive is non-linear as it depends on the properties of the repulsing Coulomb force generated within the catalytic domain. Thus, the second part of this work will focus on explaining microscopic sarcomere properties by probing the two mentioned muscle models with the experimental wobbling mass data (see 'Aim of Study 2').

1.1.1 Aim of Study 1

The first aim of this work (Study 1) will be to examine whether cross-bridges in active skeletal muscle are disrupted when strained by shock-waves in the physiological range in legged locomotion. To that end, Study 1 focuses on

mechanical properties that are strain and stiffnesses in the fibre material, the tendons and aponeurosis, and the whole muscle in response to an impact. The key research questions that need answering are:

- *What are the strain amplitudes in the fibre material in response to an impact during ordinary locomotion?*
- *What are the muscle's eigenfrequencies for responses to impacts, and how is the size-dependency of this time scale of muscular wobbling mass dynamics?*

1.1.2 Aim of Study 2

The second part of this work (Study 2) is to better understand the damping and energy dissipation of the whole muscle and the fibre material during wobbling by calculating stiffnesses, damping coefficients, and the energy dissipated during work-loops in the range from passive to fully activated muscle tissue and then scaled these parameters to the half-sarcomere level. The aim is to probe the predictions of cross-bridge stiffness values by half-sarcomere models: the first by Fusi *et al.* (2014) [1] and the second by Günther *et al.* (2018) [2]. These two models' potentials are probed to explain, by essential cross-bridge parameters, a muscle's overall response to an impact. To this end, the key research questions that need answering are:

- *How much energy is dissipated in a half sarcomere during muscle wobbling from passive to active muscle?*
- *Which parameters are essential to model experimental cross-bridge stiffness with a half-sarcomere model during an impact situation?*

1.2 Physiological background

1.2.1 Skeletal muscle

There are three types of muscle tissue in the body: cardiac muscle tissue, smooth muscle tissue and skeletal muscle tissue. Of these three types, skeletal muscle tissue is responsible for the movement of the body. Also, skeletal muscles have many subtle and secondary functions in the body. Including maintaining body temperature, protect other soft tissues, and store nutrition reserves. This chapter will focus solely on the skeletal muscle because it is the only type of muscle tissue used in this work.

In a skeletal muscle, the muscle tissue makes up approximately 80% of the muscles physiological cross-sectional area (PCSA) that is the cross-section of the muscle tissue determined perpendicular to the fibre direction. Accordingly, around 20% of the PCSA is composed of nerves, blood vessels and connective tissue. Of the latter, the connective tissue primarily exists in one of three layers: epimysium, a perimysium, and an endomysium layer, which either surrounds the muscle itself (epimysium), the fibre bundles (perimysium), the single fibres (endomysium), respectively (Fig. 1.1). All three layers are composed of collagen fibres [47] that have high Young's modulus values of 5-11.5 GPa [48] to support, protect, and structure skeletal muscle [47]. As such, they span the entire muscle length to form either a bundle known as *tendon* or a broadsheet called *aponeurosis* in the other end. In most cases, tendons or aponeurosis usually attach to bones, and as the muscle contract, it exerts a pull to the attached bone, which then initiates skeletal movement.

1.2.1.1 The half-sarcomere

On a microscopic level, the functional unit within a muscle fibre responsible for contraction is named *sarcomere*, and a series of sarcomeres span the entire length of the muscle fibre (Fig. 1.1). Sarcomeres usually have an optimal length (L_0) of about $2.3\ \mu\text{m}$ for generating maximum isometric force, which depends slightly on myofilament lengths and species (mean L_0 values are from [Table 1] [49]). Each sarcomere contains a thick filament called myosin and thin filaments called actin that appears lighter in colour than myosins when seen by electron microscopy (Fig. 1.2e). The sarcomere is a very complex structure, where each region has its properties. Thus the sarcomere can grossly be separated into either the actin region (I-band) or the region that contains both actin and myosin (A-band). Because the A-band contains both actin and myosin, this band can further be subdivided into the H-zone, which includes only myosin (Fig. 1.2a) and the overlapping zone that has both actin and myosin. Myosin filament arrangement is so that they, together with five adjacent myosins, form a hexagonal lattice (Fig. 1.2d). A single myosin contains 300 heads placed together in crowns of three pairs, spaced periodically with $14.5\ \text{nm}$ [50] (Fig. 1.3b). At each location, the three crowns are separated azimuthally by 120° and adjacent crowns are rotated by 40° . Thus, at each $42.9\ \text{nm}$, crowns are aligned. The heads that project from each myosin can bind to one of six surrounding actins (Fig. 1.2c), which do so in a stochastic manner. Because of the before-mentioned hexagonal lattice, one myosin filament can interact with six actin filaments. Thus, each elementary cell of a sarcomere contains one myosin filament and two actin filaments [50] (Fig. 1.2c).

1.2.1.2 Sliding-filament theory

The most common and accepted theory for muscle contraction is the sliding filament theory introduced in 1954 [51, 9, 52]. In brief, the sliding filament theory states that muscle contraction itself happens because of the relative sliding between the thick and thin filaments. The sliding occurs as actin filaments move past myosin filaments while actively interacting with them through the myosin cross-bridges. It is, in general, believed that approximately 90 of the possible 300 myosin heads are stochastically bound at all time while the muscle in physiologic tetanus (tetanic contraction) [53].

1.2.1.3 Titin arrangement's within the sarcomere

Until now, the structural description of the sarcomere mostly include actin and myosin. Leaving out the protein titin: a $1\ \mu\text{m}$ long filament [54, 55], which connects the Z-line and the M-line through a myosin filament [55]. The titin filament has since discovered in 1977 [56] risen to prominence. Today titin is believed to be responsible for force-enhancement [57, 58, 59], as well as passive force contribution, mechano-sensing, and help maintain the structural organisation within the sarcomere [59]. The number of titin filaments that connects to one myosin filament is still debatable, and although the most popular estimation is six titin's per elementary cell [60, 55, 61] supported by mass measurements [60]. However, there are also suggestions that only four titin filaments connect to each myosin [62, 63]. The dispute between which number is correct probably originates from the symmetry difference between the arrangement of myosin found in the A-band [64] and actins in the Z-line [65]. The thick and thin filaments in the A-band cross-section have both hexagonal lattices shapes (Fig. 1.3c), which suggests that titin filaments are highly likely to have a 3-fold symmetry to match that hexagonal

symmetry. For a 3-fold symmetry, the mass per unit length of the end-filament (17.1 kDa nm^{-1}) is also consistent with six titin molecules [60]. In contrast, the cross-section arrangement of the actin filaments in the Z-line has more the shape of a parallelogram than a hexagon (Fig. 1.3b). This makes the likelihood of a 2-fold symmetry more reasonable. One of the most popular explanation for this 2-fold/3-fold mismatch is, that the actin filaments in the A-band are systematically displaced from the Z-line positions [66, 67, 65]. Regarding the number of titin filaments per actin, one possible theory that comply with the 2-fold/3-fold transformation [67], is that that each actin filament is associated with two titin filaments in one sarcomere and a single titin filament in the next sarcomere [66, 60]

1.2.1.4 Force generation in a half-sarcomere

The amount of force generated within a sarcomere depends on the number of formed cross-bridges, which, in turn, depends on the thick and thin filaments overlap withing these sarcomeres. A sarcomere generates the most force when the filaments are within a small optimal range that depends slightly on the animal size [49]. As an example, the muscle force relative to sarcomere length is shown in Fig. 1.4, where the sarcomere within an optimal range ($\approx 95\text{-}105\%$ of L_0), the muscle can generate its maximum force. If the sarcomere is lengthened or shortened to values outside the optimal range, then the sarcomere can not generate the same muscle force. The drop in muscle force is mainly because the amount of generated muscle force depends on the number of cross-bridges that form (see Sect. 1.2.1.2). For the sarcomere to generate muscle force, it must receive an action potential stimulus: a single action potential stimulus produces a single contraction (a twitch) [50]. The single twitch grossly consists of 3 phases: the latent phase, the contraction

phase, and the relaxation phase. During the latent phase, the muscle fibre produces no force, as there exists a time delay between the stimulus and the various processes in the muscle needed to execute a contraction. In the contraction phase, force rise is due to myosin heads binding to troponin active sites on actin filaments. These attachment sites become visible as the tropomyosin that covers them moves away as calcium is released. In the last phase, the relaxation phase, calcium levels fall, which causes tropomyosin to cover the actin attachment sites. The latter leaves the number of formed cross-bridges to decline as they detach. The addition of one stimulus twitch to another before the relaxation phase begins will eventually lead to a saturated force level whereby achieving a tetanic contraction. In this state, each half-sarcomere generates approximately 480 pN. A value inferred from step-in-length [68] or step-in-force [53] fibre experiments. If each sarcomere contains 300 myosin heads of which 90 stays bound at all time at maximum isometric force (F_{max}) [53], then the force per attached head is ≈ 5 pN ($480 \text{ pN} \div 90$).

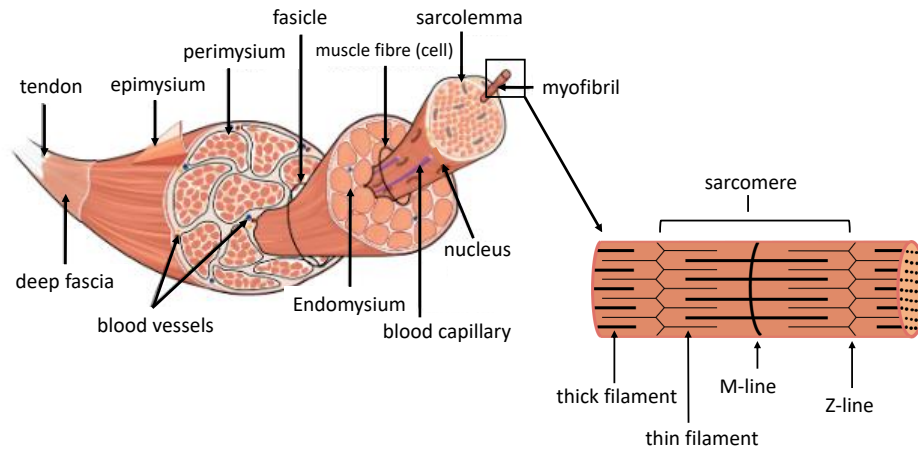


Figure 1.1 |Structural hierarchy of skeletal muscle. The three layers of connective tissue: epimysium, perimysium, and endomysium, enclose the various structures within skeletal muscle and allow for blood vessels, capillaries and nerves to interweave deep into these compartments. Epimysium surrounds the entire skeletal muscle, and perimysium surrounds bundles of muscle fibres. Lastly, endomysium encloses single muscle fibres. Within a single muscle fibre, the small myofibril contains sarcomeres *in-series*. Each sarcomere reaches from Z-line to an adjacent Z-line. The sarcomere is most commonly known for its contractile properties involving thin and thick filament interaction. The muscle in Figure 1.1, excluding the highlighted sarcomere, is from Tsang *et al.* (2019) [69], reproduced with permission from Elsevier.

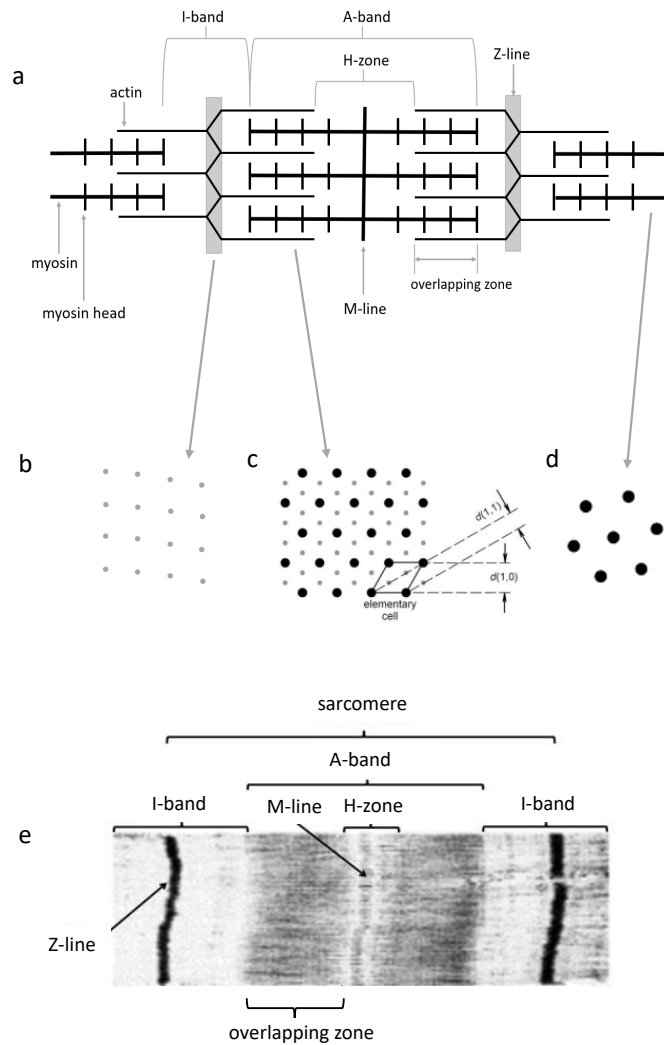


Figure 1.2 | Spacing and dimensions in a sarcomere **a**, a single sarcomere reaches from one Z-line to its adjacent Z-line. Within the sarcomere is a part that contains no myosin, which is called the I-band. Next to this I-band follows the A-band, which includes both myosin and actin filaments. The A-band also have two subdivisions named the overlapping zone and the H-zone. The overlapping zone contains both actin and myosin hence the overlap, and the H-zone contains only myosin filament. **b**, the cross-section of the actin arrangement in the Z-line. **c**, the cross-section of actin and myosin in the overlapping zone (actin: small dots, myosin: big dots). **c** also includes the crystallographic planes (1,0) and (1,1) used to define an elementary cell, i.e. one myosin and two actin [50]. **d**, the cross-section of the myosin arrangement in the A-band near the Z-disk, **e** is the electron micrograph of the sarcomere from Wallig *et al.* (2017) [47] reproduced with permission from Elsevier, and **c** is from Reconditti (2006) [50], reproduced with permission from IOP Publishing.

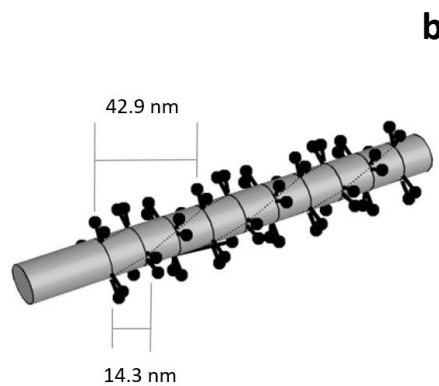
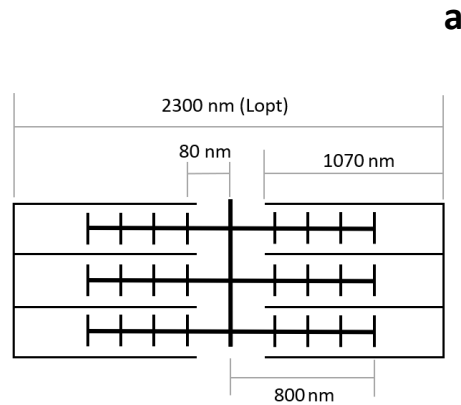


Figure 1.3 |Schematic drawing of a sarcomere. **a** depicts a sarcomere at optimal length (L_{opt}) of 2300 nm, where it is able to generate the most force (see also Fig. 1.4). For a half-sarcomere, the actin filament is ≈ 1000 nm depending on size and species [70, 71] and the myosin filament 800 nm [70, 72] with an 85 nm bare-zone [73]. **b** depicts a half-sarcomere myosin and its 300 heads. In each crown, each pair of heads are separated azimuthally by 120° and the adjacent crowns are rotated by 40° . Therefore, at each 42.9 nm, crowns are aligned [50]. **b** is from Reconditti (2006) [50], reproduced with permission from IOP Publishing.

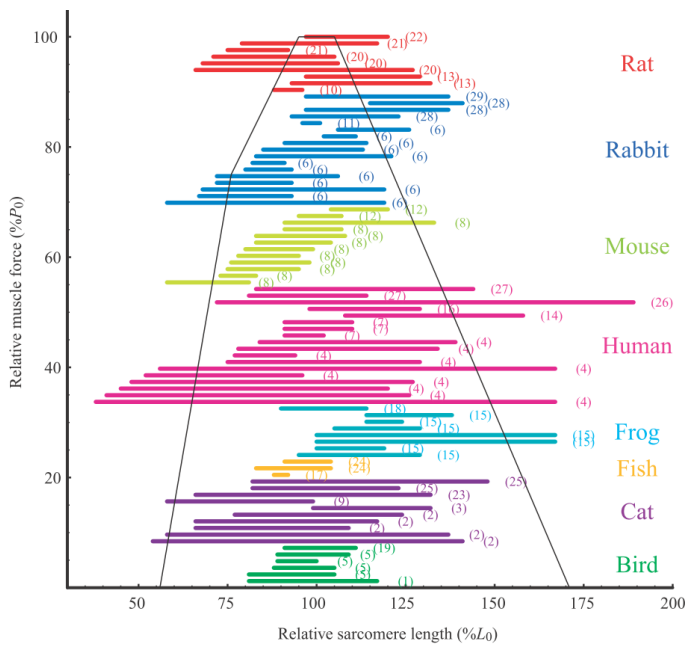


Figure 1.4 |Muscle tension relative to sarcomere length. Sarcomere operating ranges for various species, superimposed upon a normalized sarcomere force/length curve (thin, black line). When the sarcomere is within the optimal range (force plateau), the sarcomere can generate the most force. If the sarcomere length falls outside this region, the sarcomere can no longer generate the same force. The mean optimal sarcomere length $L_0 = 2.3 \mu\text{m}$. This figure is from Burkholder & Lieber (2001) [49], reproduced with permission from Journal of Experimental Biology.

1.2.2 Ischaemia and fatigue

By dissecting a skeletal muscle, regardless of which, removes the muscles blood supply (also called ischaemia). Exposing the muscle tissue to severe and prolonged ischaemia will inevitably lead to necrosis and permanently damage the muscle tissue.

During ischaemia, studies have shown that the muscle force decline ranges from 95% of the isometric force in cat *m. soleus* and 90% in *m. gastrocnemius medialis and lateralis* both after ca. 23 minutes of ischaemia [74] to 58% isometric force decline after 1 hour in rabbit *m. anterior tibialis* [75]. Despite

these declines, reperfusion restored 100 % of isometric force in cat *m. soleus* and *m. gastrocnemius* [74] (‘... the soleus fully recovers in about 5 min while the recovery of the gastrocnemius takes 10-15 times longer.’), and 87 % in rabbit *m. tibialis anterior* [75]. Further studies stated full recovery (> 90%) after 1 hour of ischaemia, proving that rapid fatigue within 1 hour is a metabolic adaptation to limited oxygen, nutrient, ion, and hormone availability, and also impeded waste removal, rather than any cellular process permanently being disabled by necrosis [76, 77] (see also Fig. 4.1). In a single case, the *m. gastrocnemius* in Wistar rat was recovered 75% after 2 hours of ischaemia [78].

In general, the term muscle (or physical) fatigue is used to indicate a transient decrease in the capacity to sustain physical actions. As such, the term is broad and includes, among others, the following definitions:

- ”Performing a motor task for long periods of time induces motor fatigue, which is generally defined as a decline in a person’s ability to exert force.” [79]
- ”... a fatiguing task was performed with the muscles of the left hand until the muscles were exhausted.” [80]
- ”Fatigue is known to be reflected in the EMG signal as an increase of its amplitude and a decrease of its characteristic spectral frequencies.” [81]
- ”Intensive activity of muscles causes a decline in performance, known as fatigue...” [82]

Because it is ambiguous as to where and what the origin of muscle fatigue is, and ischaemia studies indicate that reperfusion can restore muscles to their *in-vivo* states before ischaemia, any decline in upholding the maximum isometric muscle force is from this point onwards considered fatigue.

1.2.3 Animals used

This work used the *m. gastrocnemius medialis and lateralis* from the male *Rattus norvegicus*, Wistar in all experiments. The main reasoning behind this choice was that the Wistar rats were compatible with the facilities and equipment available for the experiments. Also beneficial of this choice was that the literature is rich on data regarding physiological measurements and mechanical properties on the isolated GAS muscle of the specimen Wistar to better support and discuss some of the choices made and results throughout this work. Compared to mouse, another widely used rodent used for experimental animal designs, the mass of the rat GAS should, in theory, allow for higher amplitudes of the vibrations due to the greater muscle mass (Eq. 1.42).

The GAS itself is one of the more accessible muscles to dissect in the rat, and the muscle's origin and insertion make it possible to cut off the bony pieces of the femur and calcaneus still attached to the tendon. A dissected muscle with the bone tissue pieces of the femur and calcaneus will allow for a complete muscle-tendon-complex (MTC) without changing the properties of both tendons or the muscle itself. The rat GAS is also very suitable for these *ex-vivo* types of experiments done because the muscle can still produce a stable isometric force after 400 ms [83]. When fully stimulated for 50-300 ms every 1-2 second, the GAS muscle can still provide about 80% of its maximum force [84, 85]. Further, the *m. gastrocnemius* has been examined with regards to ischaemia in various small rodents and mammals (Sect. 1.2.2).

1.3 Mechanical background

1.3.1 Criteria for the construction of the frame

An experimental frame had to be designed that could fixate the isolated muscle tissue, to observe the wobbling behaviour of an isolated muscle during impact scenarios. The basic idea was to fix the isolated muscle in a C-shaped frame that could measure muscle force and drop this frame on the ground from a certain height to simulate the impact.

In the initial thought-process of designing the C-shaped frame, it became clear that the frame itself needed to meet a few guideline criteria (listed as bullets below) because of the novelty of the experiments. For this reason, the frame was built from available construction-store materials and not after what is possible to manufacture externally. The overall idea was that if anything were to break or need optimisation under the experiments, then the parts in question should be easily replaceable. To further facilitate this easy-to-replace idea, the frame consists of squares or rectangular parts as squares or rectangular profiles are more convenient to remove and replace than, for example, an ellipse profile. Being able to rebuild the frame was especially important since all the experiments were at an external location, with only a limited time was available for each set of experiments. Choosing store materials and square profiles also enhanced the frame customizability and costs in the early stages of a never-before tested experimental setup.

Besides the materials and shapes to build the frame, i.e. not including material properties, an equally important consideration is the overall size and functionality. The C-shaped frame should ideally perform various experimental trials with more than one muscle length. As such, the frame backbone needs to be longer than actually necessary for the GAS muscle

to be mounted. Thus, the possibility to change the length between both clamps (needed for muscle fixation) via a build-in slider mechanism is vital. A build-in slider facilitates both changes in muscle sized and variations in GAS length.

The last considerations (in mentioned order) are frame deflection and frame mass. The maximum deflection (compression) of the frame including the force transducer, clamps and insulators (See Fig.2.3) should be lower than $5 \cdot 10^{-4} m$, because a frame length change of 0.5 mm to a GAS of ≈ 45 mm, leads to an internal fibre strain of $0.01 \approx \frac{0.5 \text{ mm}}{45 \text{ mm}}$. Therefore, assuming that all deformation goes into the fibre material of the muscle, an internal fibre material strain of 0.01 is low enough so that any length changes caused by the frame have no influence on the maximum generated cross-bridge force (Fig. 1.4), because the length at which the cross-bridge can generate its most force is considered more of a plateau than a specific sarcomere length (Sect. 1.2.1).

Although a frame with a low mass conflicts with the deflection criterion, a lighter frame will extend the falling time of the frame to meet a targeted impact. The reason for building a lightweight frame is that any potential perturbations caused by the release-mechanism (electromagnets) on the frame will attenuate over time. Hence, extending the falling height attenuates any release mechanism perturbations. Thus, overall the construction of the frame has to fulfil the following criteria:

- Parts used to build the frame should be available in a general store.
- Individual frame parts should be square or rectangular profiles.

- The frame should have a built-in slider to accommodate changes in muscle size.
- Hook and clamps: the muscle must be easy to fixate (ischaemia) and easily replaceable.
- The overall frame deflection must be under 0.5 mm.
- The frame must have a low frame mass to allow for a longer fall time.

1.3.2 Theory behind frame

In accordance with Hooks' law:

$$\sigma = E \cdot \epsilon \quad , \quad (1.1)$$

stress (σ) is equal to strain (ϵ) multiplied with a material constant E being Young's modulus. Stress can then either be compressive or tensile, respectively, depending on either a positive or negative strain prefix in Eq. 1.1. If a force (F) is applied to a fixed cantilever beam, as shown in a simple case in Fig. 1.5a, then compression ($-\sigma$) and tension ($+\sigma$) rises with the distance from the structure's centerline (y).

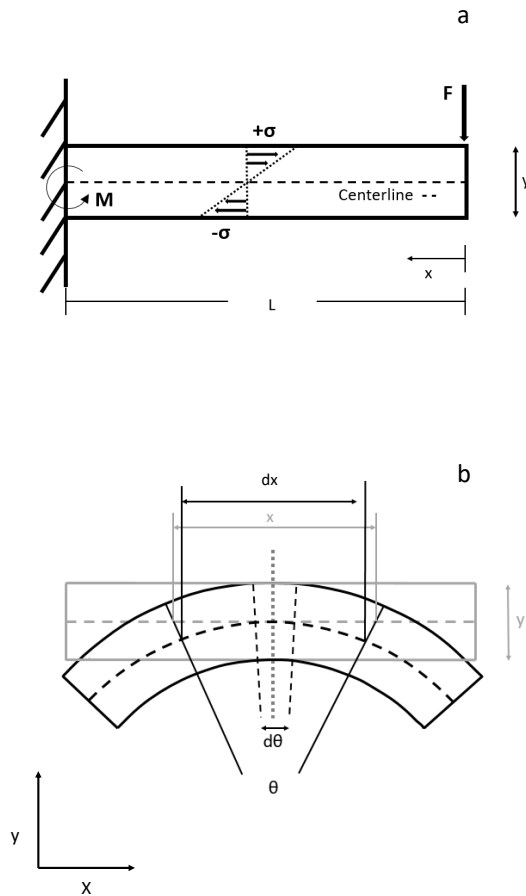


Figure 1.5 | A cantilever beam. **a** shows a force F applied to the tip of a fixated beam. The thick, horizontal arrows inside the beam either illustrates increased compression or tension from the centerline (dashed line) due to the applied force. The centerline is neither in compression or tension, i.e. the centerline is a neutral axis in the construction. L is the beam length, and x is the length from the end of the beam $x = 0$ towards the fixation $L = x_{max}$. y is the length from the beam centerline in either direction, and M is the bending moment. **b**: The solid grey rectangle is a drawing of a free-floating beam with no force applied, whereas the black, solid rectangle in **b** is a free-floating beam with identical bending moments in both ends. The dotted, grey, vertical line in the middle of both rectangles is where both centerlines (grey and black dashed lines, respectively) have no vertical deflection ($\delta=0$). The point, $\delta=0$, could also illustrate the centerline at x_{max} in **a** (i.e. at the fixation point). As the angle θ becomes smaller $d\theta$, the centerline length of the grey rectangle x approximates the centerline length of the black rectangle dx .

Regardless of the bending, the centerline of a bend structure can be ap-

proximated to follow the course of the unbent centerline. The latter is shown in Fig. 1.5 b, where the black rectangle illustrates a beam with identical bending moments in both ends. At $d\theta$, $dx \approx x$ of an unbent beam (grey rectangle). Thus, the longitudinal strain (ϵ_x) is

$$\epsilon_x = y \kappa \quad (1.2)$$

because compression and tension rises with the increased distance from the centerline (Fig. 1.5a). The latter equation is called the *strain-curvature*. By substituting ϵ_x in Eq. 1.1 with Eq. 1.2, the curvature (κ) can be expressed as

$$\kappa = \frac{\sigma_x}{E y} \quad (1.3)$$

Although Eq. 1.3 technically allows one to determine the stress, as either tension or compression, at any given point in Fig. 1.5a, the curvature is often an unknown quantity. Multiplying Eq. 1.3 with an additional y in the nominator and denominator is equal to

$$\kappa = \frac{\sigma_x y}{E y^2} \quad (1.4)$$

$$= \frac{F y}{E A y^2} \quad (1.5)$$

$$= \frac{M_z}{E I_z} \quad (1.6)$$

because the inertia (I) is $\int dA \cdot L^2$ (see Eq. 1.26). Both M and I is with respect to the z -axis. In a general term, it is possible to calculate the stress without the curvature by rearranging Eq. 1.3, and substituting κ with Eq. 1.6:

$$\frac{\sigma}{E y} = \frac{M}{E I} \quad (1.7)$$

$$\sigma = \frac{M y}{I} \quad . \quad (1.8)$$

Looking at Eq. 1.4 and Eq. 1.8, the maximum compression or tensile stress is found at $x = x_{max}$, and $y = y_{max}$ in Fig. 1.5a. For the frame construction itself, however, the stress is not considered an optimisation criterion, because the forces that act in the frame will be so low, that potential plasticity plays no role. It makes more sense to construct the frame optimised after a deflection criterion, for which Eq. 1.6 is more useful.

Unfortunately, the curvature is, in most cases, an unknown parameter. However, if the curvature (dashed centerline) in the Fig. 1.5b black beam were to continue uninterrupted, it would eventually form a complete circle with a radius (as indicated in Fig. 1.6):

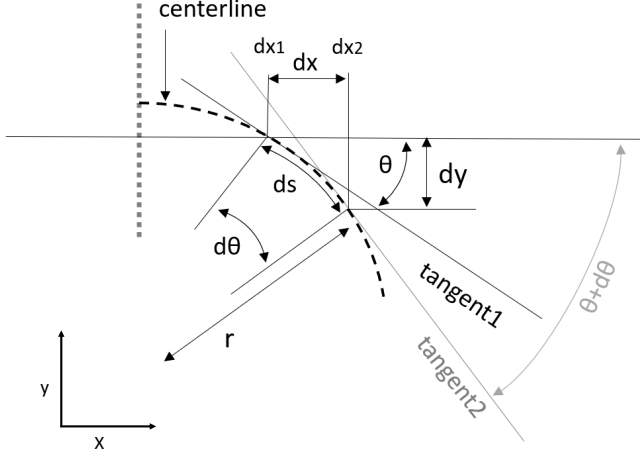


Figure 1.6 | A deflected centerline in a beam. In the figure, there is no deflection ($\delta = 0$) where the vertical, grey dotted line intersects the centerline (black, dashed line). This point on the centerline could, for example, be at the fixation in Fig. 1.5a or the grey, vertical, dotted line in Fig. 1.5b. At $\delta = 0$, the centerline also has no angle, so also $\theta = 0$. ds is the centerline length (arc length) to a central angle $d\theta$ between dx_1 and dx_2 . dx and dy are the horizontal and vertical length parts of ds , respectively. θ , is the rotational angle at tangent1, and tangent2 at dx_2 marks the beginning of an adjacent part of the arc. r is the length from the centerline to the centre of the arc.

As such, the curvature of a circle is the reciprocal of the *radius of curvature* ($\kappa = \frac{1}{r}$) with r being the radius, is equal to the arc length divided by the tangential angle ($\frac{d\theta}{ds}$). Therefore, the curvature in Fig. 1.6 is

$$\kappa = \frac{1}{r} = \frac{d\theta}{ds} \quad . \quad (1.9)$$

As $ds \approx dx$ as $\lim_{\theta \rightarrow 0}$, the angle θ in Fig. 1.6 can be estimated as

$$\theta \approx \tan(\theta) = \frac{dy}{dx} \quad . \quad (1.10)$$

Therefore, integrating Eq. 1.6 and Eq. 1.10 in Eq. 1.9, the curvature is

$$\frac{d^2y}{dx^2} = \frac{M}{EI} \quad , \quad (1.11)$$

which is also called the *moment-curvature relationship*. As $\int \frac{d^2y}{dx^2} dx = f''(x) dx$ (Leibniz's notation) and $\int x^n dx = \frac{x^{n+1}}{n+1}$ (power-rule), the anti-derivative of Eq. 1.11 with respect to x is

$$EI \int \frac{d^2y}{dx^2} = -F \cdot \int x \quad (1.12)$$

$$EI \frac{dy}{dx} = \frac{-F x^2}{2} + C_1 \quad (1.13)$$

with C_1 being an added integral constant, and the force F being negative because the bending moment ($M = -F \cdot x$) is in the opposite direction of the applied force. To solve C_1 , the boundaries $y=0$ and $\theta=0$ is assumed, which, for example, would be good approximations at $x=L$ in Fig. 1.5a or at $x=\frac{L}{2}$ in Fig. 1.5b. Because both beam examples fulfil both boundary conditions, it is convenient to continue with $x=L$ and $\theta = \frac{dy}{dx} = 0$ (Eq. 1.10). Therefore,

$$C_1 = EI \cdot 0 - \frac{-F x^2}{2} \quad (1.14)$$

$$= \frac{FL^2}{2} \quad . \quad (1.15)$$

By substituting Eq. 1.15 with C_1 in Eq. 1.13, θ (note Eq. 1.10) can be found at any given point with

$$\theta = \frac{1}{EI} \left(\frac{-F x^2}{2} + \frac{FL^2}{2} \right) \quad , \quad (1.16)$$

and at $x=0$, Eq. 1.16 can be simplified to

$$\theta = \frac{F L^2}{2 E I} . \quad (1.17)$$

With a known value for C_1 in Eq. 1.15, the derivative of Eq. 1.13 is

$$EI \int \frac{dy}{dx} dx = \frac{-F f(x)^2}{2} + \frac{FL^2}{2} dx , \quad (1.18)$$

$$EI \int \frac{dy}{dx} dx = \frac{-F (\frac{x^3}{3})}{2} + \frac{FL^2}{2} dx , \quad (1.19)$$

$$EI \frac{y}{x} = \frac{-F x^3}{6} + \frac{FL^2}{2} + C_2 , \quad (1.20)$$

and

$$EI y = \frac{-F x^3}{6} + \frac{F L^2}{2} + C_2 \cdot x . \quad (1.21)$$

At $y = 0$ and $x = L$, C_2 is

$$C_2 = -\frac{-F L^3}{6} + \frac{F L^2 x}{2} \quad (1.22)$$

$$= -\frac{F L^3}{3} . \quad (1.23)$$

From this, the deflection at any given point in Fig 1.5a can be determined with

$$y = \frac{1}{EI} \left(\frac{-F x^3}{6} + \frac{F L^2 x}{2} - \frac{F L^3}{3} \right), \quad (1.24)$$

which can be shortened to

$$\delta = y_{max} = \frac{-F L^3}{3 E I} \quad (1.25)$$

for determining the maximum deflection at $x=0$ in Fig 1.5a.

For numerical calculations, both Eq. 1.17 and Eq. 1.25 have three parameters that are relatively easy to determine: force F , Young's modulus E and length L . However, inertia I is material and profile dependent, thus, to apply Eq. 1.17 and Eq. 1.25 to conceptualise a suitable frame for all experiments, an understanding of inertia in rectangular profiles is needed (For details regarding design considerations, see Sect. 1.3.1). The *parallel axis theorem* applied to the second moment of area for a plane with respect to a reference x-axis *not* being the centroidal x-axis is

$$I_{z'} = I_z + A \cdot d^2 \quad (1.26)$$

with $I_{z'}$ being the objects inertia around a reference axis that is *not* the objects centroidal axis. A is the area of the plane region, and d is the perpendicular distance between a reference axis and the centroidal axis. I_z is the second moment of area relative to the shapes centroidal axis, which is the integral of the shape height (h) and the elemental area (dA) were

$$I_z = \iint h^2 dA \quad . \quad (1.27)$$

Therefore, if the reference axis is the centroidal axis as in Fig. 1.7,

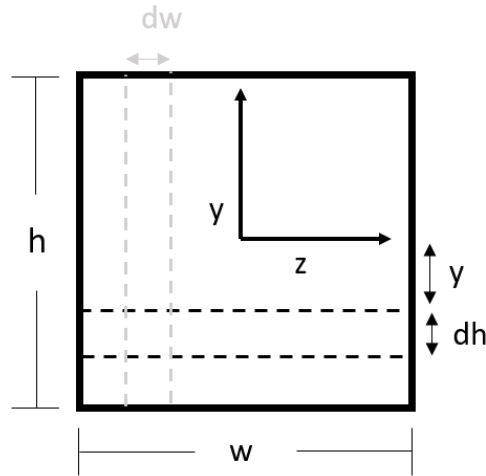


Figure 1.7 | An example of calculating inertia in a square. The square has the height h and the width w . The elemental area, in this example, has the elemental height dh and the elemental width dw . The coordinate system, about where the rotation takes place, is in the centroid of the square. y is the vertical length between the x-axis (axis-of-rotation) and the nearest limit of dh in either direction.

then the second term of Eq. 1.26 can be removed, and with $I'_z = I_z$ the inertia about the objects centroidal x-axis in Fig. 1.7 becomes

$$I_z = \int y^2 w dh \quad (1.28)$$

with $dA = w \cdot dh$, when removing one integration. In Eq. 1.28, w is the width of the square and y being the length from the centroidal axis to the limits of the square. Because the integral limits of y , in this case, is $+h/2$ to

$-h/2$, since h is the height of the square, Eq. 1.28 can be written as

$$I_z = w \int_{-h/2}^{+h/2} y^2 dh \quad (1.29)$$

$$= w \left[\frac{h^3}{3} \right]_{-h/2}^{+h/2} \quad (1.30)$$

$$= w \left[\frac{(h \div 2)^3}{3} - \frac{(h \div 2)^3}{3} \right] \quad (1.31)$$

$$= \frac{wh^3}{12} \quad (1.32)$$

For all structures in Fig. 2.3, with the exception of the force transducer and upper clamp, the inertia can be found with either Eq. 1.32 or

$$I_z = \frac{w^3 h}{12} \quad (1.33)$$

For solid rectangular shapes. If a profile has a hollow centre, then

$$I_z = \frac{w h^3}{12} - \frac{w_{in} h_{in}^3}{12} \quad (1.34)$$

$$I_z = \frac{w^3 h}{12} - \frac{w_{in}^3 h_{in}}{12} \quad (1.35)$$

The equations Eq. 1.32, 1.33, 1.34 and 1.35, shows that the lengths in the direction of applied force are a factor of 3 compared to material lengths perpendicular to an applied force. The last four equations also indicate that an, e.g. elliptic frame profile or Taperwall, would sustain stiffness and reduce weight compared to square a profile. For clarification, Taperwall means exposing the frame to the same amount of stress in any arbitrary point on the frame. Thus, in the cantilever beam example (Fig. 1.5a.), the thickness (t) in the construction should decrease from the fixation towards

the applied force. From Eq. 1.8 and Eq. 1.34 an optimization of the thickness (Taperwall) in a rectangular structure is

$$I = \frac{M y}{\sigma} \quad (1.36)$$

$$\frac{w_{in} h_{in}^3}{12} = \frac{w h^3}{12} - \frac{M y}{\sigma} \quad (1.37)$$

$$w_{in} h_{in}^3 = w h^3 - \frac{12 M y}{\sigma} \quad (1.38)$$

$$(w - 2t)(h - 2t)^3 = w h^3 - \frac{12 F y}{\sigma x} \quad , \quad (1.39)$$

if the outer cross-section dimensions w and h and stress σ are known predetermined values. Because Eq 1.36-1.39 are only for showing the idea behind Taperwall, and because the frame itself does not use Taperwall, the thickness in Eq. 1.39 is not inferred any further.

The equations Eq. 1.9,1.17, 1.25, and 1.32-1.35 are fairly straightforward to implement, especially given some of the boundary criteria in Sect. 1.3.1. Thus, these equations were used to calculate the deflection for any theorised frame to apply with the strain limit criterion of $5 \cdot 10^{-4}$ m (see Sect. 1.3.1). It should be noted, that the profiles and properties of the mounted force transducer, clamps and isolation parts to some degree are predetermined and not possible to customise, therefore, they were excluded from the frame deflection calculations (for the complete experimental setup, see Sect. 2.1.2). As examples of the latter predeterminations, the force transducer is pre-made, the clamps need to have somewhat specific shapes to fixate the bony piece

of the calcaneus or the tibia, and the lower isolation parts need to be able to slide. Although the initial calculated compressive deflection for the core of the frame (backbone and extrusions) was only 0.01 mm with an applied force to the frame of 30 N (the calculated frame deflection can be seen in Appendix 6.4). A more thorough calculated compressing deflection, including the force-transducer, clamps, and isolators, found that the combined deflection at both clamps was 0.2 mm at 27 N (Fig. 1.8). That value was calculated using the force-transducer and a high-speed camera before and after applying a compressive force of 27 N between both clamps. Because the distance between the upper and lower clamp was 40 mm, the assumed overall strain is $0.005 \left(\frac{0.2 \text{ mm}}{40 \text{ mm}} \right)$ at 27 N.

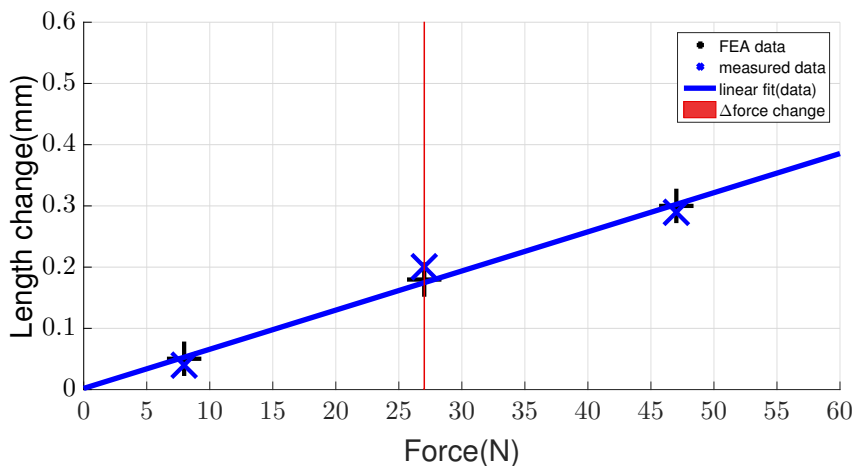


Figure 1.8 |The vertical displacement of the frame clamps in response to static compression. The blue + signs are the captured (cameras) maximum compressive deflection between the upper and lower clamp for either 8 N, 27 N, and 47 N. These three states yielded a compressive deflection of either 0.04 mm, 0.2 mm, or 0.29 mm deflection, respectively. Black x, the deflections between the clamps calculated with a finite element analysis (FEA). The blue, solid line is a linear fit of the measured data (blue +). The vertical, red line is the ΔF span in MTC force in response to impact (falling height: 4 cm).

1.3.3 Inferring kinematics of a running rat

A critical part of this work is to determine an adequate impact. It stands to reason that forced cross-bridge detachment or muscle damage will happen if the impact is high enough. However, the sarcomeres are evolutionarily adapted to meet certain impact conditions, and studying them under their normal working condition range requires adequate determination of the impact force.

During the initial literature review to ensure correct impact condition, only one paper was found that measured the ground-reaction-force (GRF) for a *Rattus norvegicus*, Wistar (trotting at 0.9 m s^{-1}) [86]. Unfortunately, that paper only included the relative stance times for hindlimbs and forelimbs and had no detectable impact peaks in either of the cases. However, others [87] have done extensive work on rodents similar to the Wistar rat by capturing kinematics with cine-radiography and measuring GRF with a custom build runway. The animal in Witte *et al.* (2002) [87] that had the most similarities with the Wistar rat, in terms of morphology and GRF ratio between hindlimb and forelimb stance, was the *Tupaia glis*. Although the *Tupaia glis* did have a clear and visible impact peak, Witte *et al.* (2002) [87] also only included relative stand durations. Therefore, to calculate a realistic impact (see Sect. 1.3.4), it was assumed that the Wistar rat and the *Tupaia glis* have the same stride duration as the *Rattus norvegicus*, Berkenhout rat, which is approximately 100 ms [88]. Table 1.1 lists the *Tupaia glis* and the Berkenhout rat with their data used to estimate the impact force and time to impact peak for a Wistar rat trotting at $\approx 1 \text{ m s}^{-1}$.

Paper	Witte <i>et al.</i> [87]	Schmidt and Biknevičius [88]
Mammal species	Tupaia glis [†]	Berkenhout
Average mass	150-210 g ^{††}	420 g ^{††}
Running speed	N/A	1.0 m s⁻¹
Stance (hindlimb)	normalised(0-1)	100 m s
Impact peak (time)	10 % of stance phase	not clearly detectable
GRF of impact peak	not clearly detectable	70 (% of BW)

Table 1.1 | Comparison of data of similar size mammals to calculate impact force. The data used to calculate the estimated impact force for a Wistar rat trotting at 1.0 m s^{-1} (rounded from 1.3 m s^{-1}) are written in bold.

[†] The animal in Witte *et al.* 2002 with the most similar GRF ratio between hind and forelimb stance compared to the Wistar rat [86].

^{††} An adolescent Wistar rat can have a mass up to 500-600 g [89, 90].

1.3.4 Determining the impact

Choosing a proper contact material is vital to emulate an impact in a rat hindlimb when running. If the chosen contact material's stiffness is too high, the applied impulse ($p = F \cdot dt$) to the GAS becomes too high as well. Vice versa, if the contact material has low stiffness, then the applied impulse to the GAS will be too low compared to what a rat experience in its natural environments. Table 1.2 gives the values used for finding a proper impact material to emulate the impact when the rat makes touch-down running at 1 m s^{-1} .

Data	description	Unit	Source
0.045	mass	kg	42 g + 3 g (\approx frame+GAS mass)
9.81	gravity	m s^{-2}	
0.04	falling height	m	emulating rat running at $\approx 1 \text{ m s}^{-1}$
0.01	$\text{imp}_{\text{duration}}$	s	see Table 1.1
0.00012	cube area	m^2	estimated in Eq. 1.47
0.01	cube height	m	estimated in Eq. 1.47

Table 1.2 | The data used to infer impulse and impact material. The data used to estimate the impulse and what Young’s modulus the contact material should have.

An impact can be mathematically described as the period (T) assuming a simple harmonic motion, where the time t of the period is equal to the reciprocal of the frequency (f)

$$t = \frac{1}{f} = T \quad . \quad (1.40)$$

The frequency itself is equal to

$$f = \frac{\omega}{2\pi} \quad , \quad (1.41)$$

with ω being the angular frequency. If the cause of oscillation is due to a force and that force is a linear restoring force, then the lengthening and shortening of the material is sinusoidal. Therefore, the angular frequency, in a simple

harmonic motion, can mathematically be described as

$$\omega = f 2 \pi = \sqrt{\frac{k}{m}} \quad . \quad (1.42)$$

This is because hook's law dictates that when applying a force to a material, the elongation of that material can be determined by mass (m) and stiffness (k). Knowing the frequency is the reciprocal of time (Eq. 1.40) and substituting ω in Eq. 1.41 with Eq. 1.42 time t is

$$t = \frac{2\pi}{\sqrt{\frac{k}{m}}} \quad (1.43)$$

With

$$k = m \left(\frac{2\pi}{t} \right)^2 \quad . \quad (1.44)$$

Thus, for these impact calculations, the contact material that decelerates the frame must have a stiffness of $2.2 \cdot 10^4 \text{ N m}^{-1}$ as

$$k = 0.045 \text{ kg} \left(\frac{2\pi}{0.01 \text{ s}} \right)^2 \quad (1.45)$$

$$\approx 1.8 \cdot 10^4 \text{ N m}^{-1} \quad (1.46)$$

with 0.045 kg being the combined frame and GAS mass (Table 1.2) and 0.01 s being the time between TD and impact peak (see Table 1.1).

The dimensions of the contact material was somewhat predetermined by the frame size and the surrounding hook parts. With this in mind, the dimensions were given beforehand and subsequently adjusted in Eq. 1.47 to match Young's modulus of a known material that was easily accessible (for final polystyrene cube dimensions, see Table 1.2) . In this case, an estimated 2.2 GPa (Eq. 1.47) corresponded well with the know pascal value in

polystyrene (3 GPa for low polystyrene value¹)

$$E = \frac{k A}{h} = \frac{2 \cdot 10^4 \text{ N m}^{-1} \cdot 0.00012 \text{ m}^2}{0.01 \text{ m}} = 2.4 \cdot 10^6 \text{ Pa} \quad . \quad (1.47)$$

With this material property and time between TD and impact peak (see Table 1.1), the impact force will be 4.0 N (Eq. 1.48), which is in good agreement with rat impact forces found in the literature 3.5 N [88] with the weight 500 g of a older Wistar rat [89, 90].

$$F = m \frac{\sqrt{2gh}}{t} = 0.045 \text{ kg} \frac{\sqrt{2 \cdot 9.81 \text{ m s}^{-2} \cdot 0.04 \text{ m}}}{0.01 \text{ s}} \approx 4.0 \text{ N} \quad (1.48)$$

¹<https://www.bestech.com.au/wp-content/uploads/Modulus-of-Elasticity.pdf>

Chapter 2

Methods

2.1 Experimental setup and muscle preparation

2.1.1 Schematic diagram of the experimental setup

In all trials, except for the passive experiments, there was a time difference between reaching isometric force and the falling time of the frame. The time difference between isometric force and impact was also affected by the two variations in falling heights (experiments from either Study 1 or Study 2). Therefore, both the signal that triggered the simulator (red lines in Fig. 2.1) and the output signal that triggered all else (blue lines in Fig. 2.1) were separated throughout all experiments. When the force-transducer and cameras were triggered, they started to record, and the captured data were after each experimental trial transferred back to the computer (black lines in Fig. 2.1). Note that Fig. 2.1 is a simplified drawing, where the connection lines may give the impression of a one-way signal transfer when actually, all signals to each hardware component were looped to detect any possible undesired

hardware delay.

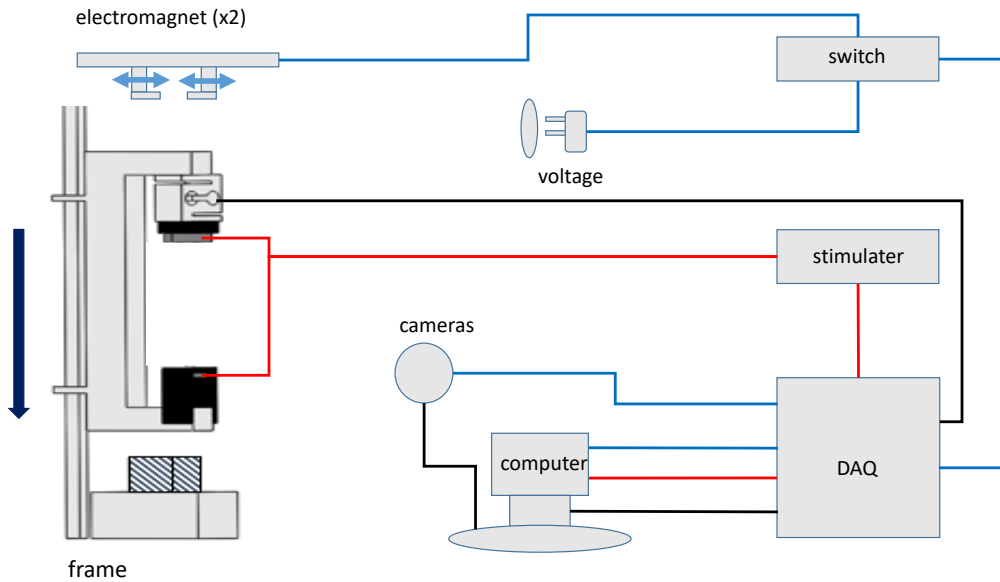


Figure 2.1 | Schematics of the experimental setup. Beyond the frame with the mounted force transducer, the experimental setup also involved cameras, electromagnets, a switch, a stimulator, a data acquisition device (DAQ), external voltage, and a computer to connect all the single hardware components mentioned. The red lines illustrate an outgoing signal. For example, the computer initiates each trial via the DAQ, which includes sending a trigger signal to the stimulator, which subsequently initiates the muscle stimulation via a positive and negative electrode fixed on the frame. The blue lines are also outgoing signals, however, sent with a delay relative to the red lines (see text). The black lines are ingoing signals illustrating the capturing of data from either the cameras or the DAQ sent back to the computer after each trial.

2.1.2 The experimental setup in detail

Besides the frame, detailed in Sect. 2.1.3, the experimental setup needs several other separate hardware components that work together for the experimental setup as a whole to function correctly. These are:

- High-speed cameras
- 2 hub-magnets
- 1 power supply
- 1 stimulator
- 1 switch
- 1 data acquisition device (DAQ).
- 2 stroboscopes (manually operated, not included in Fig. 2.1).

2.1.2.1 High-speed cameras

The cameras used for these experiments are high-speed cameras, capturing data at 1825 Hz (HCC-1000 BGE, VDS Vosskühler, 07646 Stadtroda, Germany) and were equipped with C-mount 25 mm focal length lenses (Xenon 25/0.95, Schneider-Kreuznach, 55543 Bad Kreuznach, Germany). Depending on the experiments, the high-speed cameras had either an extra 1 mm (Study 1) or 3 mm (Study 2) extension tube to increase the focal length. The downside to increasing the focal length is that the light spreads more easily around the object of interest, reducing the camera's depth of field (Fig. 2.2). Each high-speed camera had a pixel resolution of 1024x256 and was controlled via the HCC-1000 software (v5.0.0), intended for a Windows XP operation system. The latter was a minor issue because the software needed

a different frame grabber and external driver from another software to work on a Windows 7 or 10 operation systems (for installation information, see Appendix 6.4).

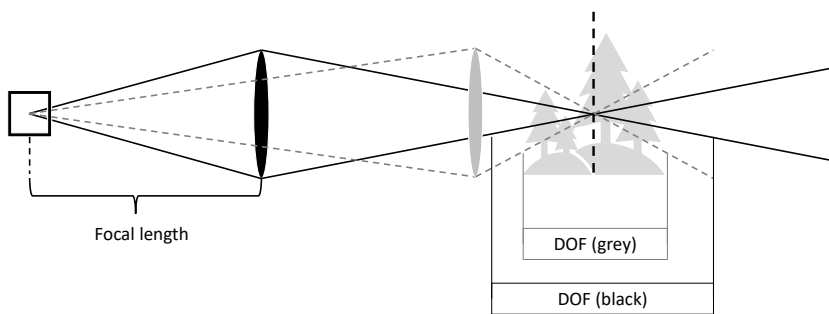


Figure 2.2 |Depth of field. The figure shows how the distance (focal length) from the sensor (black square) to the lens (black ellipse) determines the depth of field (DOF). If the focal length is changed, the distance from the sensor to the grey ellipse, the DOF changes. That is because a longer focal length results in more widespread light arrays (dashed grey lines) around the focal point (vertical, black, dashed line). Outside the DOF, the image of interest is more sensitive to focus (smear) as the light spreads out more.

2.1.2.2 Stimulator

A bi-phase stimulator (701C, Aurora Scientific Inc., L4G 1X6 Aurora ON, Canada) issued outgoing pulses to stimulate the muscle, as long as the external trigger input maintained 2 Volts (gated trigger mode). Through testing and recommendations from a previous work [91], it became clear that to ensure tetanic muscle contraction pulses must be issued as $500 \mu\text{s}$ square wave pulses of 10 V (three times the twitch threshold) at 100 Hz. The duration

of stimulation was 265 ms for Study 1 (Chapter 3) and Study 2 (Chapter 4). However the resting phase between stimulations was 428 s in Study 1 and 254 s in Study 2. This was because of the difference in falling height and a slightly lower factor-of-safety margin between both experimental setups.

2.1.2.3 Stroboscopes

For the camera to capture at 1825 Hz, the exposure time is hard-coded to 0.548 ms, which meant that there was not enough time for the digital sensor inside the high-speed camera to be sufficiently exposed to light. For the latter reason, two stroboscopes (Multiled PxT, GS Vitec GmbH, D-63628 Bad Soden Salmünster, Germany) provided a sufficient light source in each experimental trial. As the frequency of each stroboscope was 20 kHz, they did not interfere with the cameras when manually controlled.

2.1.2.4 Switch, magnets and DAQ

The switch is a custom build device made up of three parts. A 3-pin screw terminal block, a 2-pin screw terminal block and a 12 volt PCB relay (M4-12H), all soldered on a small solder point grid plate. The magnets, which released the frame were two 12 volt hub-magnets (TDS-10A) and the Data Acquisition Device (DAQ) was from National Instruments (Multifunction I/O Device USB-6363, National Instruments Corporation, 11500 N. Mopac Expwy Austin, TX 78759-3504, United States). Because the DAQ can only safely generate an output signal of no more than 5 volts, and the electro-magnets needed 12 volts to release the frame properly, the DAQ and electro-magnets was connected to each other via the switch. The switch increased the voltage signal from 5 to 12 volts via a plug-in power supply (Voltcraft SNG-600-OW, Conrad Electronic AG, 8832 Wollerau, Switzerland).

When the trigger signal arrived from the DAQ (Multifunction I/O Device USB-6363, National Instruments Corporation, 11500 N. Mopac Expwy Austin, TX 78759-3504, United States), an adjusted 12 volts from the power supply (Voltcraft SNG-600-OW, Conrad Electronic AG, 8832 Wollerau, Switzerland) connected directly with the two 12 volt hub-magnets (TDS-10A), which subsequently released the frame. The switch was necessary because the DAQ could not safely generate an analogue output of more than 5 volts, which resulted in time irregularities for the hub-magnets to release the frame.

2.1.3 The aluminium frame in detail

The right-angled, C-shaped aluminium frame had an upper and a lower clamp construction for MTC fixation between its cantilever arms (Fig. 2.3). The backbone of the frame was 120 mm long, its two arms protruded by 40 mm. The total mass of the frame including the force transducer was 42 g. This transducer (KD24S 20N, ME-Meßsysteme GmbH, 16761 Henningsdorf, Germany), amplified with an analogue measuring amplifier (GSV-1H 010/250/2, ME-Meßsysteme, 16761 Henningsdorf, Germany), was positioned above the upper clamp, insulated from the latter by a plastic cuboid (Fig. 2.3, all insulators are shown in dark blue). The lower clamp was an aluminium hook jig connected to the frame via two, shiftable, inverted-U-shaped plastic insulators allowing MTC length adjustment. For MTC fixation, the femur piece was placed between the two upper, U-shaped clamps which were then screwed to their third, inverted-U-shaped counterpart. At the MTC's opposite end, the calcaneus bone piece was placed in the hook jig of the lower clamp.

A rectangular aluminium profile, serving as a rail for the frame, was fixed on the base plate of the whole experimental device. After being released with an electromagnet, the frame fell freely, but guided (white double arrow

for indication) by the rail, and was eventually decelerated by compressing a polystyrene cuboid with mass 0.041 ± 0.0001 g and ≈ 1 cm² surface area (see Table 1.2). Both the electromagnet and the polystyrene were in vertical alignment with the overall frame-muscle centre of mass. To ensure minimal rebound and oscillation of the frame after TD, two hooks on the lower part of the frame were locked in under the horizontal pin at maximum polystyrene compression (mechanism indicated in Fig. 2.3 by red, dashed, curved and straight arrows). For minimising jerk the hook tips were covered with a rubber layer.

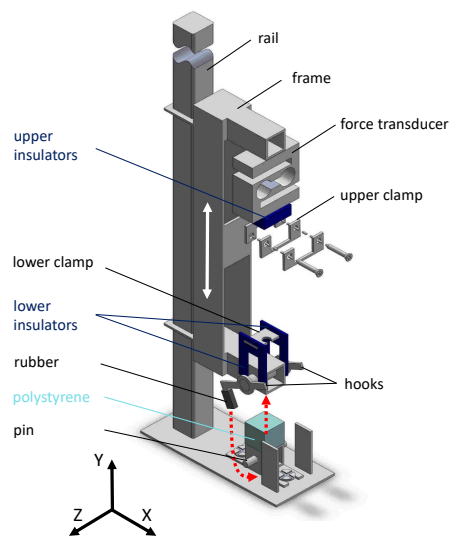


Figure 2.3 |The C-shaped frame, which was freely movable (symbolised by the white double arrow) in the direction along the rail. Red dashed arrows indicate hook movement initiated by the reaction force from the solid aluminium plate at TD. This figure is from Christensen *et al.* (2017)[92], reproduced with permission from Springer Nature.

2.1.4 Ethical approval

All extracted GAS specimens ($N = 16$) were from freshly killed rats (*Rattus norvegicus*, Wistar) provided by another animal study approved according to Section 8 of the German animal protection law (Tierschutzgesetz, BGBl. I 1972, 1277; Thüringer Landesamt für Verbraucherschutz, Abteilung Gesundheitlicher und Technischer Verbraucherschutz). In that study, the rats were anaesthetised by intraperitoneally injecting sodium pentobarbital (100 mg per 1 kg body mass). Any possible replenishment of the sodium pentobarbital injection (10 mg per 1 kg body mass) was regulated by checking the in-between toe reflex, the corneal reflex, and the ear pinch reflex. Pentobarbital targets the brain and nervous system and is the most used medium-long acting drug in most common in veterinary medicine. Pentobarbital belongs to the anaesthetic class of barbiturates[93]. Furthermore, the approved study performed experiments on other leg muscles, and the applicants had no objection against GAS extraction immediately after the rats' death. The results of their experiments were not impaired by GAS extraction.

All sixteen animals were raised in an institute for animal science (Institut für Versuchstierkunde und Tierschutz, Dornburger Straße 23, 07743 Jena, Germany). There, official veterinarians regularly ensured the welfare and care of the animals. The subsequent death and animal experiments also took place at the same institute for animal science. Of the sixteen rats, nine animals were in the first set of experiments (Study 1) and five animals in the second set of experiments (Study 2). The last two animals were for the preliminary testing.

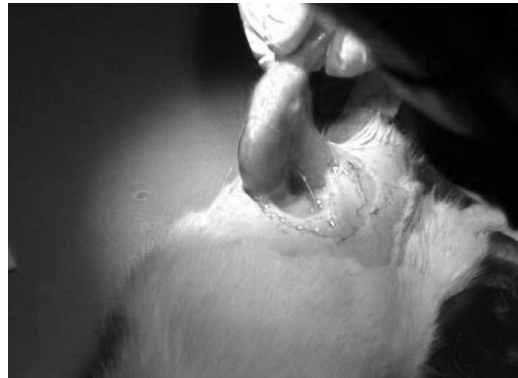
2.1.5 Preparation of the muscle (GAS)

Here is the experimental procedure for dissecting the GAS in numbered list form:

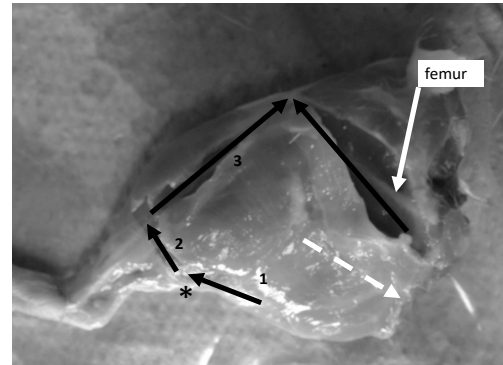
1: Shave the rat leg free of hair from the hip and down. **2:** Cut the skin at the hip joint with a circular cut around the leg. Cut in a straight line down to after the ankle joint and make a circular cut there. Now, the skin can be removed easily from the hip and downwards.



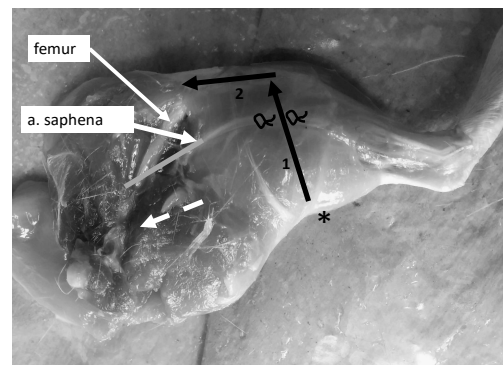
3: Remove the fascia from the hip and free the leg from the torso (done with stretching fascia free from muscle).



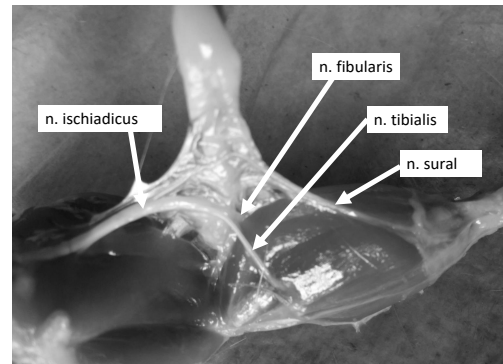
4: Stretching the leg, a distal cut in *m. semitendinosus* without damaging *m. gastrocnemius* (arrow 1) is possible and safe to perform. Continue this cut to natural resistance is met (star), cut to the insertion of *m. biceps femoris* (arrow 2) and along with the insertion to the patella (arrow 3). Cut between *m. biceps femoris* and *m. gluteus superficial* (arrow), so the femur becomes visible, and the *m. biceps femoris* can be flipped backwards (dashed, white arrow).



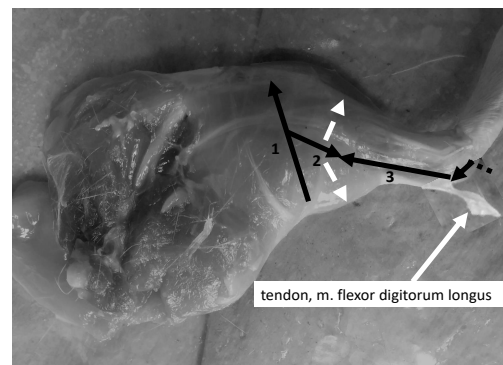
5: From the end of the previous distal cut (star here and in the previous picture), cut to the insertion of *a. saphena*, where the blood vessels are small. Make two knots on *a. saphena* to restrict blood flow and cut through. Continue the cut along with the insertion to the patella (arrow 2). Flip *m. gracilis cranialis* (dashed, white arrow).



6: Leave nerves and blood supply (not visible here) until step **10**.

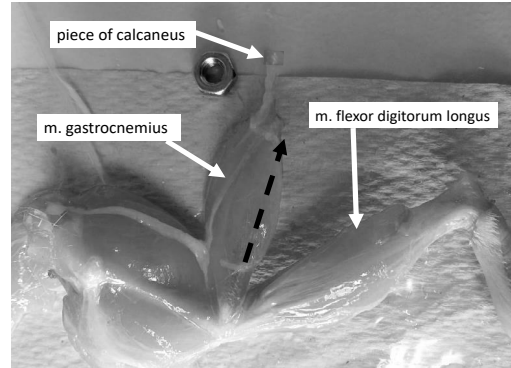


7: From the previous cut in step **5** (arrow 1), cut close to *a. saphena* (arrow 2). Snip the tendon of *m. flexor digitorum longus* from under the paw. Stretch the tendon away from the leg for the tendon to be cut free (cut along arrow 3). Continue this stretch-and-cut procedure until the *m. flexor digitorum longus* is free from the distal part *m. gastrocnemius*. Now, free the lower part of *m. gastrocnemius* in the direction of both dashed, white arrows.

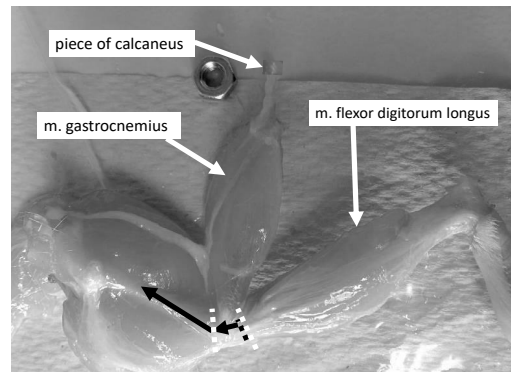


8: cut the calcaneus halfway through (dashed line) to avoid damage to the underlying blood supply. The rest of the calcaneus will break as a result of the cut.

9: Use the Achilles tendon the bony calcaneus piece to free the tendon of *m. gastrocnemius* from its surroundings. Thereafter, use the tendon of *m. flexor digitorum longus* to free the *m. flexor digitorum longus* from *m. gastrocnemius* to the knee joint. At the origin of *m. soleus*, between *m. gastrocnemius medialis* and *lateralis*, remove *m. soleus* from *m. gastrocnemius* (dashed arrow).



10: Make sure all fascia, blood supply, and nerves covering the *m. gastrocnemius* are removed. **11:** cut the tendon below the patella, and free the knee joint by cutting the *m. biceps femoris* along the femur on both the medial and lateral side (black arrow, lateral). When the knee joint is free, completely remove *m. gastrocnemius* by cutting the bone on either side of the muscle origin (white, dashed lines).



2.1.6 Direct muscle stimulation

The MTC of the GAS was freed from its surrounding tissues with the exception of small bone tissue pieces of the calcaneus and femur for fixating the MTC in the frame. With a positive electrode wired to the upper frame clamp and a negative electrode around the lower clamp, direct stimulation of the muscle was ensured. Due to poor tendon conductance an extension

of the negative electrode was bluntly put into contact the dorsal part of the muscle belly between *m. gastrocnemius medialis and lateralis* at the distal fibre-tendon junction, where the electrode was held in place by the muscle tissue adhesiveness. The muscle was stimulated (Aurora Scientific 701C) with $500\ \mu\text{s}$ square wave pulses of 10 V (three times the twitch threshold) at 100 Hz to ensure tetanic contraction during the trials, as recommended in a previous paper [91]. Experiments were conducted with the GAS contracting isometrically at optimal fibre length while falling. The series of falling experiments with each specimen were finalised by a trial without stimulation, i.e., with passive muscle fibres. To prevent desiccation, the GAS surface was moisturised once between trials with Ringer's solution of 38°C temperature from a small spray flask. The experiments were conducted at room temperature ($23\text{-}25^\circ\text{C}$).

2.2 Methods (Study 1)

In Study 1, the falling height of the frame emulates a rat running at approx. $1\ \text{m s}^{-1}$ (4 cm height falling height). For more information on both surface stiffness and the falling height, see Sect. 1.3.4. All experiments were done with fully active muscles, except for the last trial, which was performed with the stimulation switched off (passive). The muscle force was measured by a force transducer serving as a rigid connector between the suspending clamp of the upper tendon and the frame.

2.2.1 Data acquisition, marker tracking, and digital filtering

To study the shock-wave-induced kinematics of rat GAS muscles *ex vivo* (see Sect. 2.1.6), the frontal area of the GAS was patterned by pressing the muscle belly on a prepared array of high-grade steel markers (spheres, nominal diameter 0.4 mm, mensuration N0, IHSD-Klarmann, 96047 Bamberg, Germany) as seen in Fig. 2.4c. The GAS was then fixed in an aluminium frame (Fig. 2.4a), which was dropped on the ground. Local muscle kinematics was recorded with two high-speed cameras, each recording 256x1024 pixels per sample at 1825 Hz (Sect. 2.1.2.1). The cameras were placed along a semicircle with radius of ca. 15 cm on the open side of the C-shaped frame, and all were focused on the frontal surface of the belly located in the semicircle's centre. The imaging planes were aligned in parallel to the vertical (rail) axis. Two-dimensional images from a particular camera were respectively calibrated, including distortion correction in linear proportion to distance to the image centre. After automatic marker tracking using 'DigitizingTools' (Hedrick Lab, University of North Carolina, Chapel Hill, USA; coded in MATLAB, The MathWorks, Natick, USA), the marker positions were digitally filtered using a moving average with a symmetric window of five samples. Accelerations were calculated with a symmetrical, first order (two point) central difference formula.

2.2.2 Detecting touch-down (TD) and calculating strain

Touch-down TD was the point in time when the frame made contact with the polystyrene. It was determined in each trial as the point before the earliest instant at which the second time derivative of the COM position (acceleration;

a_{COM}) had raised above noise level. As no delay between the acceleration signals of frame and COM was detectable in all experiments around TD, either signal could be used in principle to determine TD. However, detecting TD with the COM acceleration was favourable because this method proved more reliable than using frame marker acceleration. Although an extended template size (spatial noise of just 0.1 pixel) was possible for frame marker tracking, a slightly better signal-to-noise ratio could be achieved using an array (individual noise: 1 pixel) of belly markers (see also sub-pixel resolution in Appendix 6.4).

To determine belly strain ϵ_{CE} , an upper and lower range of each $\sim 10\%$ of total muscle length was identified. The vertical placement of both marker subarrays was nearly symmetrically positioned around the midpoint of the belly (location of maximum cross-sectional area $A_{CE,0,max}$), as seen in Fig. 2.4c. The horizontal, white lines across the belly represent the subarray limits and thereby confine the denotation ‘contractile element’ (CE) in this work. The representative vertical position of each marker subarray (y_u and y_l with u for ‘upper’ and l ‘lower’) was calculated as the arithmetic mean of the vertical positions of all markers in this subarray. In Fig. 2.4c, the aponeuroses extend on both lateral sides of GAS, i.e., the field of view. Thus, by solely using markers from the centre of the y_u and y_l regions, care was taken to analyse the kinematics of fibres alone rather than any aponeurosis material. The calculated fibre material strain $\epsilon_{CE} = \Delta L_{CE}/L_{CE,0}$ was calculated with the length L_{CE} spanning the fibre material in the centre of the muscle belly and a corresponding reference length $L_{CE,0}$: $\Delta L_{CE} = L_{CE} - L_{CE,0}$. The reference length that defined zero percent strain $L_{CE,0} = y_u - y_l$ was the distance between the mean vertical positions of an upper (y_u) and a lower (y_l)

marker subarray measured at TD in each trial. Each subarray contained four to eight markers. The reference length was the trial-specific L_{CE} at frame touch-down. The reference length of the COM ($L_{COM,0}$) was the COM's vertical distance to the frame marker at TD, and $\Delta L_{MTC} = L_{COM} - L_{COM,0}$ is the corresponding MTC displacement after TD.

2.2.3 Calculating ΔF , the CE stiffness (K_{CE}), the MTC stiffness (K_{MTC}), and inferring the tendon-aponeurosis-complex stiffness (K_{TAC})

Beyond describing CE-internal kinematics by strain ϵ , Newton's second law $\Delta F = m \cdot (a_{COM} + g)$ was used to calculate the dynamic force change ΔF between MTC ends in response to the impact. The symbols are: muscle mass m , COM acceleration a_{COM} , and gravitational acceleration g . The COM position is calculated as the arithmetic mean of all steel marker positions on the muscle (detailed in Fig.2.4 legend).

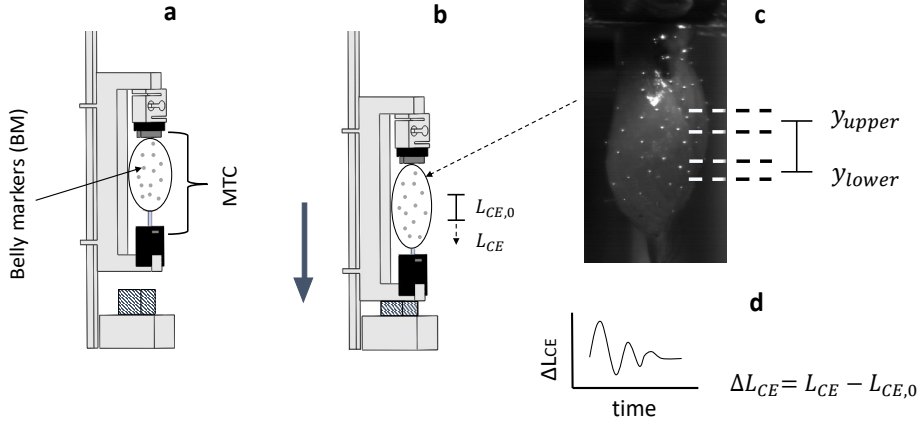


Figure 2.4 | Drawing of the experimental frame. **a:** the frame before TD. GAS is fixed between the upper and lower clamp (solid dark-grey rectangles). Above the upper clamp is an insulator (solid, black rectangle) and the force transducer, respectively, which are both fixated to the frame backbone (squared C-shape). The solid, black insulators prevent muscle stimulation to interfere with the force transducer. The light-grey spots on the muscle belly are illustrating the steel markers that pattern the muscle belly, which we used to calculate the dynamic force change between MTC ends in response to the impact ($\Delta F = \overline{BM} \cdot m = a_{COM} \cdot m$) after TD, with m being the GAS mass, \overline{BM} the arithmetic mean of all belly markers' vertical (y) positions and a_{COM} the correspondingly estimated acceleration of the centre of mass. **b:** the frame after TD with the polystyrene (hatched rectangle) being compressed. In **b**, the belly's stretch response to the impact is drawn exaggerated. **c,:** a video frame image of the muscle belly from one of the trial cameras, where the white spots are the steel markers, and the dashed, black lines are the upper and lower limits of the horizontally spread upper and lower ranges of CE markers for which y_{upper} and y_{lower} , respectively, symbolise the arithmetic means of the vertical marker positions in each the upper and the lower range. **d:** an example of how ΔL_{CE} changes over time, after TD. A more detailed description of the functionality of the frame is given in Sect. 2.1.3. This figure is from Christensen *et al.* (2021) [94], reproduced with permission from Springer Nature.

Because CE mass is much higher than the tendon-aponeurosis-complex

(TAC) mass, ΔF also approximates the dynamic force change between CE ends well. Since the dynamic force change ($\Delta F(t)$) as well as MTC deflection relative to the frame $\Delta L_{MTC}(t) = (y_{COM}(t) - y_{frame}(t)) - (y_{COM}(t = 0) - y_{frame}(t = 0))$ and CE-internal elongation $\Delta L_{CE}(t)$ are all known as functions of time t in each single trial, the k_{MTC} and k_{CE} can be calculated based on all data points in the respective force-elongation relations $\Delta F(\Delta L_i(t))$ between TD and the instant of maximum centre of mass acceleration $a_{COM,max}$ (examples in Fig. 2.5). Accordingly, all presented k_{MTC} and k_{CE} data are estimated with the 3-parameter fit

$$F(L_i(t)) = k \cdot L_i(t) + b + d \cdot \dot{L}_i(t) \quad (2.1)$$

using three parameters k , b , d to fit a linear function $F(L_i, \dot{L}_i)$ to measured data with i being either $i = \text{CE}$ or $i = \text{MTC}$ and $F = \Delta F$. This overdetermined linear equation system for k , b and d is solved by the Matlab operator “\”. For comparison, the effect on estimating k_{MTC} when neglecting the damping parameter d is shown in Fig. 2.5 (slope of ‘2 parameter fit’).

From this, the stiffness

$$k_{TAC} = \frac{K_{CE} \cdot K_{MTC}}{K_{CE} - K_{MTC}} \quad (2.2)$$

of the ‘tendon-aponeurosis complex’ (TAC) was inferred based on the model idea that the MTC consists of a mass that is suspended to the frame (or bone) by two compliant elements arranged in series (CE and TAC) given the overall MTC and the local CE stiffness values.

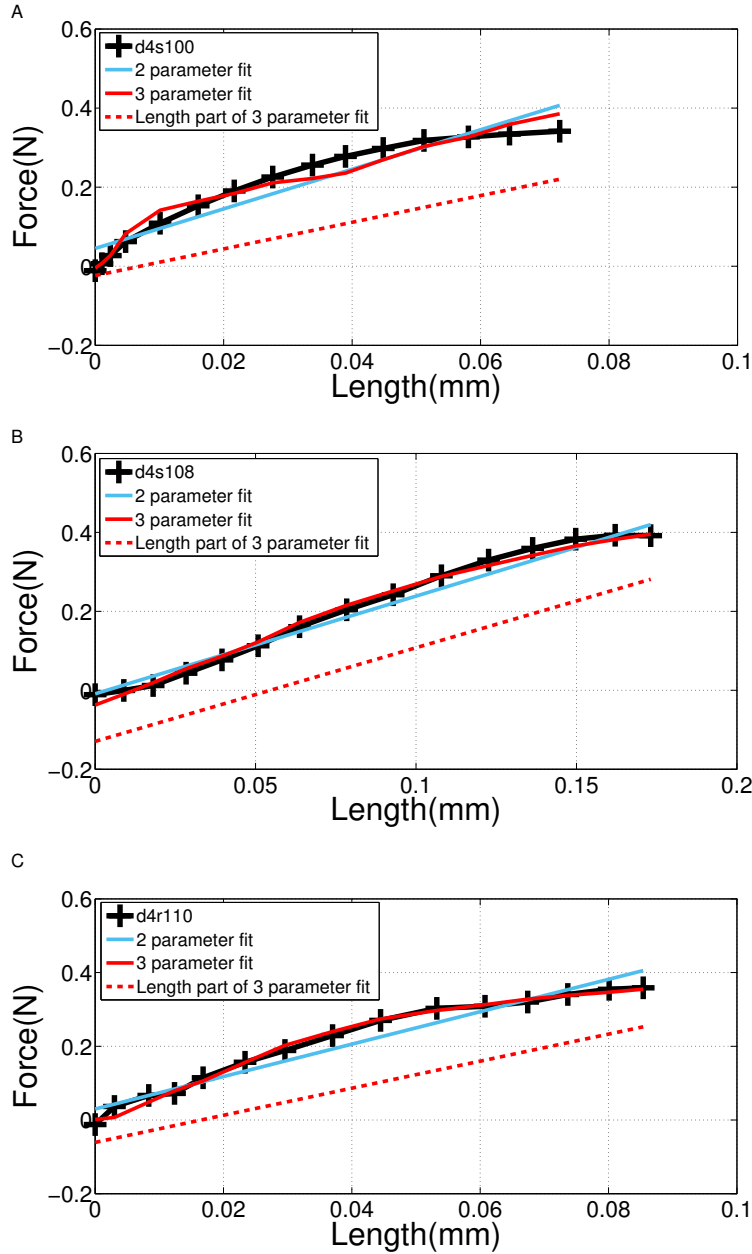


Figure 2.5 | Force change ΔF versus displacement ΔL_{MTC} of the MTC's COM in the initial phase (ca. 5 ms starting with TD) of shock-wave-induced strain. Panels from top to bottom show examples for three trials of the same muscle specimen 'd4s1': 'd4s100', 'd4s108', 'd4s110' (crosses). The dynamic force change ΔF is calculated as the corresponding vertical acceleration a_{COM} of the MTC's COM (right y-axis in Fig. 3.3) plus gravitational acceleration and multiplied by the muscle mass m . The red, solid line is the 3-parameter fit to data using Eq. 2.1 with the light-blue line being the length part of this k_{MTC} fit. The slope of '2 parameter fit' is k_{MTC} when neglecting the damping parameter d . This figure is from Christensen *et al.* (2017) [92], reproduced with permission from Springer Nature.

2.2.4 Exclusion criteria

Not all data were suitable for use within these analyses; therefore, exclusion criteria at different stages of the data processing were used. In particular, excluding the following: (I) an entire trial if the force at TD was less than 95% of the trial-specific isometric force, where the latter was determined as the force value to which the force transducer signal converged shortly before or after the impact response (see also Fig. 2.6); (II) an entire trial if material shortening ($\epsilon_{CE} < 0$) preceded material elongation as an initial response to TD (e.g., Fig. 2.7, bottom); (III) a marker in a trial if it had obviously glided across the muscle surface during the experiment; and (IV) a marker in a trial if it showed phase and/or amplitude irregularities (either in coordinate position or acceleration) when compared to all other markers. Note that all data analysed and presented did not meet the exclusion criteria (I)-(IV). As an exception, data regarding the initial force, which are shown in Fig. 3.1 and Fig. 4.1 only needed to pass criterion (I).

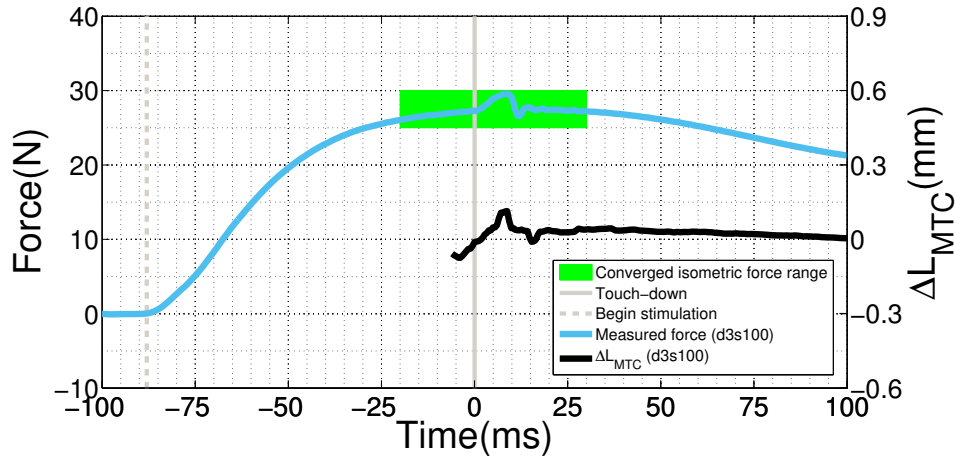


Figure 2.6 | Example of experimental data: MTC force and MTC length around touch-down. Light blue, thick line: force transducer signal (left y-axis). Black, thick line: MTC length excursion ΔL_{MTC} (right y-axis) from MTC length $L_{MTC,0}$ at TD. Vertical, dashed line: start of stimulation at $t = -87$ ms. Vertical, grey line: touch-down (TD) at $t = 0$. The green, shaded area indicates the time period in which the isometric force F was determined as the maximum low-frequency value from the force transducer trace, that is, with additionally excepting the (high-frequency) impact period from TD to 15 ms later. Usually, F was the value to which the force trace converged in the 10-15 ms after the impact period. The force decreased thereafter, which was a reproducible characteristic phenomenon in these experiments, particularly in the least fatigued muscles. In some experiments, the maximum in the force trace, except for the impact peak, was reached before TD. If force at TD and isometric force F differed by more than 5%, the trial was excluded from analysis (see sect. 2.2.4). This figure is from Christensen *et al.* (2017) [92], reproduced with permission from Springer Nature.

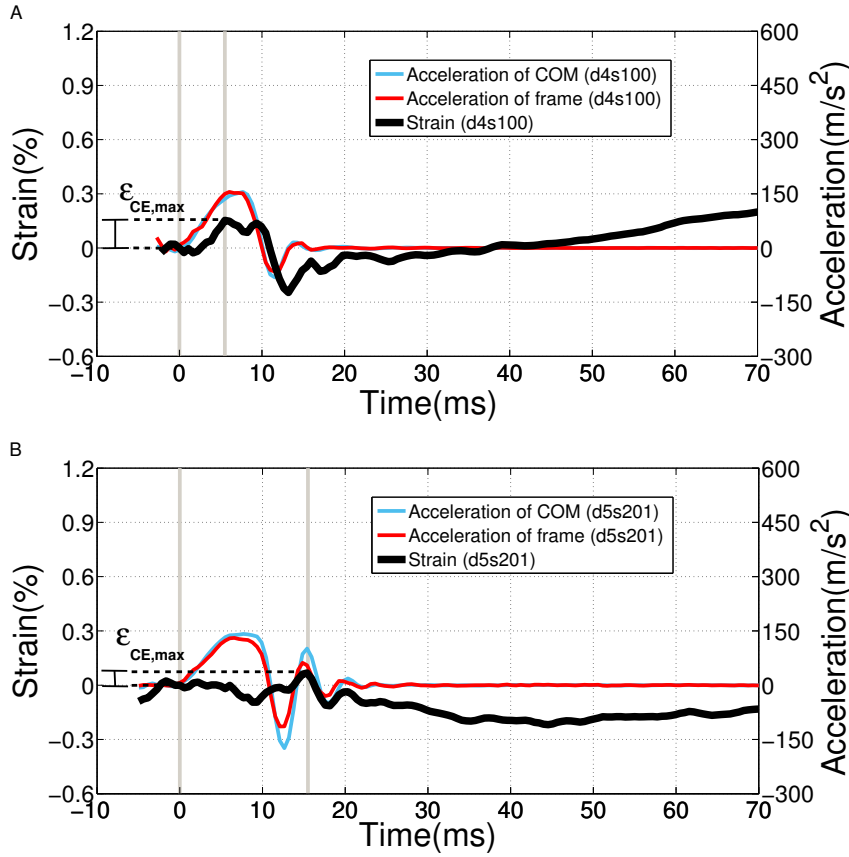


Figure 2.7 | An example of CE strain inclusion or exclusion. Plots of the local fibre material strain ϵ_{CE} (black, thick, solid line: $\epsilon_{CE} = 0$ at TD), net vertical MTC acceleration a_{COM} (light blue, thin, solid line) – that is, the arithmetic mean of all steel markers’ values approximating centre of mass (COM) kinematics – and vertical acceleration of the suspending frame a_{frame} (dark red, thin, solid line) for trials ‘d4s100’ (A) and ‘d5s201’ (B). Vertical, grey lines indicate time instants of TD ($t = 0$ s) and maximum dynamic strain amplitude $\epsilon_{CE,max}$ during shock response $t > 0$ s. The bottom trial ‘d5s201’ was *excluded* from the analysis because its earliest extreme in strain (at ca. 9 ms) was a *minimum* rather than a maximum as in the top trial ‘d4s100’ (at ca. 4.5 ms). This figure is from Christensen *et al.* (2017) [92], reproduced with permission from Springer Nature.

2.3 Methods (Study 2)

In Study 2, the falling height of the frame emulates a rat running at approx. 0.5 m s^{-1} (1 cm falling height). For more information on both surface stiffness and the falling height, see Sect. 1.3.4 and Sect. 2.3.1. The basis of the processing of data in this chapter are the same as described in Sect. 2.2 for Study 1, with the exception that each camera is processed separately and a new location for the frame marker was used due to the previous frame marker's potential erroneous influence in estimating energy dissipation and damping coefficients (Sect. 2.3.3). All experiments were done with fully active muscles, except for the last trial, which was performed with the stimulation switched off (passive). The muscle force was measured by a force transducer serving as a rigid connector between the suspending clamp of the upper tendon and the frame.

2.3.1 Lowering the falling height

The falling height for an impact corresponding to a rat running at 1 m s^{-1} was inferred in Sect. 1.3.4. The relation between falling height (h) and the mean (ground reaction) force on the frame during the impact (ΔF_{imp}) arises from combining the conservation of mechanical energy (Eq. 2.3) and the impulse-momentum equation (Eq. 2.4),

$$mgh = \frac{1}{2} m v^2 \rightarrow v = \sqrt{2gh} \quad (2.3)$$

and

$$p = mv = \Delta p \rightarrow \Delta F_{imp} = \frac{\Delta p}{\Delta t} = \frac{m\sqrt{2gh}}{\Delta t} \quad , \quad (2.4)$$

respectively, with m being the frame mass (42 g, twenty-one times higher than GAS mass: Table 4.1), v the frame's TD velocity, p the frame's linear momentum at TD, Δp its change (impulse) during the impact of duration Δt and g the gravitational acceleration. Thus, lowering the falling height to 1 cm will reduce the impact with a factor of 0.5 (Eq. 2.4). An example of the impact difference is shown in Fig. 2.8.

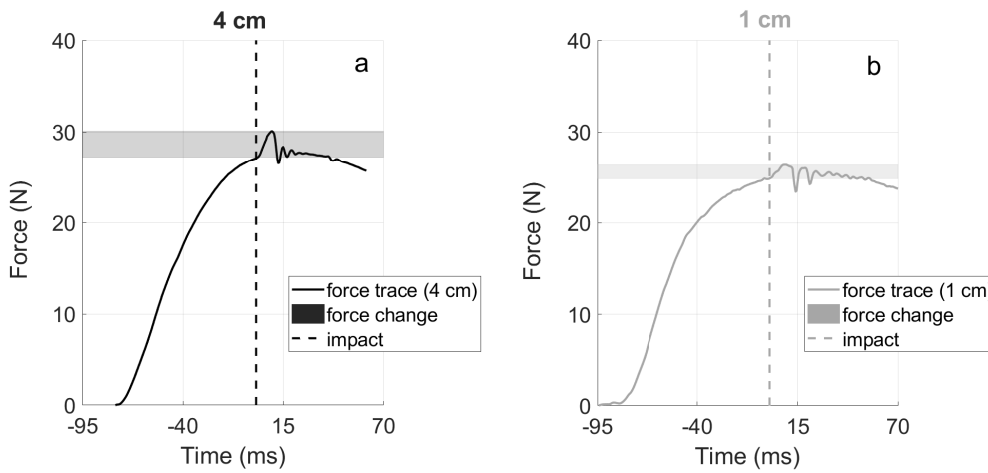


Figure 2.8 | The measured isometric force traces in two trials for two different falling heights. The black solid lines and grey solid line are the isometric muscle force measured by the force transducer in falling heights of either 4 cm (a) or 1 cm (b), respectively. The black dashed line and the grey dashed line are the measured isometric forces just before impact, in falling heights of either 4 cm or 1 cm, respectively. The hatched areas in both a and b are the increase in the measured isometric force due to an impact in experiments of either 4 cm or 1 cm falling heights, respectively.

2.3.2 Determining work-loop

Similar to Sect. 2.2.3, with known values for length ($L(t)$) and length rates ($\dot{L}(t)$), stiffness k_{CE} , k_{MTC} and damping d_{CE} and d_{MTC} properties were inferred from the 3-parameter function in Eq. 2.1.

Contrary to Study 1, the force-displacement data in Study 2 were analysed

using Eq. 2.1 in the period between TD and when a_{COM} returned to zero for the second time (≈ 17 ms, Fig 2.9). The area enclosed by such a loop is approximated, for both MTC and CE, using the Right Riemann summation method.

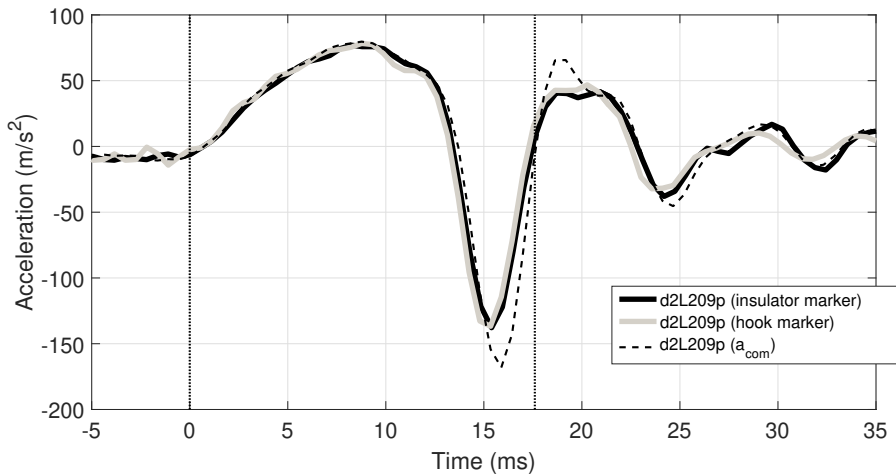


Figure 2.9 | Example of noise and delay in frame marker acceleration before and after TD. The solid, black line is the acceleration of the frame marker located at the left, lower insulator. Solid, grey line is the acceleration of the frame marker located on the lower clamp. The solid, grey line leads solid, black line with 0.5 ms (1 frame) in d2L209p. This trailing tendency was examined in 23 trials, and at no point was *insulator* earlier than *hook*. In addition, the solid, grey line never led with more than 0.5 ms. In few trials no delay was found. The dashed, black line is a_{COM} signal for this trial and the dotted, vertical, black lines indicate the span between TD and when a_{COM} returns to zero for the second time. This figure is from Christensen *et al.* (2021) [94], reproduced with permission from Springer Nature.

2.3.3 Dealing with the non-synchronicity of cameras and the critical choice of the marker on the frame

To calculate work-loops and damping coefficients in MTC and CE in response to impacts, it was necessary to remove two potential sources of systematic

errors in the data analysis. Figure 2.9 shows the acceleration signals of two different marker positions on the frame (*hook* and *insulator*). The *hook* marker was on the aluminium part of the lower clamp, formed as a hook, and the *insulator* marker was on the outside of the left, lower insulator (see Fig. 2.3). In general, while the *hook* marker had a higher noise-to-signal ratio than the *insulator* marker, the *hook* systematically led the *insulator* trajectory by 0.5 ms. The latter finding is decisive for the calculation of reliable work-loops. The influence of the frame marker position used to calculate ΔL_{MTC} with and without a 0.5 ms frame marker delay are shown as examples in Fig. 2.10b and a, respectively. Accordingly, the MTC was found to dissipate $45.6 \mu\text{J}$ during one full oscillation period after TD if *hook* was used to calculate ΔL_{MTC} (no marker delay), while only $2.7 \mu\text{J}$ would be calculated if *insulator* was used to calculate ΔL_{MTC} (marker delay).

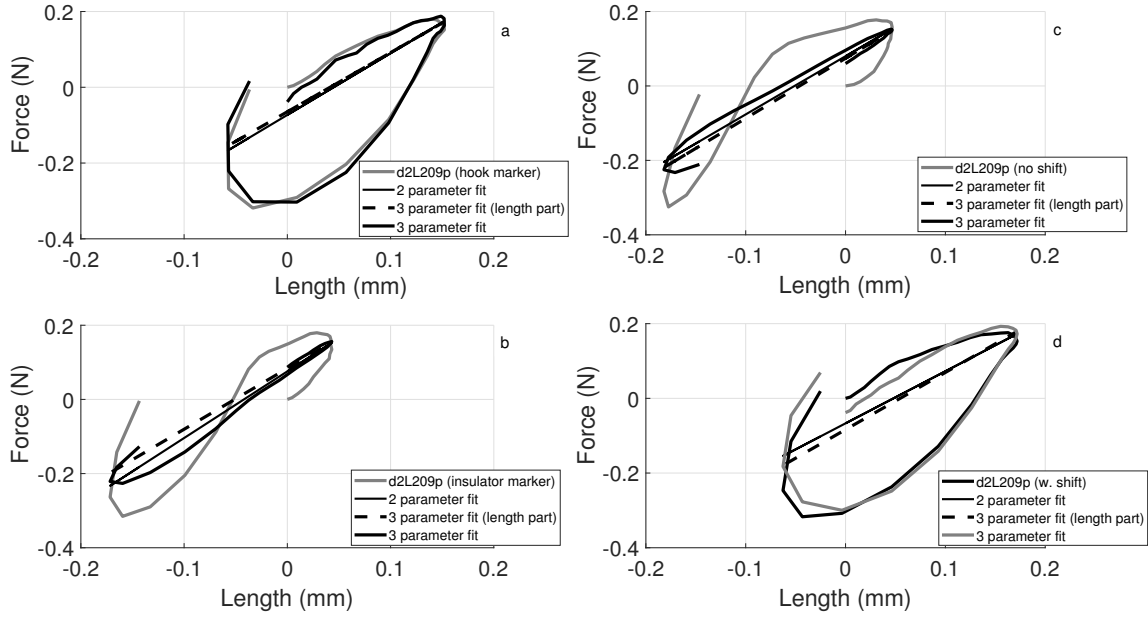


Figure 2.10 | An example of time delays effecting the work-loop in trial d2L209p. **a** The *hook* marker, which had a systematic 0.5 ms lead on the *insulator* marker (Fig. 2.9), was used to calculate ΔL_{MTC} , based on one camera view. **b** *insulator* used to calculate ΔL_{MTC} , based on the same view. **c**, d2L209p with the one frame shift between the two cameras as determined by MinPos (Table 2.1). **d** d2L209p with a one frame enforced shift between the two cameras, ignoring the time delay determined by MinPos. In **a,b,c,d**, the solid, grey line is the measured $\Delta L_{MTC}-\Delta F$ response (work-loop) to the impact. The solid, thin, black line is the respective linear 2-parameter (force (length)) fit to the data. The solid, black loops depict the respective 3-parameter fits to the data, using the parameters k_i, b_i, d_i of each the function $F_i(L_i, \dot{L}_i)$ (see Eq. 2.1), which linearly depends on length L_i and time rate of length change \dot{L}_i ; the dashed, black line is the respective length-dependent contribution. d2L209p work-loop encompasses one oscillation period that spans between TD and the instant closest to zero when a_{COM} returns to zero for the second time (Fig. 2.9). **a** is the same figure as Fig. 4.4b. This figure is from Christensen *et al.* (2021) [94], reproduced with permission from Springer Nature.

The frame marker used to calculate ΔL_{MTC} should ideally not even be on the lower clamp, rather, on the bony tissue of calcaneus or femur to guar-

antee the elimination of any potential frame property interference. In these experiments, however, both bony tissues proved unreliable for marker tracking.

The VDS Vosskühler cameras used in these experiments (see Sect. 2.1.2.1) had an internal hardware buffer (ring buffer), thus, when the cameras were ready to record, waiting for an external hardware trigger, images started to fill the internal camera buffer memory (continuously removing the earliest entry when full). The ring buffer then potentially may or may not add a 0.5 ms ($\frac{1}{1825}$ Hz) offset to one of the two cameras, when the hardware trigger impulse enters. This potential recording discrepancy made the analysis susceptible to a similar effect as the frame marker delay above. In Fig. 2.10c (same trial as above), no camera offset (uncorrected data) yielded a negative energy dissipation of $-14.6 \mu\text{J}$ for the MTC as a mean of both cameras. On the contrary, a manually enforced 1-frame delay (0.5 ms) to one of the two cameras resulted in a mean MTC energy dissipation of $51.5 \mu\text{J}$ (Fig. 2.10d) during one full oscillation period after TD.

Nonetheless, some calculated mechanical properties, such as strains and stiffnesses of the MTC and CE are robust with regard to camera synchronisation and marker position delay. In the four cases considered above, the estimated MTC stiffness values, from a 3-parameter fit (Eq. 2.1), span between 1560 N m^{-1} , 1630 N m^{-1} , 1620 N m^{-1} , and 1530 N m^{-1} for Fig. 2.10a,b,c and d, respectively.

To systematically check for camera offsets, three different methods of detection were used (Table 2.1). Common for all three methods was the attempt to detect an equal number of steel markers in each of the two cameras. The

first method subtracted the arithmetic mean of all individual tracked muscle belly frame numbers, at which the markers reached their lowest vertical positions, in each camera and subsequently subtracted and rounded the difference to the nearest integer (*MinPos*). In the second method, the TD frames were found in each camera and then subtracted (*ImpIdx*). The third method compared the frame number that included the lowest a_{COM} value in each camera (*MinAcc*), which was chosen due to its narrow and easily detectable minimum. All three methods indicated a camera offset of either 1, 0, or -1. As seen in Table 2.1, there were camera offset indications throughout the experiments, but all indicators proved to be inconsistent. As a consequence thereof, the work-loops were calculated separately and presented as a mean for both cameras.

	max dev	0 dev	1 dev	2 dev	3 dev	N
MinPos	1	20	20	-	-	40
ImpIdx	3	18	16	4	2	40
MinAcc	1	24	20	-	-	40
MinPos ImpIdx *	3	18	17	4	1	40
MinPos MinAcc *	1	26	14	-	-	40
ImpIdx MinAcc *	3	17	20	2	1	40
AllSame *	-	12	-	-	-	

Table 2.1 | Camera recording inconsistencies within each trial that did not fulfil the exclusion criteria. The table lists the three methods of detecting inconsistencies (*MinPos*, *ImpIdx*, *MinAcc*) and the consistency between them (**MinPos|ImpIdx**, **MinPos|MinAcc**, **ImpIdx|MinAcc**). **AllSame** is number of trials where all three methods of detecting (**MinPos**, **ImpIdx**, **MinAcc**) are consistent. All three methods and comparisons of methods, are listed with the maximal found frame deviation (**max dev**) and how the found deviations, e.g. the number of frames, are distributed (**0 dev**, **1 dev**, **2 dev**, or **3 dev**) across all trials (N). For the three methods, the **MinPos**, is the difference between the lowest centre of mass COM position in each of the two cameras. **ImpIdx**, is the frame difference between the touch-down (TD) index value in each of the two cameras. **MinAcc**, is the frame difference between the lowest acceleration of COM a_{COM} value in each of the two cameras. This table is from Christensen *et al.* (2021)[94], reproduced with permission from Springer Nature.

* The numbers given here compares the inconsistencies between thw methods of detection, i.e. how often two methods has the same findings for a trial.

2.3.4 Scaling the MTC and CE findings

Under the assumption that the CE region is an isotropic and homogeneous material, the stiffness of the contractile element k_{CE} was scaled to the stiffness

of a half-sarcomere k_{hs} with

$$k_{hs}(k_{CE}) = \frac{r \cdot A_{hs} \cdot E}{L_{hs}} = \frac{r \cdot A_{hs} \frac{k_{CE} \cdot L_{CE,0}}{A_{CE,max,0}}}{L_{hs}} \quad , \quad (2.5)$$

where $L_{CE,0}$ and the maximum cross-sectional area $A_{CE,max,0}$ are anatomical data from Table 4.1, and E is Young's modulus. The half-sarcomere length (L_{hs}) is set to 1150 nm [95], and the area of an elementary cell (1 myosin and 2 actin filaments) is $A_{hs} = 1540 \text{ nm}^2$ (Fig. 6.9).

Assuming that $A_{CE,max,0}$ takes up 83% ($r = 0.83$) [96] of a macroscopic muscle's ACSA and that the remaining 17% does not carry any significant loads at these lengths [97, 98] the corresponding isometric force per half-sarcomere F_{hs} was calculated as

$$F_{hs}(F) = \frac{F \cdot A_{hs}}{r \cdot A_{CE,max,0}} \quad . \quad (2.6)$$

Of which the parameter $A_{CE,max,0}$ was chosen because the examined fibre area, with $L_{CE,0} = 7.5 \text{ mm}$ (Table 4.1), was located approximately at the muscle belly centre at which $A_{CE,max,0}$ applies rather than $A_{CE,avr,0}$. F is the isometric force generated by the GAS MTC just before TD, which is measured by the force transducer.

By correspondingly applying the above scaling rules for lengths and forces, the work per half-sarcomere (w_{hs} , right y-axis Fig. 4.3c) is estimated as

$$w_{hs}(w_{CE}) = \frac{w_{CE} \cdot L_{hs} \cdot A_{hs}}{r \cdot L_{CE,0} \cdot A_{CE,max,0}} \quad , \quad (2.7)$$

where the work of the contractile element (w_{CE}) was calculated as the area enclosed by a work-loop (see Sect. 2.3.2). The damping coefficient per half-

sarcomere (d_{hs}) was calculated with

$$d_{hs}(d_{CE}) = \frac{d_{CE} \cdot A_{hs} \cdot L_{CE,0}}{A_{CE,max,0} \cdot L_{hs}} \quad , \quad (2.8)$$

and the damping coefficient of the contractile element (d_{CE}) was inferred from Eq. 2.1. Comparing Eq. 2.5 to Eq. 2.8 reminds us that linear stiffnesses and damping coefficients scale the same with the dimensions of the finite volumes of which they represent these mechanical properties.

2.3.5 Model ideas (short version)

In line with the aim of Study 2, the experimental data will be probed by two different muscle models to explain which parameters that are essential to model cross-bridge stiffness.

In *model1* [1] (Fig. 2.11), the half-sarcomere consists of two compartments *in-series*: the cross-bridges and the myofilaments. The force generated by a single cross-bridge is assumed to be a constant, with an associated constant deflection (ΔL_{CB}). The overall half-sarcomere force F_{hs} equals the sum of all cross-bridge forces (F_{CB}), which scales linearly with the number of attached heads (n_{CB}), like the overall stiffness ($k_{CB} = \frac{F_{CB}}{\Delta L_{CB}}$) of the cross-bridge part. Knowing the constant parameters ΔL_{CB} and myofilament compliance C_{fil} , the half-sarcomere stiffness can be determined as

$$k_{hs}(F_{CB}) = \frac{1}{C_{fil} + \frac{\Delta L_{CB}}{F_{CB}}} \quad . \quad (2.9)$$

In a fully fresh muscle with $F_{CB} < F_{CB,max} = 445$ pN (see Sect. 4.1), leaving both parameters in Eq. 2.9 open for a fit to the data in Fig. 4.2, $\Delta L_{CB} = 85.7$ nm

and $C_{fil} = 0.4 \text{ nm pN}^{-1}$ (Table 4.2).

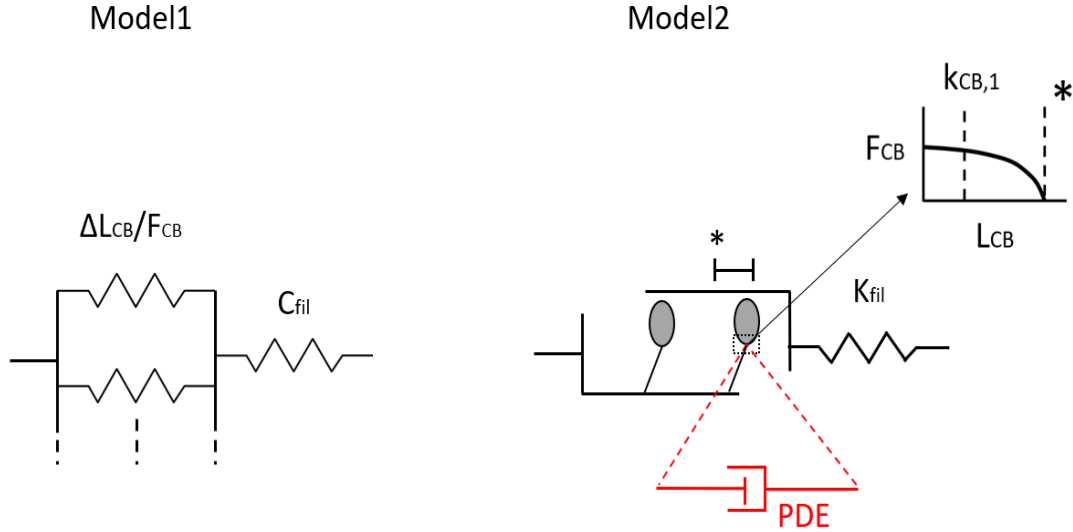


Figure 2.11 | Elements that, according to *model1* and *model2*, contribute to the half-sarcomere stiffness k_{hs} . In the elastic *model1*, the myofilament compliance (C_{fil}) is in series with stiffness k_{CB} the number of attached *in-parallel* myosin heads (cross-bridges, CB). The force generated by a single cross-bridge is assumed to be a constant, with an associated constant deflection ΔL_{CB} . Thus, the stiffness of the ensemble of cross-bridges only ($k_{CB} = \frac{F_{CB}}{\Delta L_{CB}}$) scales linearly with the number of attached myosin heads. In the non-linear, visco-elastic *model2*, the half-sarcomere stiffness k_{hs} is likewise determined by the number of *in-parallel* attached myosin heads, with each head's driving non-linear force-length relation $F_{CB}(L_{CB})$ depicted in the top right inset, and a collective of *in-series* passive stiffnesses denoted myofilament stiffness ($k_{fil} = \frac{1}{C_{fil}}$), see Eq. 2.11. $k_{CB}(F_{CB})$ (Eq. 2.10) is determined under the assumption that $L_{CB} = L_{CB,opt} = 7 \text{ nm}$, i.e., $F_{CB} = F_{CB,max}$. See Fig. 6.8 for $F_{CB}(L_{CB})$ as determined with original model parameters. Note that, to compare *model1* and *model2*, the visco-elastic PDE from *model2* is excluded (accordingly, PDE is marked in red). This figure is from Christensen *et al.* (2021) [94], reproduced with permission from Springer Nature. * The dashed line at the asterisk marks the end of the work-stroke.

model2 [2] is more complex (Fig. 2.11): apart from the myofilaments, the cross-bridge itself is divided into a catalytic domain and a light chain domain that can rotate, actuated by a Coulomb force drive, with respect to the catalytic domain (both represent the S1 part). Combined, light chain, S2 part and the myofilaments form the (serial) elastic part, which is collectively referred to by the stiffness symbol k_{fil} further below. The underlying model idea consists of a repulsing Coulomb force generated within the catalytic domain, which upon myosin head attachment causes a driving force acting between the catalytic and the light chain domains. The driving force then levers the light chain such that the cross-bridge can generate force between the actin and the myosin filaments ([Fig. 2] [2]). According to *model2*, the force $F_{CB}(L_{CB})$ generated by the attached cross-bridges in a half-sarcomere is a non-linear function of the model-internal lever arm coordinate L_{CB} ([Fig. 2] [2]), and the corresponding cross-bridge stiffness k_{CB} is

$$k_{CB}(F_{CB}) = 2 \cdot F_{CB,max} \cdot \sqrt{\frac{\left(\frac{F_{CB}}{F_{CB,max}} - \frac{-c_1}{c_3^2}\right)^3}{c_1}}, \quad (2.10)$$

where $F_{CB,max}$ is the maximum force generated by the cross-bridge ensemble in a half-sarcomere (their current number: n_{CB}). The c_1 is a constant that depends on c_3 and assumes the lever coordinate ($L_{CB,opt}$) is at its optimal lever arm position corresponding to a cross-bridge generating about $F_{CB,1} = 4\text{-}5$ pN ($F_{CB,max} = n_{CB,max} \cdot F_{CB,1}$, with $n_{CB,max} \approx 90$; for more detail regarding Eq. 2.10, see Appendix 6.4). At $L_{CB} = -c_3$ the assumed function $F_{CB}(L_{CB})$ of the cross-bridge-internal force-length relation has a pole.

In line with *model1*, k_{CB} in *model2* acts *in-series* with myofilament (plus S1) stiffness $k_{fil} = \frac{1}{C_{fil}} = 150$ pN nm⁻¹ [53] to make up overall k_{hs} . Further, it was assumed that all cross-bridges in *model2* are always at $L_{CB,opt} = 7$ nm.

With this, just like in *model1*, the isometric force $F_{CB} = u \cdot F_{CB,max}$ and the cross-bridge stiffness $k_{CB} = u \cdot k_{CB,max}$ are assumed to scale linearly with solely the number n_{CB} of attached myosin heads ($u = \frac{n_{CB}}{n_{CB,max}}$). Thus, the overall k_{hs} for *model2*, when additionally using the latter assumption, can then be expressed as

$$k_{hs}(u) = \frac{u \cdot k_{CB,max} \cdot k_{fil}}{u \cdot k_{CB,max} + k_{fil}} \quad , \quad (2.11)$$

leaving only the c_3 value open for fitting (see Table 4.2) in Eq. 2.10 because $k_{CB,max} = k_{CB}(F_{CB} = F_{CB,max})$.

Chapter 3

Study 1: strain in shock-loaded skeletal muscle

3.1 Results

All experiments were conducted within the first hour of *m. gastrocnemius* dissection to prevent permanent muscle tissue damage due to ischaemia (see Sect. 1.2.2). The mean anatomical data of the GAS specimens (N = 9) used in this chapter are in Table 3.1.

Description	Symbol	Data	Unit	Source
Animal mass	m_{animal}	413±16	g	measured
GAS mass	m	2.0±0.3	g	measured
MTC length at 90°	$L_{MTC,90^\circ}$	43±0.3	mm	measured
MTC length in frame	$L_{MTC,0}$	45 [*]	mm	$L_{MTC,90^\circ} - 2$
Belly length	$L_{belly,0}$	33 [†]	mm	$L_{MTC,0} - L_{CE,0}$
Reference length	$L_{CE,0}$	18±0.8	mm	measured
Proximal tendon length	$L_{prox,0}$	2 [*]	mm	literature
Distal tendon length	$L_{dist,0}$	10±0.35	mm	measured
Total tendon length	$L_{tendon,0}$	12 [*]	mm	$L_{prox,0} + L_{dist,0}$
Maximum belly ACSA	$A_{CE,0,max}$	109±4.5	mm ²	measured
Minimum belly ACSA	$A_{CE,0,min}$	73±3.6	mm ²	measured
Tendon ACSA	$A_{tendon,0}$	2.8±0.2	mm ²	measured

Table 3.1 |Anatomical data in Study 1. The anatomical data given as the mean value \pm standard deviation of the nine specimens ($N = 9$), where the anatomical cross-sectional area (ACSA) was calculated by approximating the geometrical form of the area with a half-ellipse. One half-axis was measured as half the width of the muscle projection in the frontal view (Fig. 2.4c) right before TD. The second half-axis was calculated as the width along the frontal visual axis; this number was calculated from the shot of another camera at the same instant, and this camera was positioned to view along an axis rotated by 40° against the frontal view axis (partial side view). This table is from Christensen *et al.* (2017)[92], reproduced with permission from Springer Nature.

^{*}The measured values of MTC length at 90° ankle and knee angles ($L_{MTC,90^\circ}$) and of distal tendon length ($L_{dist,0}$) as well as the very short proximal tendon length ($L_{prox,0}$) are equal (within 1 mm) to those published elsewhere [83].

[†] $L_{belly,0} = 32$ mm measured by others [99].

The experimental conditions correspond to total ischaemia, a condition in which force decline has been described as fatigue [74, 100, 101] (see also

Sect. 1.2.2). Each muscle specimen fatigued with consecutive trials, which can be seen from the trial-specific isometric force F decreasing almost linearly with time after muscle extraction (Fig. 3.1). Isometric force saturation tendencies were seen after 30-45 min at levels between 2% and 13% of maximum (non-fatigued) isometric force F_{max} . By linear extrapolation from 60 min back to the instant of extraction (thick, solid line in Fig. 3.1), the estimated mean maximum value of $F = F_{max} = 30$ N, which can be expected from GAS anatomy (Table 3.1) and literature (see Sect. 3.2.1). On average, maximum values of ΔF are 0.35 ± 0.07 N, and they are practically independent of fatigue (see left y-axis in Fig. 3.3).

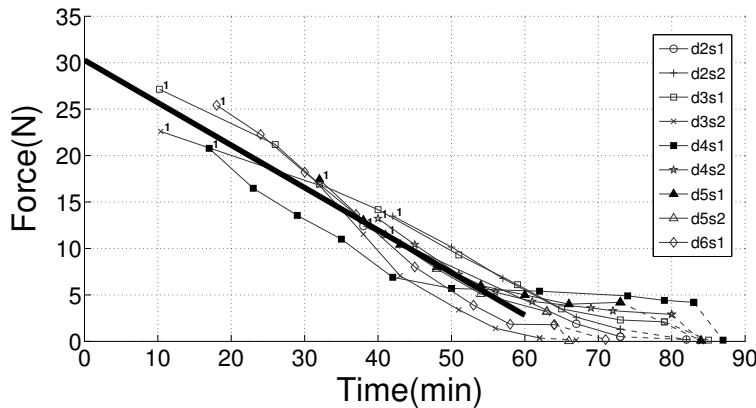


Figure 3.1 | Initial isometric muscle force F at TD versus time after muscle extraction. Only trials with a TD force of at least 95% of its isometric value were included, where the latter was defined by the value to which the force transducer signal converged shortly before or after TD (see Fig. 2.6). Trials were named (see key top right) after consecutive days of experiments ('d#'), the first ('s1') or second ('s2') specimen extracted that day, and the trial number (starting with first as '00'). The thick, solid line is a linear fitting line to all data points below 60 min. The extrapolation to the instant of extraction at 0 min was assumed to represent the maximum isometric force $F = F_{max} = 30$ N. In Figs. 3.2, 3.4, 3.6 and 3.3 the number of trials included is lower due to further exclusion criteria (see Sect. 2.2.4). This figure is from Christensen *et al.* (2017) [92], reproduced with permission from Springer Nature.

The instants at which maximum accelerations occurred were 7.4 ± 1.0 ms and 7.7 ± 0.9 ms for the frame and COM, respectively. While the COM signal lagged the frame signal by 0.3 ms, on average, a t-test showed that this lag was insignificant at $p > 0.05$. The maximum COM acceleration values $a_{COM,max}$ were $165 \pm 23 \text{ m s}^{-2}$ (see right y-axis Fig. 3.3), which were reached, on average, 2.7 ms earlier than maximum strain. However, strain kinematics are much more variable (see standard deviation of 2.5 ms): in some trials, maximum strain was even reached before maximum COM acceleration, particularly in non-fatigued muscle with low strain maxima (Fig. 3.2, top). The impact duration measured as the time spent from TD to frame (or bone) acceleration returning to zero was 10.7 ± 0.9 ms. Zero COM acceleration occurred at 11.3 ± 0.7 ms, and the delay to zero frame acceleration was doubled to 0.6 ms as compared to instants of their maxima, which was significant on a level $p < 0.05$ using a t-test.

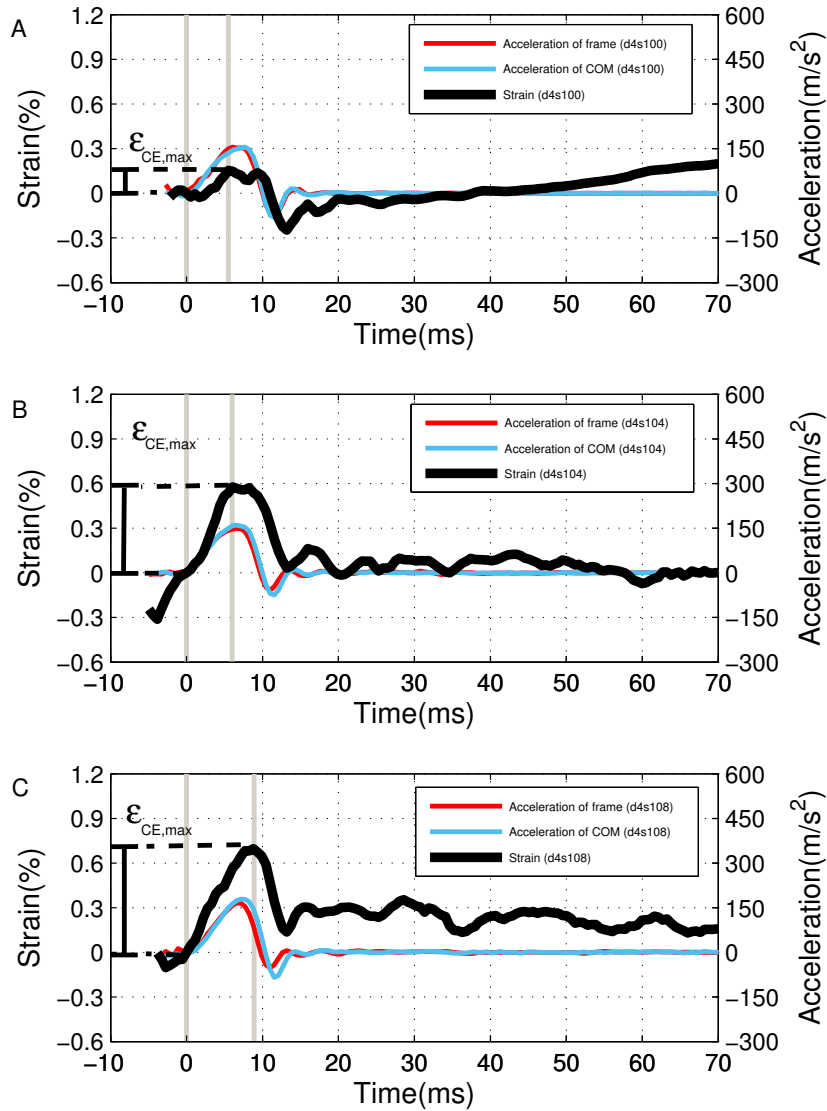


Figure 3.2 |Time courses of CE strain, accelerations of COM and frame. Plots of the local fibre material strain ϵ_{CE} (black, thick, solid line: $\epsilon_{CE} = 0$ at TD), net vertical MTC acceleration a_{COM} (light blue, thin, solid line: arithmetic mean of all steel markers' values approximating the centre of mass, i.e., COM kinematics), and vertical acceleration of the suspending frame a_{frame} (dark red, thin, solid line) for three trials (from top to down) of the same muscle specimen: 'd4s100', 'd4s104', and 'd4s108' (naming: Fig. 3.1). The vertical, grey lines indicate time instants of TD ($t = 0$ s) and the maximum dynamic strain amplitude $\epsilon_{CE,max}$ during shock response ($t > 0$ s). This figure is from Christensen *et al.* (2017) [92], reproduced with permission from Springer Nature.

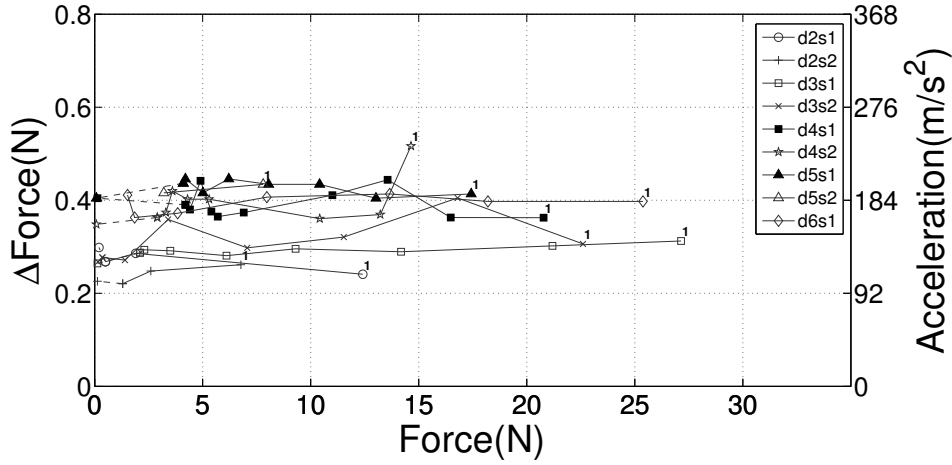


Figure 3.3 |Muscle force peak (dynamic force change ΔF) during shock-wave-induced (‘dynamic’) fibre material strain after TD versus isometric force F at TD. The dynamic force change ΔF was calculated as the corresponding vertical acceleration a_{COM} of the MTC’s COM (right y-axis) plus gravitational acceleration multiplied by muscle mass m (see sect. 2.2.3). The COM position was calculated as the arithmetic mean of all steel marker positions. The mean ΔF is $0.35 \text{ N} \pm 0.03$. This figure is from Christensen *et al.* (2017) [92], reproduced with permission from Springer Nature.

Across all trials, the muscle fibre strain increased from $\approx 0.2\%$ to 1% in fully fresh and active muscle to non-stimulated fibre material, respectively (Fig. 3.4). To examine fibre strain in muscle fibre, the strain is divided into two contributions: ‘initial strain’ due to the initial, isometric force and additional ‘dynamic strain’, due to the impact response, as plotted in Fig. 3.2. For the initial strain, two limit cases of locating elasticity as a potential cause are conceivable: strain is either (i) solely located in the myosin heads or (ii) distributed across all sarcomere structures that act in series, that is, heads and actin plus myosin filament backbones. By further assuming in the case (i) that decreasing initial force was solely due to the reduced number of attached cross-bridges, the initial strain of the fibre material would always be

the same, regardless of the force – that is, any single cross-bridge generates its maximum force (about 0.4% [34, 1, 102, 103, 104], see bottom, horizontal, blue, dashed line in Fig. 3.4). In any other case, the most simple model relating initial fibre force to initial strain would be a linear stiffness (see bottom, sloped, red, solid line in Fig. 3.4 with zero strain at zero force and -0.4% at maximum isometric force), which is case (ii). For one trial, the initial and dynamic strain contributions are visualised in Fig. 3.4 by vertical arrows – a blue, dashed arrow (i) and a red, solid arrow (ii) for the two initial strain cases as well as a black, solid arrow on top of them for the measured dynamic strain.

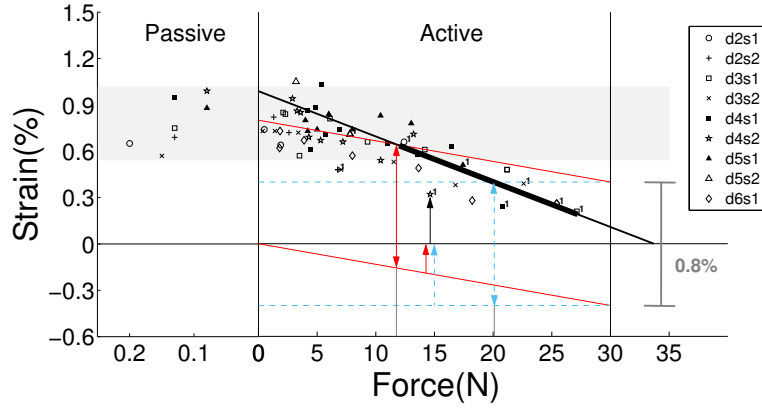


Figure 3.4 | Maximum shock-wave-induced (‘dynamic’) fibre material strain $\epsilon_{CE,max}$ after TD versus isometric force F at TD. Data for fully active muscles on the right side of $F = 0$ and non-stimulated (‘passive’) muscles on the left. The grey-shaded region indicates a range of values from trials with passive muscle. Horizontal, blue, dashed as well as sloped, red, solid baselines at $\epsilon_{CE,max} < 0$ symbolise initial strain hypothesised for cases (i) and (ii), respectively (see Sect. 3.1). Dynamic strain values at which cross-bridges may be forcibly detached in cases (i) and (ii) are symbolised by corresponding lines at $\epsilon_{CE,max} > 0$, where both are placed at $\Delta\epsilon_{CE,max} = 0.8\%$ distances from their respective baselines. Red, solid and blue, dashed arrows from $\epsilon_{CE,max} < 0$ to $\epsilon_{CE,max} = 0$ at $F \approx 15$ N indicate initial strain values for cases (i) and (ii), respectively. The black arrow from $\epsilon_{CE,max} = 0$ to the first trial of specimen ‘d4s2’ is one example of measured dynamic strain. The predicted force limits for forcible cross-bridge detachment are 20.1 N (blue, dashed double arrow) and 11.8 N (red, solid double arrow) for cases (i) and (ii), respectively. The black, thick, solid line represents the linear fitting line for $\epsilon_{CE,max}$ using all data points at $F > 12$ N – the thin extensions extrapolate to $F = 0$ and $F = F_{max} = 30$ N. This figure is from Christensen *et al.* (2017) [92], reproduced with permission from Springer Nature.

To examine whether the calculated CE and MTC stiffness values may depend monotonically on isometric force F the data was fitted with simplest approach, that is, a linear function. The corresponding straight-line fits through all data points above 12 N are plotted in Fig. 3.5. This force boundary value at 12 N was extracted by separating the calculated $k_{MTC}(F)$ and $k_{CE}(F)$ data points into two ranges of approximately constant values

(low forces) and assumed linear change with force F (high forces: straight lines), and searching for the boundary value between them with the best continuity of the inferred $k_{TAC}(F)$ curve (see black, solid line in Fig. 3.6).

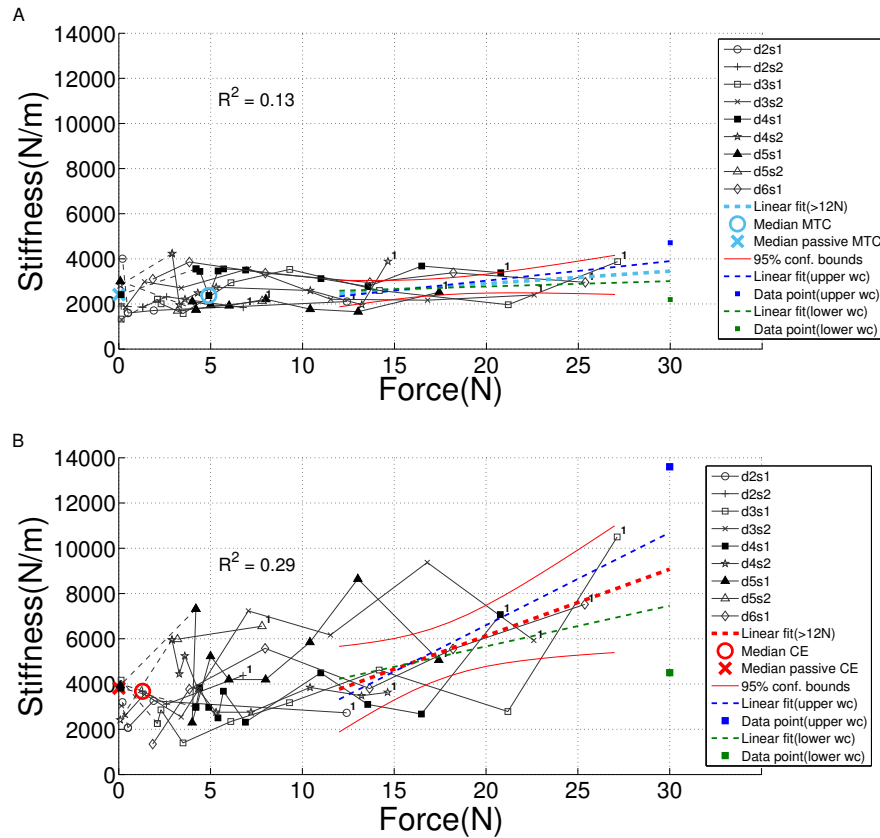


Figure 3.5 | Measured stiffness values of MTC (top: k_{MTC}) and CE (bottom: k_{CE}) versus isometric force F at TD. For each single trial, these values were determined by fitting the linear relation Eq. (2.1). Through each of the two data clouds, a linear fit $k = a \cdot F + b$ to all data points was calculated for $F > 12$ N. Additionally, the following are also plotted: (i) circles represent the median value for trials with active muscles in the region $F < 12$ N, and (ii) a cross represent the median value for all trials with passive muscles. To illustrate the uncertainty of the linear approximations (light blue, thick, dashed line in A and red, thick, dashed line in B), the linear fits was re-calculated using two additional worst case data points that were hypothetically placed at the maximum observed force (blue and green squares). The corresponding linear fits, each including the respective worst cast data point, are plotted as dashed blue and green lines, respectively, in A and B. Additionally, the 95% confidence intervals for the undisturbed linear fits in A and B are plotted with red, thin, solid lines. Note that, although MTC stiffness does only weakly depend on force, the slope of the linear fit remains positive even in the worst case of the hypothetically low stiffness value at maximum force. This figure is from Christensen *et al.* (2017) [92], reproduced with permission from Springer Nature.

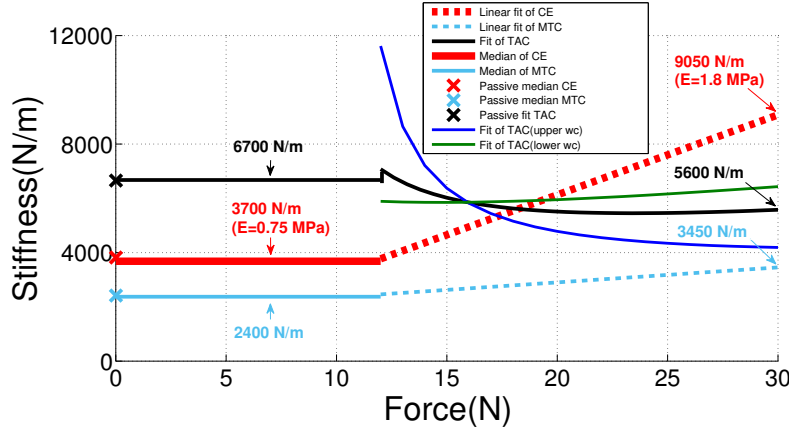


Figure 3.6 |Linear interpolations $k = a \cdot F + b$ versus isometric force F at TD in the region $F > 12$ N for stiffness values of CE (k_{CE}), MTC (k_{MTC}), and TAC (k_{TAC}). k_{CE} and k_{MTC} were measured (Fig. 3.5), whereas k_{TAC} was inferred from Eq. (3.2) and Eq. (2.2), respectively. Horizontal lines represent the respective median values for trials with active muscles in the region $F < 12$ N. Crosses represent the respective median values for all trials with passive muscles (for more details see sect. 3.2.1 and Sect. 2.2.3). The dark blue and green lines illustrate the uncertainty of TAC stiffness inferred on the basis of the linear fit $k = a \cdot F + b$ to MTC and CE stiffnesses (Fig. 3.5). The combined effects of MTC and CE stiffness dependencies on force are assumed to both follow the lower slopes in their worst case examination in Fig. 3.5 and result in the dark green line for the TAC stiffness dependency. Vice versa, combining both MTC and CE worst cases with upper slopes gives the dark blue line for the TAC stiffness dependency. This figure is from Christensen *et al.* (2017) [92], reproduced with permission from Springer Nature.

3.2 Discussion

3.2.1 The isometric force in isolated muscle

The maximum isometric muscle tension σ_{max} is between $2.25 \cdot 10^5 \text{ Nm}^{-2}$ [105] and $3 \cdot 10^5 \text{ Nm}^{-2}$ [50]. If the PCSA and both $P_{CE,0}$, and the pennation angle α are known [106, 107], then the maximum isometric muscle force F_{max} can be estimated. In case (a) [106], $P_{CE,0}$ and α were measured for the *gastrocnemius*

medialis and *lateralis* muscles separately. The *lateralis* muscle accounted for 56% of the GAS PCSA ($P_{CE,0} = 111 \text{ mm}^2$) and $\alpha = 14^\circ$ was found in both muscles. In case (b) [107], measurements were made for only *m. gastrocnemius medialis* (54 mm^2 , $\alpha = 21^\circ$). Assuming a 44% contribution of this muscle, which is in line with Eng *et al.* (2008) [106], the overall GAS PCSA in the work of Kadhiresan *et al.* [107] would then have been $P_{CE,0} = 123 \text{ mm}^2$. Due to the same boundary condition defining $L_{MTC,90^\circ}$ in case (i) [106], it was further assumed that $\alpha = 14^\circ$. Thus, the mean PCSA ($P_{CE,0} = 112 \text{ mm}^2$) can be calculated as

$$P_{CE,0} = \frac{A_{CE,0,max}}{\cos \alpha} \quad (3.1)$$

Based on the σ_{max} range given above, maximum isometric force can be calculated as $F_{max} = \sigma_{max} \cdot A_{CE,0} = \sigma_{max} \cdot P_{CE,0} \cdot \cos \alpha$, which would yield values between 24.2 N and 32.3 N in case (i) and between 25.8 N and 34.5 N in case (ii). Compared to these estimations, a $F_{max} = 30 \text{ N}$ was found by extrapolation (Fig. 3.1).

3.2.2 Fibre material strain in response to TD

Shock-waves induced dynamic strains of ca. 0.2% in the least fatigued case (Fig. 3.4). The net strain of all fibre-internal serial elasticities in the actin and myosin filaments and the cross-bridges at maximum isometric force is ca. 0.4% [34, 108, 1] in the non-fatigued case. Forces to forcibly detach one myosin head from actin have been measured to scatter around 9 pN [35], while estimations of the maximum isometric force of a cross-bridge range from 2 pN [34] to more modern, higher values [53], and up to more than 10 pN [108]. Moderate values of ca. 4 pN come from energetic estimations [36, 37]. Mechanical, structural, and energetic approaches seem to converge at about

5 pN [38]. Additionally, force saturation in eccentric contractions, as another possible measure for a limit of forcibly detaching myosin heads, which indicates muscle ‘giving’, has been quantified to be 1.4-2.0 times the isometric force [39, 40, 41, 42].

Altogether, following three assumptions is used for the line of reasoning in the remainder of this paragraph: (a) other possible sources of forces that act in parallel to a cross-bridge and may resist stretching (e.g., titin [109, 110]) are neglected, (b) also an initial strain of 0.4% in the serial elasticities is assumed at maximum isometric force $F = F_{max}$, and (c) roughly double this force value is needed to forcibly detach a cross-bridge, corresponding to 0.8% limit strain. If it is further assumed that in model case (i) fibre-internal stiffness k_{CE} is located solely in the myosin heads (horizontal, blue, dashed lines in Fig. 3.4), the initial plus shock-wave-induced, dynamic strain according to the experimental data would allow cross-bridges to stay bound down to 20.1 N (67% of F_{max} : vertical, blue, dashed double arrow in Fig. 3.4). In the upper limit model case (ii) of k_{CE} distributed across heads, actin, and myosin (vertical, red, solid lines in Fig. 3.4), cross-bridges are predicted to stay bound down to 11.8 N (40% of F_{max} : vertical, red, solid double arrow in Fig. 3.4). This is practically the very same force boundary value $F = 12$ N (40% of F_{max}) that was found in the stiffness analysis (Fig. 3.6), where the changes of CE and MTC stiffness characteristics with force F saturate at constant levels of the passive muscle. For a discussion of the local joint force F see Sect. 3.2.4.1.

To support the argument given here of measuring strain as an indicator of forcible cross-bridge detachment, a short review the basic idea behind force generation by a tilting myosin head within a cross-bridge will follow. Mechanically, during the force-generating process (i.e. the work stroke) the

myosin head must be strongly bound to actin. The term ‘strongly bound’ implies limited adherence forces at the attachment site, and an analogue of a myosin head would be a sucker adhering to an actin active site, where the adherence force is limited by the material properties of both adherents. As there are head-internal and filament-internal contributions to elasticity, this elementary work stroke process and the functional existence of fibre-internal stiffness are, mechanically, inseparably connected. Thus, more or less by definition of the term ‘strongly bound’, any other potential binding state, which may be suggested by observation and postulated by models of muscular contraction, is ‘weakly bound’ in a mechanical sense. Weakly bound states can thus not contribute to fibre-internal stiffness as an insignificant force in the location of attachment would resist strain. However, while energy dissipation will always be induced by forcible detachment of strongly bound states, such dissipation may also occur for weakly bound states. Such energy loss has also been termed ‘protein friction’ [111, 112, 113, 114, 115].

After an event of forcible detachment, it is expected that a previously strongly bound cross-bridge undergoes ‘repriming’ [68, 116], which may be the re-attachment at an active site on actin that would be located at one, two, or more active sites further from the site of detachment. Such repriming occurs within about 5-8 ms in response to shortening [68]. In response to 5 nm lengthening steps per cross-bridge [116], which corresponds to ca. 0.5% dynamic strain, many cross-bridges seem to remain attached as can be seen from the initial force response, which is a peak that is due to elastic distortion. Repriming after lengthening seems to be slower than during shortening. It will thus not occur during shock-wave-induced impacts lasting about 10 ms. If cross-bridges are forcibly detached during shock-waves, then the following is expected: (a) energy dissipation by protein friction, (b) rapid relaxation of

all non-detached cross-bridges [116, 34] on the time scale of a few milliseconds after a force peak ΔF , (c) repriming of cross-bridges on the time scale of ca. 50 ms [116]), and (d) re-attachment dynamics of the assembly of cross-bridges on an even longer time scale with reduced forces in response to the intermittent phenomena of force increase ΔF and relaxation decrease.

3.2.2.1 Young's moduli – a comparison to literature

Young's modulus $E_i = k_i \cdot \frac{L_{i,0}}{A_{i,0}}$ is defined as a local material property that can be found from known macroscopic properties of a finite mass portion i , including stiffness k_i , reference length $L_{i,0}$, and cross-sectional area $A_{i,0}$. With the chosen reference length $L_{CE,0} = 0.018$ m (Table 3.1) in the centre of the muscle belly, $A_{CE,0} = 1.09 \cdot 10^{-4}$ m², the maximum estimate of the anatomical cross-sectional area (ACSA) within $L_{CE,0}$ (Table 3.1) and $k_{CE} \approx 9050$ N m⁻¹, the lower limit of CE's Young's modulus was calculated to be $E_{CE} \approx 1.5$ MPa in fully active, fresh muscle fibres. Due to low pennation angles $\alpha \approx 20^\circ$ at optimal fibre length [106, 107, 99], the ACSA values and physiological cross-sectional area (PCSA) values found in literature [106, 107] are practically identical. For fixed $A_{i,0}$ and $L_{i,0}$, Young's modulus scales linearly with k_i . Thus, in strongly fatigued and passive muscle fibres with $k_{CE} \approx 3700$ N m⁻¹, Young's modulus ≈ 0.6 MPa as a minimum, which is ca. 40% of the stiffness and modulus values for fresh, fully active fibres. Using $A_{CE,0} = 0.73 \cdot 10^{-4}$ m² estimated at its upper (proximal) end, the minimum ACSA value within $L_{CE,0}$, the estimated upper limit of Young's modulus is $E_{CE} \approx 2.3$ MPa for fresh and $E_{CE} \approx 0.9$ MPa for fatigued/passive muscle fibres. Assuming volume constancy, homogeneity, and uniformity for fibres and the belly's [117, 118, 119, 120, 121], Young's modulus equals the shear modulus. With this, these results match others' data [122] well; this is demonstrated by the local

shear values that were found at the Z-disc and M-line locations: 2.6 MPa and 1.3 MPa, respectively, in a fully active fibre as well as 1.7 MPa and 1.2 MPa, respectively, in a passive fibre.

TAC stiffness k_{TAC} according to Eq. (2.2) is calculated (inferred) from

$$k_{MTC} = (k_{CE} \cdot k_{TAC}) / (k_{CE} + k_{TAC}) \quad . \quad (3.2)$$

k_{TAC} contains all compliances in series to the fibre material, and is equivalent to what is often referred to as ‘serial elastic element’ (SEE) or ‘serial elastic component’ (SEC) in muscle modelling. The basic notion is described in three papers [123, 124, 125]. First, to check whether TAC stiffness was dominated by tendon properties, the tendon stiffness

$$k_{tendon} = E_{tendon} \cdot \frac{A_{tendon,0}}{L_{tendon,0}} \quad (3.3)$$

was calculated from anatomical data $L_{tendon,0} = 0.012$ m, $A_{tendon,0} = 2.8 \cdot 10^{-6}$ m², and a well-established literature value for Young’s modulus of mammalian tendon material $E_{tendon} = 1.5$ GPa [126, 127, 128, 129] as $k_{tendon} = 350$ kN m⁻¹. This k_{tendon} value would be about 50 times higher than the upper limit of inferred TAC stiffness values $k_{TAC} = 6700$ N m⁻¹. Conversely, an upper limit estimate of TAC’s Young’s modulus

$$E_{TAC} = k_{TAC} \cdot \frac{L_{TAC,0}}{A_{TAC,0}} \quad (3.4)$$

can be calculated from assuming (a) the highest stiffness value $k_{TAC} = 6700$ N m⁻¹ inferred from this analysis, (b) the smallest cross-sectional area value $A_{TAC,0} = A_{tendon,0} = 2.8 \cdot 10^{-6}$ m² measured for rat GAS tendon, and (c) the length $L_{TAC,0} = L_{MTC,0} - L_{CE,0} = 0.027$ m that bridges the distance between the

fibre material (analysed within $L_{CE,0}$) and the frame. The corresponding theoretical, upper limit $E_{TAC} = 64$ MPa is 23 times lower than mammalian tendons' Young's modulus. Alternatively, the lower limit $E_{TAC} = 2.1$ MPa can be calculated from using (a) the lowest TAC stiffness value $k_{TAC} = 5600$ N m⁻¹ occurring in this analysis and (b) the minimum fibre ACSA value $A_{TAC,0} = A_{CE,0} = 0.73 \cdot 10^{-4}$ m² at the boundary between fibre material (CE) and TAC.

As k_{CE} results from the serial arrangement of all local elasticities within the cross-sectional areas along the finite length $L_{CE,0}$, the most likely value of inferred E_{CE} should be approximately the arithmetic mean value of the upper and lower limits at each force, that is, $E_{CE} = 1.9$ MPa for fresh and $E_{CE} = 0.75$ MPa for fatigued/passive muscle. The local net material property E_{TAC} in a belly's aponeurosis region may well increase continuously – when approaching the aponeurosis-tendon junction – from $E_{TAC} = E_{CE} = 0.75 \dots 1.9$ MPa at the fibre-aponeurosis boundary to $E_{TAC} = E_{tendon} = 1.5$ GPa at the aponeurosis-tendon junction. Besides the fibre activity, this continuous change will depend on the geometrical arrangement of the aponeurosis and the fibres as well as on the shifting fibre-to-aponeurosis ratios of material contributions within the belly and on the belly surface. Average values of TAC's Young's modulus in the range $E_{TAC} = 2.1$ -64 MPa supports this idea.

3.2.3 Regional stiffnesses in whole muscle

The measured strain increases with fatigue down to ca. $F=10$ N (Fig. 3.4), however, the measured dynamic force ΔF is practically independent of fatigue (Fig. 3.3). If the decrease in isometric force F , seen during fatigue, was due to a decrease in force per cross-bridge with the number of cross-bridges remaining the same, then the CE stiffness should remain constant with fatigue. This is because the stiffness of a single cross-bridge is practically

constant down to ca. 10% F_{max} in initially isometric conditions [34, 108] and down to ca. 50% F_{max} in isotonic contractions [53]. Alternatively, if the force per cross-bridge remained constant with fatigue, but the number of cross-bridges decreased, the CE stiffness should decrease along with fatigue. According to Fig. 3.6, CE stiffness k_{CE} decreases from 9050 Nm^{-1} in fresh muscle to 3700 Nm^{-1} at $F = 12 \text{ N}$. This is a strong indication that the CE stiffness decrease is due to a decreasing number of cross-bridges at $F > 12 \text{ N}$.

Except for the cases where either (i) the slopes of $k_{MTC}(F)$ and $k_{CE}(F)$ are zero or (ii) both stiffness values have their x-intersect at zero force, the $k_{TAC}(F)$ curve in Fig. 3.6 will be a non-linear function. The inferred curve represents an almost constant value around $k_{TAC}(F) \approx 5600 \text{ N m}^{-1}$ down to ca. $F \approx 18 \text{ N}$, where the $k_{CE}(F)$ curve starts to undergo the $k_{TAC}(F)$ curve. Non-linear deviation of inferred $k_{TAC}(F)$ from near-constancy increases with a further decrease in force down to the boundary $F = 12 \text{ N}$. However, for Fig. 3.6 three points should be noted: (i) $k_{TAC}(F)$ curvature may be a technical artefact of the fact that $k_{CE}(F)$ and $k_{MTC}(F)$ themselves do not exactly trend linearly with physiological reality; (ii) the independent inferences from below and above $F = 12 \text{ N}$ are almost the same at the boundary itself, namely, $k_{TAC}(F) \approx 6700 \text{ N m}^{-1}$; (iii) the uncertainty of the values $k_{TAC}(F) = 5600\text{-}6700 \text{ N m}^{-1}$ is the same as in other experiments on solely the *m. gastrocnemius medialis* head [41], and the predicted absolute values are slightly lower than found in two other analyses based on Hill-type models [83, 41]. Here, k_{TAC} is equivalent to $k_{SEC} = 9000 \pm 1400 \text{ N m}^{-1}$ (pers. comm. to T. Siebert) [41] and $k_{SEC} = 8000 \text{ N m}^{-1}$ [83] there.

3.2.4 Determining the MTC eigenfrequency

The maximum dynamic strain in response to frame impact was reached at 10.4 ± 2.5 ms after TD, which was on average 2.7 ms delayed to the instant of maximum a_{COM} and 0.9 ms before the a_{COM} returned to zero (Fig. 3.2). The maximum dynamic strain (examples in Fig. 3.2) increased with muscle fatigue (Fig. 3.4), that is, with initial force F decreasing down to ca. a third of F_{max} ($F = 10$ N) and saturation occurring at the level of passive muscle for lower forces. The muscle including its tendon parts was stiff enough for its COM to closely follow the frame kinematics with a delay that slightly increased with time (see Sect. 2.2.2).

The circular eigenfrequency of a MTC exposed to a sudden stretch or a change in force (as in the impact situation) can be predicted as

$$\omega = \sqrt{\frac{k_{MTC}}{m}} \quad (3.5)$$

directly from muscle mass $m \approx 2$ g and MTC stiffness k_{MTC} (Fig. 3.6). Accordingly, the eigenfrequency values $f = \frac{\omega}{2\pi}$ are 209 Hz ($k_{MTC} \approx 3450$ N m⁻¹) and 174 Hz ($k_{MTC} \approx 2400$ N m⁻¹) for fully active and passive muscle, respectively. These eigenfrequency values explain why MTC dynamics is strongly bound to frame kinematics (COM acceleration delayed by 0.6 ms within impact duration).

Equating the frame and leg bone kinematics, the impact duration of ca. 10-15 ms is practically the same in the hindlimbs of running rats [130], small mammals [87] and humans [19]. Peak values of COM acceleration are also similar for a running rat's GAS ($a_{COM,max} = 165$ m s⁻² see Sect. 2.2.2) and running human's leg muscles [19] ($a_{shank,max} \approx 270$ m s⁻², $a_{thigh,max} \approx 160$ m s⁻²). Yet, the phase relations of the leg's wobbling [131, 30] masses in response

to the impact clearly differ. In humans, maximum vertical accelerations of the segmental muscle masses occur ca. 5 ms (shank) and 20 ms (thigh), after maximum leg bone acceleration [19, 21]. Furthermore, one can expect that the MTC mass

$$m = \alpha \cdot \rho \cdot L^3 \quad (3.6)$$

scales with a characteristic length L , with the proportionality factor α , and the mass density ρ . Accordingly, muscle stiffness

$$k_{MTC} = E \cdot \frac{A}{L} = \beta \cdot E \cdot L \quad (3.7)$$

scales linearly with L due to the cross-sectional area scaling as

$$A = \beta \cdot L^2, \quad (3.8)$$

with β being a second proportionality factor and E Young's modulus. With this, the circular eigenfrequency (Eq. (3.5)) scales as

$$\omega = L^{-1} \cdot \sqrt{\frac{E}{\rho} \cdot \frac{\beta}{\alpha}} = m^{-\frac{1}{3}} \cdot \sqrt{E \cdot \beta \cdot (\alpha \cdot \rho)^{-\frac{1}{3}}} \quad (3.9)$$

with length or mass [44], respectively, and using Eq. (3.9) and assuming that MTC mass roughly scales with body mass, a characteristic value of muscular wobbling mass eigenfrequency in humans of $f_{human} = (0.4 \text{ kg} / 70 \text{ kg})^{\frac{1}{3}} \cdot f_{rat} \approx \frac{1}{5.6} \cdot 200 \text{ Hz} \approx 35 \text{ Hz}$ can be predicted. Experimentally, the range 25-40 Hz has been found for human shank and thigh muscles [19][figures 3,4,5,6].

3.2.4.1 A reflection on muscle-internal mechanics during impact

In Sect. 2.2.3, it is explained how Newton’s second law was used to calculate – from the kinematics of the centre of the distributed muscle masses (COM) estimated by marker tracking – the dynamic force change ΔF between muscle ends (origin and insertion) that must have acted to accelerate the COM.

If the muscle masses are suspended to a rigid construction (i.e., the frame), one can calculate a finite distance between the COM and the suspension positions that approximates an anatomical length, namely, the muscle-tendon complex (MTC) length. This mechanical analysis of a real muscle implies at least two further prerequisites: (i) it is desirable to formulate a mechanical model of the MTC to potentially subdivide it into further sub-elements, and (ii) the MTC is suspended to a single rigid construction at both ends. Both prerequisites are implied in the calculation of the MTC length, and (ii) means that it does not matter whether MTC length changes are calculated with respect to the upper or lower suspension point.

The initial idea was that the minimum mechanical model description starts with just one net suspending structure for the COM: a spring acting between COM and one suspension point; note that any length change calculated this way represents the length change of all MTC material. Consistent with this, the calculated dynamic force change ΔF , which is proportional to the COM acceleration, is interpreted as the net force change that acts on the MTC spring while it changes its length by ΔL_{MTC} . Likewise, a net MTC stiffness can be calculated, because (iii) few percent of the MTC masses are located in the tendons, which justifies estimating COM acceleration from kinematic information of fibre material solely. The latter can then be used to make a first MTC length subdivision within the model, namely, into the length of mass distribution itself (termed CE) and the remaining material in

series. With this, the COM of the masses in the CE, accelerated in space as calculated above from ΔF , an additional length change ΔL_{CE} of this CE part superposed to the COM movement can be estimated. This CE length change between the upper and lower ends of the CE region subtracted from all MTC length change is the length change ΔL_{TAC} of all MTC parts in series to the CE region.

Using these arguments, model idea of two deforming (length changing) structures in series that suspend the muscle mass to the skeleton or frame, respectively, can now explain in more detail: while the CE can locally change length in any instant due to finite fibre stiffness, which can easily induce, e.g., double fibre stress (and thus mean force F in a cross-sectional area) by doubling strain as compared to initial, isometric strain, the dynamic force change ΔF between both ends of the MTC (and thus CE) provides its acceleration in space. Note that the only measured reliable, static (isometric) force values are before touch-down. ΔF should also be reflected by the sum of both length changes in the upper and lower anatomical structures in series to CE, that is, the upper and lower TAC parts, respectively.

In a nutshell, F and ΔF are, for the time being, two independent mechanical variables that are probably locally and continuously distributed during wave propagation. The variable F represents the concept of ‘joint force’ that causes linear momentum transmission between two adjacent mass distributions (compare, e.g., the work of Lipfert *et al.* (2014) [132] [Appendix 2]) that can be calculated according to Newton’s third law (action=reaction) in any conceived area of cutting through the muscle. The variable ΔF represents the difference in external forces that accelerates one selected mass distribution localised between its spatial boundaries (‘joints’).

In a real muscle, the stress or force, respectively, and their gradients are

expected to vary temporally and spatially during wave propagation. The local force F is the integral of stress over a finite cross-sectional area, and the dynamic force change ΔF is an integral of a force gradient distribution over a finite distance along the gradient. Adding the idea of elastic cross-bridges, changes in strain ϵ and force F are proportionally connected, which applies to both temporal and spatial variations – that is, rates and gradients, respectively – provided there is no forcible detachment. For example, a local gradient in strain generates a local force gradient and thus finite force change ΔF for finite distances along the gradients. With the experimental setup used here in this chapter (1 mm extension tube, Sect. 2.1.2.1), it was only possible to spatially resolve the net (mean) strain in the whole fibre material region of ca. 18 mm using this present pioneering methodological approach, the strain signals (plotted in Figs. 3.2 and 3.4) represent the mean strain values along this CE region. With higher spatial resolution, local strain and thus stress or force F values, respectively, are probably distributed around their mean values.

Chapter 4

Study 2: dissipative responses and cross-bridge mechanics

4.1 Results

All experiments were conducted within the first hour of *m. gastrocnemius* dissection to prevent permanent muscle tissue damage due to ischaemia (see Sect. 1.2.2). The mean anatomical data of the GAS specimens ($N = 5$) used in this chapter are in Table 4.1.

Description	Symbol	Data	Unit	Source
Animal mass		406±6.3	g	measured
GAS mass		1.9±0.2	g	measured
GAS length at 90°	$L_{GAS,90^\circ}$	41±1.2	mm	measured
GAS length in frame	$L_{GAS,0}$	43	mm	$L_{GAS,90^\circ} + 2^\dagger$
Belly length		31	mm	$L_{GAS,0} - L_{tendon,0}$
Reference length	$L_{CE,0}$	7.5± 1.7	mm	measured
Proximal tendon length	$L_{prox,0}$	2 [†]	mm	literature
Distal tendon length	$L_{dist,0}$	10±0.5	mm	measured
Total tendon length	$L_{tendon,0}$	12	mm	$L_{prox,0} + L_{dist,0}$
Maximum belly ACSA	$A_{CE,max,0}$	96±4.9	mm ²	measured
Minimum belly ACSA	$A_{CE,min,0}^\ddagger$	81±16.2 [*]	mm ²	measured
average belly ACSA	$A_{CE,avr,0}$	86	mm ²	$\frac{A_{CE,0,max} + A_{CE,0,min}}{2}$
Tendon ACSA	$A_{tendon,0}$	1.9±0.66	mm ²	measured

Table 4.1 | Anatomical data in Study 2. The anatomical data given as the mean value \pm standard deviation of the five specimens ($N = 5$), where the calculated anatomical cross-sectional area (ACSA) was calculated by assuming that the belly had the geometrical shape of a half-ellipse. This table is from Christensen *et al.* (2021)[94], reproduced with permission from Springer Nature.

[†] The 2 mm added to measured $L_{GAS,90^\circ} \approx L_{opt}$ were inferred from literature [83, 133].

[‡] $A_{CE,min,0}$ was measured ≈ 8 mm distal, along the muscle belly, to where $A_{CE,0,max}$ was measured, both in passive muscle state.

^{*} The relatively large SD in $A_{CE,0,min}$ is due to one outlier geometry.

In Study 2, the average time between each trial was 254 seconds, with the first measurements conducted $t \approx 10$ minutes after dissection ($t=0$). Due to the *ex-vivo* experimental setup, the GAS' measured isometric force declined trial by trial (Fig. 4.1).

Figure 4.1 includes a linear regression of all isometric force data points, which shows a linear trend (<40 minutes), and this trend slope (solid line: $2.9 \cdot 10^{-4} F_{max} \text{ s}^{-1}$) is almost identical to experimental data in Study 1 (dashed line: $2.6 \cdot 10^{-4} F_{max} \text{ s}^{-1}$). A difference between the experiments conducted in Study 1 and the experiments conducted in Study 2 is the average time between each stimulation: here, GAS was stimulated once per 254 seconds, as compared to every 428 seconds in the Study 1 experiments. By linear extrapolation of the fatigue trend in the present data back to $t=0$, an estimated $F_{max} = 23 \text{ N}$ was 7 N lower than the maximum isometric GAS force $F_{max} = 30 \text{ N}$ in Study 1 (Fig. 3.1). In the passive trials, i.e. the non-stimulated muscles, the median of the passive muscle forces measured by the force transducer was 0.25 N.

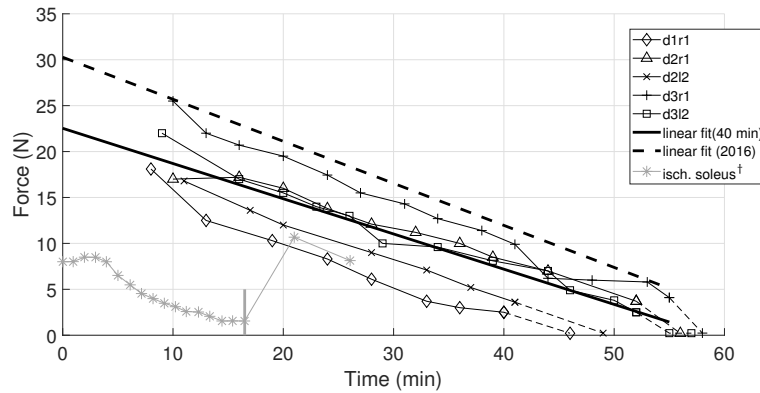


Figure 4.1 | Decline of isometric muscle force (F) at TD versus time after muscle extraction. Only trials with TD force of at least 95% of its isometric value (converged force before or after TD) were included. The solid line is a linear fit to all data points below 40 min, as data shows a lineartrend. For comparison, the dashed, thick line is the linear fit (<60 min) from Fig. 3.1. Both linear fits are extrapolated back to $t = 0$ when the muscles were dissection from the animal. The dashed, thin lines between the last measurement in a trial and its adjacent trial measurement indicates the transition from the active to the passive experiment.

† The measured isometric force in cat *m. soleus* in response to induced ischaemia from Mortimer *et al.* (1970) [74]. In the shown trial, they stimulated the cat muscle with single twitches (*) under ischaemic conditions, whereafter blood flow was returned (grey, vertical line at 16.5 minute mark) to recover muscle force (* > 20 minutes). In a similar work, the isometric force in rabbit *m. anterior tibialis* recovered 87% of the measured maximal isometric force after 1 hour of ischaemia [75]. This figure is from Christensen *et al.* (2021) [94], reproduced with permission from Springer Nature.

The calculated peak value of the dynamic force change between proximal and distal MTC ends in response to the impact had an almost constant mean $\Delta F = 0.2 \text{ N} \pm 0.03$ in all trials. This ΔF was expected due to a falling height of only 1 cm (in Study 2), where the the mean ΔF peak was $0.35 \text{ N} \pm 0.03$ for a 4cm fall height in the Study 1 experiments. Likewise is the present elongations in the fibre material lower (strain at $F = 0.23 \text{ N}$: 0.8%, 5 N: 0.5%, 23 N: 0.2%).

Figure 4.2 shows that the median CE stiffness (median k_{CE}) in passive muscle (3200 N m^{-1} ; dotted, horizontal, black line), was lower than in almost all active trials (cross (x) scatter $> 1 \text{ N}$). In the active trials, k_{CE} ranged from $\approx 4200 \text{ N m}^{-1}$ at $F = 1 \text{ N}$ to $\approx 16000 \text{ N m}^{-1}$ at $F = F_{max} = 23 \text{ N}$ (for linear fits of MTC and CE data $> 1 \text{ N}$, see Fig. 4.6).

With the use of GAS dimensions from Table 4.1, the k_{CE} values (Fig. 4.2) and force values were scaled to half-sarcomere level: stiffness (k_{hs} , Eq. 2.5) and isometric force (F_{hs} , Eq. 2.6), respectively. A F_{max} of 23 N (Fig. 4.1), the isometric maximum half-sarcomere force is predicted to be $F_{hs} = 445 \text{ pN}$.

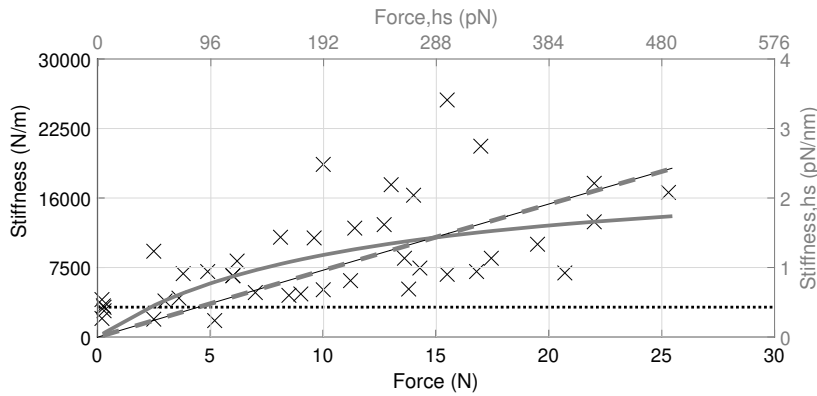


Figure 4.2 | Contractile element stiffness (k_{CE}). Trial specific k_{CE} values were inferred from a 3-parameter fit (Eq. 2.1), with information from one oscillation period after TD (Fig. 2.9). k_{CE} is also given as scaled to the dimension of one representative half-sarcomere (k_{hs} , right axis, see Eq. 2.5). The correspondingly scaled isometric force per half-sarcomere (Eq. 2.6) is given on the upper axis. The solid and dashed grey lines represents the *model1* and *model2* fits, respectively. The dotted, horizontal, black line indicates the median of passive k_{CE} values. The thin, black line underlying the *model2* fit, is the *model1* fit with only the parameter ΔL_{CE} open (fixed $C_{fil} = 0.0067 \text{ nm pN}^{-1}$). This figure is from Christensen *et al.* (2021) [94], reproduced with permission from Springer Nature.

Using the half-sarcomere values of F_{hs} and k_{hs} , it was possible to fit two different model ideas (see Sect. 2.3.5) to the data for better understand the

underlying half-sarcomere mechanics in response to an impact. The solid, grey line in Fig. 4.2 is a least-square fit of *model1* by Fusi *et al.* (2014) [1] to scaled k_{hs} data with passive trials excluded, which predicts a stiffness of 1.8 pN nm^{-1} at 23 N and approaches zero on a slightly curved course, as the isometric force approaches zero. The latter is slightly different from the fitted course of *model2* by Günther *et al.* (2018) [2] (the dashed, grey line in Fig. 4.2), which appears practically linear, with a slightly higher stiffness at 23 N (2.2 pN nm^{-1}) than predicted by *model1*. The fitted parameter values for both models are given in Table 4.2.

Model	c_3 (nm)	ΔL_{CB} (nm)	C_{fil} (nm pN $^{-1}$)
<i>model1</i>	–	85.7	0.4
<i>model1</i> *	–	198	0.0067*
<i>model2</i>	1.2	–	–

Table 4.2 | Parameter estimations. In *model2*, the parameter c_3 represents the pole (at $L_{CB} = -c_3$) in the non-linear cross-bridge force-length relation $F_{CB}(L_{CB})$ (Coulomb drive *in series* to the serial elastic part representing S1, S2 and filaments), which is used to estimate k_{CB} , and eventually k_{hs} . In *model1*, the parameter ΔL_{CB} (nm) represents the average elongation at a fixed force of each cross-bridge acting *in series* to the filament part with compliance C_{fil} . The parameter values of both *model1* and *model2* were determined with the Matlab curve fitting tool ‘cftool’. If the maximum isometric force of a half-sarcomere $F_{CB,max}$ is 445 pN, as estimated in Sect. 4.1, then the original parameter values for *model1* ($[\Delta L_{CB} = 1.56 \text{ nm}$ and $C_{fil} = 1.77 \text{ nm T}_0^{-1}]$ [1]) would translate to $k_{CB} = 285 \text{ pN nm}^{-1}$ ($\frac{445 \text{ pN}}{1.56 \text{ nm}}$) and $k_{fil} = 251 \text{ pN nm}^{-1}$ ($\frac{445 \text{ pN}}{1.77 \text{ nm}}$) at $F_{CB,max}$. This table is from Christensen *et al.* (2021)[94], reproduced with permission from Springer Nature.

* ΔL_{CB} (nm) in *model1* estimated with a fixed $k_{fil} = 150 \text{ pN nm}^{-1}$ value ($C_{fil} = \frac{1}{k_{fil}} = \frac{1}{150 \text{ pN nm}^{-1}} = 0.0067 \text{ nm pN}^{-1}$).

In Fig. 4.3, the energy dissipated is estimated as the area enclosed per one work-loop (Examples in Fig. 4.4), and the respective damping coefficient

(inferred from Eq. 2.1) of the muscle-tendon complex (MTC) and the contractile element (CE). At F_{max} , the MTC and CE dissipated on average $17 \mu\text{J}$ (Fig. 4.3a) and $3.5 \mu\text{J}$ (Fig. 4.3c), respectively. The latter values had increased to $70 \mu\text{J}$ (Fig. 4.3a) and $23 \mu\text{J}$ (Fig. 4.3c), respectively, in the passive experiments (both passive median values). Across all trials, the energy dissipated by the CE and MTC decreased with isometric force, which was in contrast to the found damping coefficients that increased along with the isometric force. In more detail, MTC damping coefficients increased from around 2.2 N s m^{-1} in a passive muscle to about 5.1 N s m^{-1} in active muscle above 10 N (Fig. 4.3b). With regard to the CE damping coefficient, the latter trend was more unclear due to data scatter, though, the damping coefficient seemed to increase from $\approx 9 \text{ N s m}^{-1}$ in a passive muscle to $\approx 12.8 \text{ N s m}^{-1}$ in active muscle at F_{max} (Fig. 4.3d).

As with the CE stiffness, the dissipated CE energy and the CE damping coefficient were also scaled to a half-sarcomere. These scalations were done using Eq. 2.7 and Eq. 2.8, respectively (right and upper axes in Fig. 4.3c,d). Accordingly, the energy dissipated in the CE ranged from 68 zJ in the median passive half-sarcomere to 10.4 zJ at F_{max} , and the CE damping coefficient was $\approx 1.1 \mu\text{N s m}^{-1}$ in a passive half-sarcomere and $\approx 1.6 \mu\text{N s m}^{-1}$ at F_{max} .

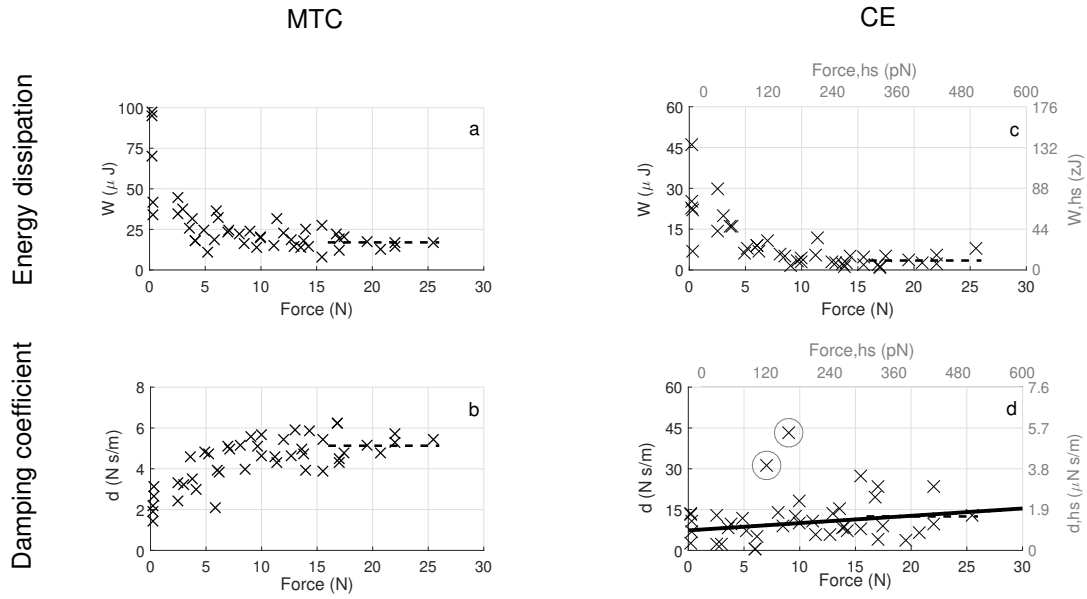


Figure 4.3 | Energy dissipated and viscous damping coefficient of MTC and CE for all isometric and passive force states. a, b, c, d: Data in each trial are calculated for one work-loop, i.e. one oscillation period that spans between TD and the instant when a_{COM} returns closest to zero for the second time. See Fig. 4.4 for an example of one work-loop in a specific trial. For **a, b, c, d**, the dashed, black line is the mean value of all data points > 16 N: $17 \mu\text{J}$, 5.1 N s m^{-1} , $3.5 \mu\text{J} \mid 10.4 \text{ zJ}$ and $12.5 \text{ N s m}^{-1} \mid 1.6 \mu\text{N s m}^{-1}$, respectively. **a:** the energy dissipated by the MTC due to internal material friction. **b:** the viscous damping coefficient calculated for MTC. **c:** the energy dissipated by the CE, with the right and upper axes giving the work (Eq. 2.7) and isometric force (Eq. 2.6) values per half-sarcomere, respectively. **d:** the viscous damping coefficient calculated for the CE, with the right and upper axes giving the damping coefficient (Eq. 2.8) and isometric force (Eq. 2.6) values per half-sarcomere, respectively. Due to the indistinct trend in **d**, a linear fit was added. In **d**, the circles indicate data that were considered outliers and excluded from the fit. This figure is from Christensen *et al.* (2021) [94], reproduced with permission from Springer Nature.

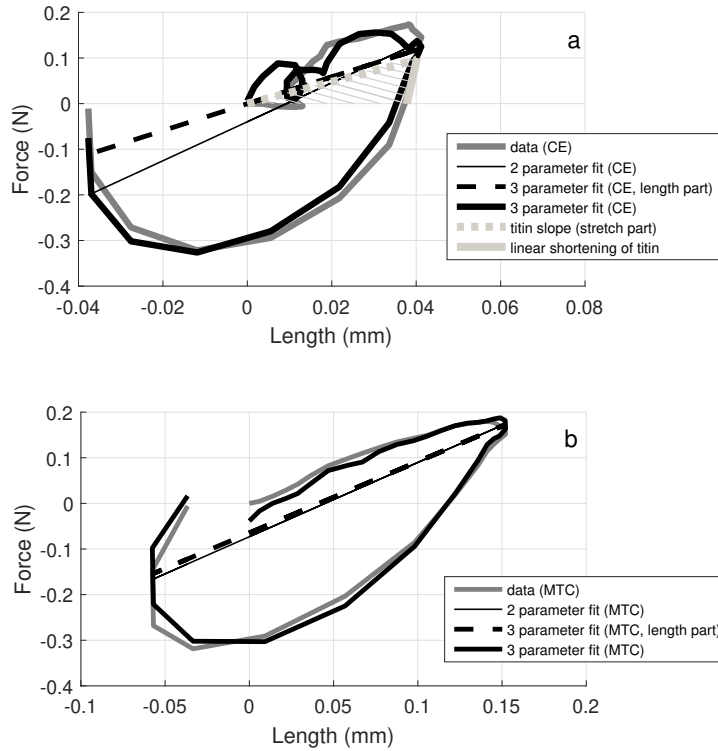


Figure 4.4 | The work-loops of CE and MTC in one passive exemplary trial. The solid, dark-grey loops are the $L_{CE,0}$ or $L_{MTC,0}$ responses, respectively, to ΔF . The solid, thin, black line is the respective linear 2-parameter fit to the data. The solid, black loops depict the respective 3-parameter fits to the data, using the parameters k_i , b_i , d_i of each the function $F_i(L_i, \dot{L}_i)$ (see Eq. 2.1), which linearly depends on length L_i and time rate of length change \dot{L}_i ; the dashed, black line is the respective length-dependent contribution. In **a**, the dotted, light-grey line shows a linear fit to isolated titin stretch data [54], and the solid, light-grey line is an idealised shortening path of the titin filament as ΔF returns to zero, for which linearity is assumed as an approximation. **b** is identical to Fig. 2.10a, where it is used to highlight the requirement of the marker data to be processed separately for each camera (see sect. 2.3.3). Both work-loops encompass one oscillation period that spans between TD and the instant when a_{COM} returns closest to zero for the second time (Fig. 2.9). This figure is from Christensen *et al.* (2021) [94], reproduced with permission from Springer Nature.

4.2 Discussion

4.2.1 The influence of muscle stimulation on ischaemia

The muscles in the experiments in Study 2 (chapter 4) were on average stimulated once per 254 seconds for 265 ms, which is roughly half the stimulation interval from the 4 cm falling experiments in Study 1 (once per 428 seconds for 265 ms). Ischaemia has a very strong, yet reversible effect on muscle force generation within one hour of ischaemia [100, 101]. Further, ischaemia seems so dominant for GAS isometric force production, that a reduction in stimulation duration had little to no influence on isometric force decline over the course of the experiments. The F_{max} difference between the solid and dashed lines in Fig. 4.1 can be explained by the difference in maximum belly anatomical cross-sectional area in both experiments (here, $A_{CE,max,0} = 96 \text{ mm}^2$, Table 4.1). Since the maximum isometric tension in a muscle is between $2.5 \cdot 10^5 \text{ N m}^{-2}$ [105] and $3 \cdot 10^5 \text{ N m}^{-2}$ [134], and GAS has a pennation angle of 14° under similar isometric conditions [106], the expected F_{max} value is between 21 N and 28 N.

4.2.2 ΔF scaled to half-sarcomere level

In Study 2, the parameters characterising particularly two basic structural properties were taken from literature: The PCSA of the muscle consists of 83% myofibril material [96], and the elementary cell of the cross-sectional filament lattice in sarcomeres has the shape of a parallelogram with an area of 1540 nm^2 (Fig. 6.9) at optimal half-sarcomere length (1150 nm [95]). With the measured maximum muscle stress (240 kN m^{-2}) value, the corresponding $F_{hs,max} = 445 \text{ pN}$ value for a half-sarcomere can then be estimated by use of the two parameter values just given above.

To estimate the uncertainty of the predicted $F_{hs,max}$ value, it may be assumed that only 80 % [50, 135] of the PCSA is myofibril material, and that the interplanar d(1,0) lattice distance is 40 nm² [50] (the shape of the elementary cell is either calculated as a square or a parallelogram). In Table 4.3, a summary of the parameter variations given above with data on maximum isometric muscle stress likewise taken from literature, e.g. from two prominent papers [53, 68]. Accordingly, since the measured muscle stress (240 kN m⁻²) value is identical to Piazzesi *et al.* (2007), the percentage variance of $F_{hs,max}$ is about 25 % ($\frac{554 \text{ pN} - 445 \text{ pN}}{445 \text{ pN}}$), depending on the parameters used for the $F_{hs,max}$ calculation (Table 4.4).

Data	Symbol	Unit	Source
240	σ	kN m ⁻²	text [53]
206	σ	kN m ⁻²	[table 2] [68]
40	d(1,0)	nm	d(1,0) = 40 nm [50]
0.8	r	a	80% of PCSA are myofibrils [50, 135]
0.83	r	a	83% of PCSA are myofibrils [96]
1600	A	nm ²	$d(1,0)^2$
1848	A	nm ²	$d(1,0)^2 \cdot 2 \cdot \frac{1}{\sqrt{3}}$

Table 4.3 | Literature data to infer F_{hs} . The two stress values from literature were used to infer force ($F = \sigma \cdot A$ or $F = \sigma \cdot A \cdot \frac{1}{r}$) for a representative half-sarcomere. The length values of the elementary cell's interplanar d(1,0) lattice distance in a half-sarcomere and the myofibril density (see Fig. 6.9) are from independent literature sources. The area of the elementary cell was then either calculated as a square or a parallelogram. This table is from Christensen *et al.* (2021)[94], reproduced with permission from Springer Nature.

Piazzesi <i>et al.</i> (2007) [53]	Lombardi <i>et al.</i> (1992) [68]
$240 \frac{\text{kN}}{\text{m}^2} \cdot 1540 \text{ nm}^2 \cdot 10^{-3} \cdot \frac{1}{0.83} = 445 \text{ pN}$	$206 \frac{\text{kN}}{\text{m}^2} \cdot 1540 \text{ nm}^2 \cdot 10^{-3} \cdot \frac{1}{0.83} = 382 \text{ pN}$
$240 \frac{\text{kN}}{\text{m}^2} \cdot 1600 \text{ nm}^2 \cdot 10^{-3} \cdot \frac{1}{0.8} = 480 \text{ pN}$	$206 \frac{\text{kN}}{\text{m}^2} \cdot 1600 \text{ nm}^2 \cdot 10^{-3} \cdot \frac{1}{0.8} = 412 \text{ pN}$
$240 \frac{\text{kN}}{\text{m}^2} \cdot 1848 \text{ nm}^2 \cdot 10^{-3} \cdot \frac{1}{0.8} = 554 \text{ pN}$	$206 \frac{\text{kN}}{\text{m}^2} \cdot 1848 \text{ nm}^2 \cdot 10^{-3} \cdot \frac{1}{0.8} = 476 \text{ pN}$

Table 4.4 | $F_{hs,max}$ estimations. The variations in estimated $F_{hs,max}$ in two papers using literature data from Table 4.3. This table is from Christensen *et al.* (2021)[94], reproduced with permission from Springer Nature.

4.2.2.1 Titin's property in passive muscle fibre

For the low drop heights experiments, the mean initial GAS force in passive muscle measured by the force transducer was 0.25 N, with an added ΔF peak of 0.2 N as a response to the impact, which means that estimated initial passive force and the dynamic force change for a half-sarcomere as a response to the impact were 4.8 pN and 3.9 pN (Eq. 2.6), respectively. The median passive strain peak with ΔF was about 0.8%, which corresponds to an about 10 nm stretch peak per half-sarcomere (titin filament). Under the assumption that six titin filaments are attached to one myosin rod [60, 61], and the slope of the force-length relation of a single titin filament, measured during fixed-rate stretches, is 0.05 pN nm⁻¹ [54] between 0.8 pN and 1.5 pN, then the overall six-titin slope in a passive half-sarcomere would be 0.3 pN nm⁻¹. The single-titin slope was estimated at 1000 nm s⁻¹ stretch rate [54], which is practically the same as the rates measured for a half-sarcomere ($\approx 1100 \text{ nm s}^{-1}$), as the median passive stiffness is 0.4 pN nm⁻¹, the dynamic force change is

3.9 pN, and the time that passed between TD and this dynamic force change is 9 ms (Fig. 2.9).

Although some studies suggest that only four titin filaments are associated with one myosin, the most popular estimation is six titin filaments per myosin. The mismatch is probably due to the difference in actin filament arrangement in the Z-line and A-band (see Sect. 1.2.1.3). Here, six titin associated with one myosin is assumed because six titin filaments are consistent with titin mass estimations in a sarcomere [60].

To understand how titin might influence the passive macro CE, the estimated titin slope was scaled to one specific passive trial: the CE work-loop in Fig. 4.4a. The scaled titin force-length relation was examined while hypothesising two different, somehow extreme, conditions that may determine the work-loop return path from maximum elongation ($\Delta F > 0$) back to $\Delta F = 0$. As ΔF returns to zero, the titin filament would, in the respective two extreme cases, either shorten along the measured ΔL_{CE} path (Fig. 4.4a, solid, light-grey line), or along the same 0.3 pN nm^{-1} titin slope that applies to the stretch path (Fig. 4.4a, dotted, light-grey line). If titin re-shortens along the measured ΔL_{CE} path, this would resemble a course of titin shortening after stretches at least an order of magnitude [54] longer than estimated here. In this case, titin accounts for half (1.8 zJ , hatched area in Fig. 4.4a) of the 3.5 zJ dissipated CE energy for $\Delta F > 0$.

On the other hand, Ig and PEVK unfolding events has been shown to occur above 6 pN [54, 136], which is far greater than the estimated $\frac{3.9 \text{ pN}}{6} = 0.65 \text{ pN}$ for ΔF . Therefore, if the unfolding events are the cause for a titin's viscosity, then titin might respond as a nearly non-dissipative (conservative) material within the low $\Delta F = 0.65 \text{ pN}$. For the latter extreme case, titin would account for 84% of the 2870 N m^{-1} passive CE stiffness value in the Fig. 4.4a

example and 75% of the 3200 N m^{-1} median passive CE stiffness value, both estimated from a 3-parameter fit (Eq. 2.1).

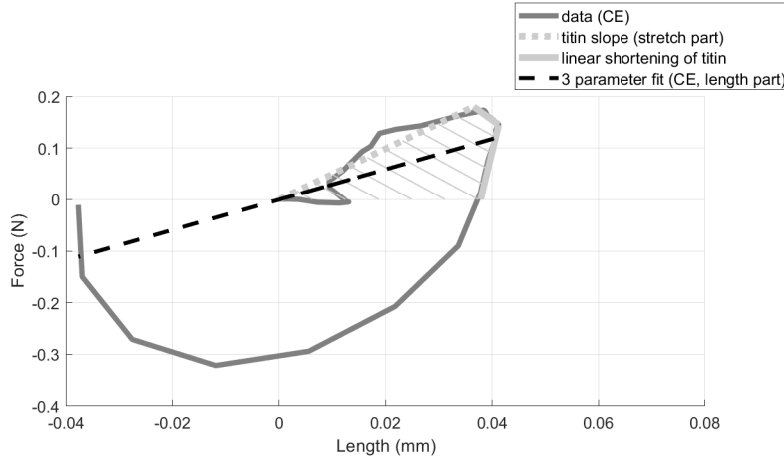


Figure 4.5 | An example of titin contribution in the passive CE. Both the inferred titin stiffness contribution (grey, dotted line) and dissipated energy by titin (hatched area) in CE estimated from single-titin experiments with a 1000 nm s^{-1} stretch rate [54]. The Figure shows the titin stiffness contribution and dissipated energy by titin, under the assumption that each single titin filament from segment I105 to Mis-7 [137] is *in-vivo* coupled with a "rigid" myosin filament (150 pN nm^{-1} [53]). The solid, dark-grey loops are the $L_{CE,0}$ response to ΔF and the dashed, black line is the respective length-dependent contribution. The $L_{CE,0}$ response to ΔF is the same as in Fig. 4.4a.

Another possibility is that the found 0.3 pN nm^{-1} is closer to double that because titin runs through the myosin filament in the A-band [138, 54, 137]. The titin sequence from I105 to Mis-7 is inside the myosin filament [54, 137], which is approximately 50% of the titin length [54, 139]. Thus, the alternative titin stiffness contribution in a half-sarcomere is 0.6 pN nm^{-1} when

substituting 50% of the *in-sereis* titin stiffness with myofilament stiffness (150 pN nm^{-1} [53]). This change in titin stiffness increases titin's passive stiffness contribution to 4940 N m^{-1} in the passive CE (visualised in Fig. 4.5), which as above, have two limit conditions. The first is that titin is purely elastic, and titin will shorten along the same titin slope that applies to the stretch path (Fig. 4.5, dotted, light-grey line). If this is the case, then the stretch of passive CE is determined by titin stiffness and the shortening of passive CE by some other sarcomere property. The second limit condition is that titin re-shortens along the measured ΔL_{CE} path. If that is the case, then titin accounts for 100% (3.7 zJ , hatched area in Fig. 4.5) of the dissipated energy in passive CE (3.5 zJ). Note that the titin property estimations in Fig. 4.5 do not consider any potential titin stiffness regions that might dominate the overall pure titin stiffness as, for example, the PEVK region.

On a final note, titin is a visco-elastic material [54, 136], and titin's ability to dissipate energy does not only depend on velocity. Titin's energy dissipation also depends on contractile history and time between each stretch/shortening contraction [54]. Furthermore, the resistance of passive muscle to movement (and thus its stiffness) increases with time at rest and is reduced by movement [140]. Thus, the large deviations in energy dissipated in the passive trials might relate to either the time between the last active trial and the passive one, the time between dissection and the passive trial, or the total number of trials for a specific muscle. However, unfortunately sample size is too small, and the data too few to further explore any of these potential correlations.

4.2.3 Wobbling mass findings fitted to two half-sarcomere model ideas

For better understanding cross-bridge mechanics, the parameters of two CE models (see Sect. 2.3.5) were fitted (Table 4.2), *model1* [1] and *model2* [2], to reproduce measured CE stiffness k_{CE} (Fig. 4.2).

Regarding *model1*, the best fit of k_{hs} predicted 1.8 pN nm^{-1} at F_{max} , which yielded parameter values of cross-bridge deflection ($\Delta L_{CB} = 85.7 \text{ nm}$) and myofilament stiffness ($k_{fil} = 2.5 \text{ pN nm}^{-1}$) that are factors of 55 and $\frac{1}{34}$, respectively, from earlier model estimations [1].

As a consequence of the estimated 85.7 nm work-stroke for *model1*, the stiffness of a single cross-bridge would be 0.05 pN nm^{-1} if the force for a single cross-bridge is 4 pN [53, 36]. Vice versa, if a force for a single cross-bridge were 100 pN, then the cross-bridge would have a realistic [141, 34, 108] stiffness of 1.2 pN nm^{-1} . Therefore, it seems unlikely that *model1* in this form can explain the low k_{hs} values found in these experiments, without either compromising values for generally accepted work-stroke length [141, 142], force, or stiffness [53, 34, 108]. In accordance with the original model formulation of *model1*, both the cross-bridge stiffness k_{CB} and the filament stiffness k_{fil} are free parameters. However, if $k_{fil} = 150 \text{ pN nm}^{-1}$ applies as in *model2*, then the work-stroke would be higher than the estimated 85.7 nm. A fixed $k_{fil} = 150 \text{ pN nm}^{-1}$ would also make the k_{hs} fit of *model1* appear more linear as predicted by *model2* in Fig. 4.2, due to the then forced change in myofilament compliance ($C_{fil} = \frac{1}{k_{fil}}$) and ΔL_{CB} ratio (Table 4.2). The latter is expected since both models assume a contractile compartment *in-series* within a sarcomere.

Contrary to *model1*, *model2* assumes a non-linear force-length relationship of the Coulomb-actuating cross-bridge part in the CE, which depends

on the pole value in the cross-bridge force-length relation (c_3). A change in c_3 does neither affect the force nor the work-stroke length measured from the cross-bridge's optimal state. However, c_3 does change $\frac{dF}{dL}$ with changing cross-bridge position. With $c_3 = 1.2$ nm (Table 4.2), k_{hs} would be 2.2 pN nm $^{-1}$ at F_{max} (Fig. 4.2). Under the same $k_{fil} = 150$ pN nm $^{-1}$ assumption as above, the overall stiffness value of the cross-bridge part k_{CB} for *model2* is 2.2 pN nm $^{-1}$ (Eq. 2.11) at F_{max} ($n_{CB,max} = 90$), practically making $k_{CB} \approx k_{hs}$. The latter stiffness is a factor 5 from an estimated $k_{CB} = 10$ pN nm $^{-1}$, which is the overall stiffness of the cross-bridge part at F_{max} when calculated with the parameters given in the original paper [2] (Eq. 2.10). For a *model2* $F_{CB}(L_{CB})$ comparison, see Appendix Fig. 6.8. In addition, the 2.2 pN nm $^{-1}$ does not seem compatible with the originally suggested [2] parameter values of *model2*, since the latter choice in Günther *et al.* (2018) [2] predicts the course of the Coulomb force to be nearly linear in the length range of the work-stroke, and the corresponding Coulomb force stiffness contribution for a single cross-bridge to be approximately 0.11 pN nm $^{-1} = \frac{10 \text{ pN nm}^{-1}}{90}$ (here, 0.024 pN nm $^{-1} = \frac{2.2 \text{ pN nm}^{-1}}{90}$).

The difference between originally estimated 10 pN nm $^{-1}$ and the measured 2.2 pN nm $^{-1}$ may be due to the dynamics inherent to the shock-waves that propagated through the CE after the frame made contact with the ground, which potentially caused some local sarcomere compression. If compression were to occur, then the sarcomeres here could be dominated by the low 0.01 - 0.02 pN nm $^{-1}$ bending stiffness of the myosin sub-fragment S2 [143, 144]. That local sarcomere compression can occur seems plausible, because, in rare trials macroscopic CE shortening was observed to precede elongation *after* TD (see Sect. 2.2.4). However, due to insufficient spatial resolution, an adequate examination has not been possible so far.

Although *model2* appears to better explain the findings in Fig 4.2, previ-

ous applications of *model1* have been proven very robust [1, 145, 146], with k_{hs} either inferred from rapid step-in-length experiments [145] or 4 nm peak-to-peak oscillations per half-sarcomere at 4000 Hz [1, 146]. However, according to step-in-length, or -force simulations [2] to reproduce the half-sarcomere force recovery phase following a rapid step in length (T2 curve [141, 34, 108]) with *model2*, the force-length relation of the Coulomb force that drives the lever arm is nearly compensated by parallel friction within the first ≈ 0.1 ms [Fig. 7] [2]. Diminishing displacements within the Coulomb drive strongly suggests that the Coulomb contribution to k_{hs} is, likewise, practically friction-neutralized at very high frequencies such as 4000 Hz. The latter seems to be supported by experimental data, since a half-sarcomere needs to elongate 4 nm to achieve a force enhancement of 180-200% at F_{max} (≈ 3500 Hz), whereas an 8 nm elongation accompanies the same force at 100 Hz [147]. In fact, there have even been half-sarcomere stiffness estimations as low as $k_{hs} = 10$ pN nm $^{-1}$ for <50 Hz [148] and in slow ramp experiments [149].

Despite the MTC and CE stiffness fit courses shown in Fig.4.6, correlate well with other findings [53, 150], the exact number of formed cross-bridges is unknown. Piazzesi *et al.* (2007) [53] also estimated that the maximum number of formed cross-bridges is ≈ 90 from single fibre experiments. If $n_{CB,max} = 90$, then the force of a single cross-bridge is ≈ 5 pN ($\frac{445 \text{ pN}}{90}$), a value at which mechanical, structural, and energetic approaches seem to converge about (4-5 pN) [38, 151]. The estimated k_{hs} values for both models are robust towards the exact number (within limits) because for 90 formed cross-bridges, the stiffness of a single cross-bridge is 0.06 pN nm $^{-1}$ ($\frac{5 \text{ pN}}{85.7 \text{ nm}}$, *model1*) and 0.024 pN nm $^{-1}$ ($\frac{2.2 \text{ pN nm}^{-1}}{90}$, *model2*).

4.2.4 Work done in MTC, CE and half-sarcomere

The energy dissipated by the MTC at F_{max} was calculated as $17.0 \mu\text{J}$ (Fig. 4.3a). If GAS dissipates $17.0 \mu\text{J}$, then the *m. gastrocnemius medialis* head would (scaled by ACSA) roughly account for $8.5 \mu\text{J}$, which is only 21% of the $40 \mu\text{J}$ previously estimated for Wistar *m. gastrocnemius medialis* in one work-loop at 50 Hz with 1 N peak-to-peak force [44] for one oscillation period. All experiments here corresponds to only half of that peak ΔF , because the impact only corresponds to half of an oscillation period. For the experiments in Chapter 4 (Study 2), $\Delta F = 0.2 \text{ N}$ was practically constant across all trials, of which *m. medialis* would then roughly account for 0.1 N. This latter value is about 20% of the comparable 0.5 N force change (half oscillation period) in Ettema and Huijing (1994) [44], which is in perfect accordance with the 21% ratio of $8.5 \mu\text{J}$ and $40 \mu\text{J}$ (or $17.0 \mu\text{J}$ and $80 \mu\text{J}$).

At F_{max} , the energy dissipated by the CE was $3.5 \mu\text{J}$ (Fig. 4.3c). Using Eq. 2.7, and assuming that the maximum number of myosin heads in a half-sarcomere bound at F_{max} is $n_{CB,max} = 90$ [53], the energy dissipated per cross-bridge is $\frac{10.4 \text{ zJ}}{90} = 0.12 \text{ zJ}$ ($1.2 \cdot 10^{-22} \text{ J}$) for a fresh and fully stimulated muscle (Fig. 4.3c). To put 0.12 zJ into perspective, the free energy ΔG_{ATP} available from ATP hydrolysis within a cell is 54 kJ mol^{-1} for rabbit psoas (fast-twitch) and 66 kJ mol^{-1} for rabbit soleus (slow twitch) [152], which corresponds to 90 zJ and 110 zJ per ATP molecule, respectively [153]. Reported values for cross-bridge thermodynamic efficiency, i.e. the fraction of ΔG_{ATP} converted into work, is around 21% for mouse *m. extensor digitorum longus* (fast) and 45% for tortoise *m. rectus femoris* (slow) [153]. The ΔG_{ATP} value for mouse *m. extensor digitorum longus* suggest that for a muscle dominated by fast-twitch fibres like GAS, the mechanical work available per one ATP molecule

split is around $0.21 \cdot 90 \text{ zJ} = 19 \text{ zJ}$. Therefore, one impact for the GAS would lead to an 0.6% ($\frac{0.12}{19}$) energy loss per cross-bridge at F_{max} , because the myosin is believed to be bound to actin for 450 ms under isometric conditions [36, 154], and the wobbling impact response does not take more than 25 ms (Fig. 2.9).

On the other hand, if GAS was pre-activated by only 20% before an impact as in humans [155] and the isometric force scales linearly with activation and the number of attached myosin heads [53] (see also Fig. 4.6), then the energy loss per cross-bridge would be 7.9% for an impact, because the dissipated energy per half-sarcomere at $F = 5 \text{ N}$ is about 27 zJ (Fig. 4.3c), and the number of myosin heads bound in a half-sarcomere may be approximately $n_{CB} = 0.2 \cdot n_{CB,max} = 18$. In the latter more realistic case, one cross-bridge may dissipate about $2 \cdot 7.9\% \approx 16\%$ of the mechanical work available (19 zJ) due to the impacts, since the stride cycle for a rat hindlimb is 300 ms [156], which is 100 ms shorter than the myosin actin bound state.

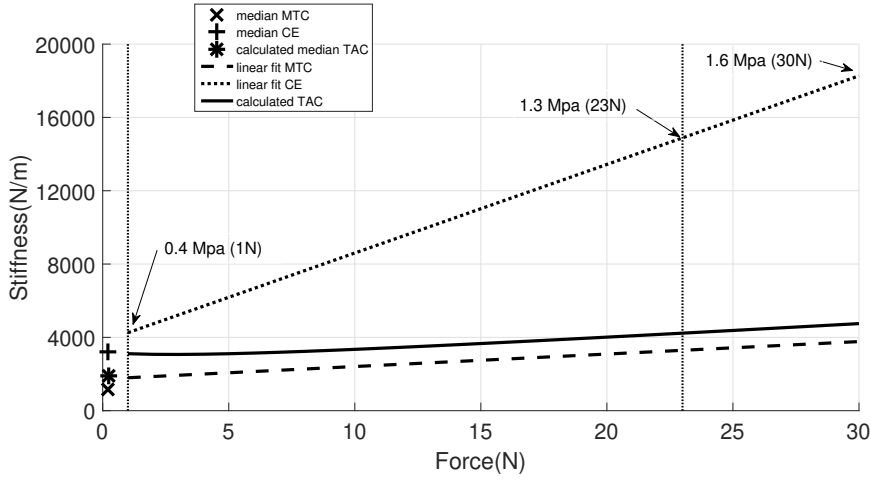


Figure 4.6 | TAC stiffness (k_{TAC}) from linearly interpolated stiffnesses of CE (k_{CE}) and MTC (k_{MTC}) at TD. This figure shows MTC subdivided into a tendon-aponeurosis-complex (TAC) and a CE compartment. TAC was inferred with the assumption that k_{MTC} consisted of an *in series* k_{CE} (see also Sect. 2.2.3). The dotted, black line is the linear fit of all measured k_{CE} values (Fig. 4.3). At 1 N, 23 N, and 30 N, Young’s modulus was calculated for CE using Eq. 2.5 and data from Table 4.1. The dotted, vertical, black lines mark 1 N and 23 N. The dashed, black line is the linear fit of all measured k_{MTC} values, and the solid, black line is the inferred k_{TAC} . ‘Cross’ and ‘plus’ are median values for passive GAS k_{MTC} and k_{CE} , respectively. ‘Asterisk’ is the passive muscles’ estimated k_{TAC} inferred from median k_{MTC} and k_{CE} . This figure is from Christensen *et al.* (2021) [94], reproduced with permission from Springer Nature.

4.2.5 The damping coefficient in MTC, CE and half-sarcomere

The determined damping coefficient d can be interpreted to represent, together with stiffness k and mass m , a GAS MTC that responds visco-elastically to the impact by a damped harmonic oscillation around an operating point at the isometric force level F . From this, the damping strength can be assessed by comparing d with the critical damping coefficient $d_{crit} = 2\sqrt{k m}$,

i.e., by calculating $\zeta = \frac{d}{d_{crit}}$. As can be seen in Fig. 4.3b, the inferred damping coefficients at 3 N, 5 N and 7 N are 3 N s m^{-1} , 4 N s m^{-1} and 4.5 N s m^{-1} , respectively. The corresponding stiffnesses are 1930 N m^{-1} , 2070 N m^{-1} and 2240 N m^{-1} (Fig. 4.6), and the GAS mass is on average 1.9 g (Table 4.1). From this, the damping ratio for the MTC at $F = 5 \text{ N}$ is $\zeta = 1$, as well as $\zeta = 0.8$ and $\zeta = 1.1$ for 2.5 N and 7.5 N, respectively. As it is assumed that the 20% pre-activation level of leg muscles [155] right before leg impacts in human running also applies to a rat's GAS, the MTC is critically damped at 20% of F_{max} (Fig. 4.1), under-damped for activity lower 20%, and slightly over-damped for higher activity levels.

If the muscle force directly relates to muscle activity [53, 150] (see also stiffness fits in Fig. 4.6), then the 20% of F_{max} in Fig. 4.2 is the same as the pre-activation in human GAS before TD (20%) [155]. Accordingly, the number of cross-bridges before an impact relates to soft tissue vibration control in the first few milliseconds after TD. Several studies have experimentally investigated the association between muscle activation and almost critical damping of muscle vibration in response to an impact [28, 29, 24], which lead to the muscle-tuning paradigm [29]. However, a limitation of conducting impact experiments with human subjects is the inability to decouple any effect of leg geometry, joint compliance and muscle activity. Conversely, a benefit of this work's ex-vivo setup is the direct control over GAS isometric force generation and the impact situation: soft tissue MTC properties and conditions affecting its vibration responses can be manipulated independently of the impact strength (falling height).

In contrast, the CE part is always slightly over-damped across the whole isometric force range, as $\zeta = 1.3$ ($d = 7.6 \text{ N s m}^{-1}$, $k = 4250 \text{ N m}^{-1}$) at $F = 1 \text{ N}$ and likewise $\zeta = 1.2$ ($d = 12.8 \text{ N s m}^{-1}$, $k = 13800 \text{ N m}^{-1}$) at $F = F_{max} = 23 \text{ N}$.

This suggests, that the CE system is to return both as smoothly and as quickly at the same time to its equilibrium state, or it may be important for the CE not to overshoot its equilibrium state. The latter may potentially have higher importance as the force-length relationship of the work-stroke is non-linear, with even decreasing stiffness of a cross-bridge if the sarcomere is elongated (see inset at the right top in Fig 2.11).

Chapter 5

Comparing studies: fibre material responses to changes in impact amplitude

5.1 Relationship between critical strain and Coulomb force

The strain, and in particular critical strain, in CE for an 0.35 N impact has been discussed extensively in Study 1 (Chapter 3), whereas Study 2 (Chapter 4) centred around the energetic costs and the low stiffness estimated in the half-sarcomere. Both experimental setups (4 cm experiments and 1 cm experiments, respectively) are, thus, more or less discussed separately. This is primarily due to being different studies, the data processing difference between both studies (Sect. 2.3.3) and secondarily because the fundamental stiffnesses in each experiment, whether it be k_{MTC} or k_{CE} , are calculated differently. For the 4 cm experiments (Chapter 3), k_{MTC} or k_{CE} include only elongation

information between TD and 1 sample after maximum material elongation (e.g. Fig. 2.5). For the 1 cm experiments (Chapter 4), the stiffness, although also using Eq. 2.1, is calculated with the information of an entire work-loop (Fig. 4.4). For a comparison between the two methods of processing data, Figure 5.1 shows, in one exemplary trial (the same trial as in Fig. 4.4), the difference between the two methods of calculating stiffness. Accordingly, if the estimated fibre stiffness contained both fibre elongation and shortening information, then $k_{CE} = 2950 \text{ pN nm}^{-1}$ (Fig. 5.1a) but 5360 pN nm^{-1} with only elongation information (Fig. 5.1c). For k_{MTC} , the estimated stiffness value varies from 1560 pN nm^{-1} to 1490 pN nm^{-1} in Fig. 5.1d and d, respectively. Therefore, if the information of a work-loop is reduced to only the lengthening (initial) part, values of Young's modulus may be significantly over-estimated. However, the difference in data processing methods does not influence the estimated maximum fibre strains, which also have robustness regarding the camera non-synchronicity problem (see Sect. 2.3.3).

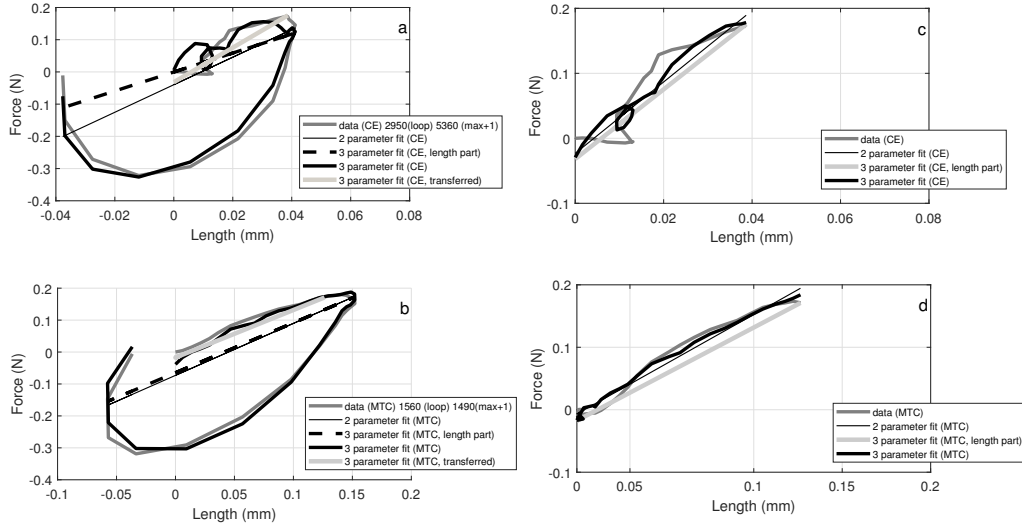


Figure 5.1 | Comparison of stiffnesses calculated with either "loop" or elongation information. **a** and **b** are the same CE and MTC work-loops figures as in Fig. 4.4. Thus, in **a** and **b**, the solid, dark-grey loops are the $L_{CE,0}$ or $L_{MTC,0}$ responses, respectively, to ΔF . The solid, black loops depict the respective 3-parameter fit to data, and the dashed, black lines are the associated length parts (see also Eq. 2.1). For direct comparison, both thick, light-grey lines in **a** and **b** are the transferred 3-parameter length parts from **c** and **d**. However, **c** and **d** fits are only to the instant after the ΔF peak. $k_{CE} = 2950 \text{ pN nm}^{-1}$ in **a**, and $k_{CE} = 5360 \text{ pN nm}^{-1}$ in **c**. The variation in k_{MTC} is lower as $k_{MTC} = 1560 \text{ pN nm}^{-1}$ in **b**, and 1490 pN nm^{-1} in **d**. **a** and **b** are from Christensen *et al.* (2021) [94], reproduced with permission from Springer Nature.

Sect. 3.2.2 discussed the critical strain in fibre material and visualised this in Fig. 3.4. With two boundary assumptions, the text and figure explained or showed how much strain the fibre material can endure before a cross-bridge forcibly detaches (critical strain limit). In the most likely scenario (upper boundary, red line in Fig. 3.4), the fibre material exceeds the critical strain limit when GAS generates an isometric force lower than 11.8 N.

This critical strain limit is inferred from known rupture force between actin and myosin bond [35] and cross-bridge property values estimated in

rapid (above 3000 Hz) step-in-force [53, 108] or oscillation experiments [1].

However, contrary to these rapid step-in-force experiments, Sect. 4.2.3 introduced the term Coulomb force to explain the low half-sarcomere stiffness in dynamic impact situations that a rat would experience running at an intermediate velocity (60 Hz, Fig. 2.9). Accordingly, the actuating Coulomb force-length relation/characteristic that drives a cross-bridge is friction-inhibited at very high frequencies (3000 - 4000 Hz). Thus, failing to take the Coulomb force characteristic and protein friction into account when estimating the critical strain limit in a half-sarcomere can lead to erroneous estimations because the Coulomb force-length relation/characteristic alters the half-sarcomere stiffness k_{hs} at optimal length with a factor of $\frac{1}{34}$ (see *model1* and *model2* comparisons in Table 4.2).

The literature is currently sparse with data that support the inclusion of an actuating Coulomb force in a half-sarcomere or very low half-sarcomere stiffnesses in general. Even in studies that estimate the critical force limit for forcible detachment of cross-bridges, or vice versa, the critical strain limit in muscle fibre experiments, induce rapid perturbations (>4000 Hz) [157, 146, 158]. Therefore, in an attempt to determine a physiological relevant critical strain limit (60 Hz, Fig. 2.9), the fibre strains from the 4 cm falling height experiments are here compared to Nishizaka *et al.* (1995) [35] rupture force experiments (see Table 5.1). Nishizaka *et al.* (1995) [35] estimated the rupture force between myosin and actin by slowly pulling them apart until cross-bridge rupture occurred at 9 pN.

4 cm experiments	Data	Formula	Data source
temperature	23-25°	—	text in Sect. 2.1.6
L_{hs}	1150 nm	—	[text] [95]
stretch rate	86 nm s ⁻¹	$\frac{0.6 \cdot 1150 \text{ nm}}{8 \text{ ms}}$	Fig. 3.2b
critical strain	0.68%	—	case (ii) in Fig. 3.4

Nishizaka [35]	Data	Formula	Data source
temperature	28-30° C	—	[text] [35]
L_{hs}	1150 nm	—	[text] [95]
stretch rate	10 nm s ⁻¹	$\frac{200 \text{ nm} - 190 \text{ nm}}{3 \text{ s} - 2 \text{ s}}$	[Fig. 2a, Fig. 2b] [35]
k_{hs}	0.9 pN nm ⁻¹	$\frac{9 \text{ pN} - 4 \text{ pN}}{29 \text{ nm} - 23.5 \text{ nm}}$	[Fig. 2b] [35]
critical length	10 nm	9 pN ÷ 0.9 pN nm ⁻¹	—
critical strain	0.87%	10 nm ÷ 1150 nm ⁻¹ · 100	—
$k_{hs,alternative}^{\dagger\dagger}$	1.3 pN nm ⁻¹	$\frac{9 \text{ pN} - 5 \text{ pN}}{29 \text{ nm} - 26 \text{ nm}}$	[Fig. 2b] [35]

Table 5.1 | The Coulomb force’s influence on CE strain. An overview of the data used to compare the CE strains in the 4 cm experiments and inferred literature CE strain in physiologically relevant conditions. Data were taken from either 4 cm falling height results or Nishizaka *et al.* (1995) [35]. If the **data source** notes “—” (no source), then the **formulas** contain values from elsewhere in the table.

†† An alternative calculated k_{hs} starting from a cross-bridge that generates 5 pN.

The inferred strain to generate a rupture force of 9 pN [35] is 0.86% (calculations are in Table 5.1), which is almost identical to the upper limit case in Fig. 3.4 (0.68%, black and red lines intersect in the figure) estimated from fast oscillation experiments (above 3000 Hz [1, 53]). Using the alternative cross-bridge stiffness $K_{hs,alternative}$ in Table 5.1, the inferred critical strain limit is 0.6% instead of 0.86%. Thus, the upper limit case in Fig. 3.4 is within the range of strain limits inferred from literature with lower stretch velocity (rate) as in these experiments, which means that the critical strain in a half-sarcomere is independent of the Coulomb force contribution to half-sarcomere stiffness. A possible explanation is that the cross-bridge stiffness in *model2*, when stretched beyond the work-stroke range at $L_{CB} > 11$ nm (see also Appendix Fig. 6.8) will increase rapidly because the cross-bridge is nearing its mechanical limit. In *model2*, the stiffness of a single cross-bridge $k_{CB} = 2.3$ pN nm⁻¹ (Eq. 6.44) at the end of the work-stroke (end of solid line at $L_{CB} = 0$ in Appendix Fig. 6.8) where the lever arm between the two charges, which drives the myosin head (L_1 in [Fig. 2][2]), becomes zero. Stretching the cross-bridge in the opposite direction, beyond the attachment site $L_{CB} > 11$ nm, might increase the cross-bridge stiffness to a similar high stiffness value as in the $L_{CB} = 0$ nm region (up to 2.3 pN nm⁻¹), making the force-length curve in Appendix Fig. 6.8 mirrored at the isometric operating point (7 nm, 4 pN).

5.2 Fibre strain: a comparison between two falling heights

Figure 5.2 shows the maximum fibre strains (CE part) in the 1 cm falling height experiments. As with all 1 cm trials, the fibre strain is calculated sepa-

rately for each camera and subsequently presented as mean values (Sect. 2.3.3). In the figure, the strain values are almost entirely half the strain values given in Fig. 3.4 for identical generated isometric forces. Furthermore, the dynamic force fluctuation ΔF is nearly 50% higher in the 4 cm experiments when compared to the 1 cm experiments. A direct comparison across falling heights of fibre material strain versus force fluctuation is in Fig. 5.3, which separates the isometric force into intervals of 5 N: 0-5 N, 5-10 N, 10-15 N, 15-20 N, 20-25 N, 25-30 N, and passive trials. The figure conflates the data from Fig. 3.4 and Fig. 5.2, and also includes linear fits linking the isometric-force-ranked data points of each the respective 1 cm ($\Delta F = 0.2$ N) and the 4 cm trial ($\Delta F = 0.35$ N) within the same isometric force interval, e.g. 0-5 N.

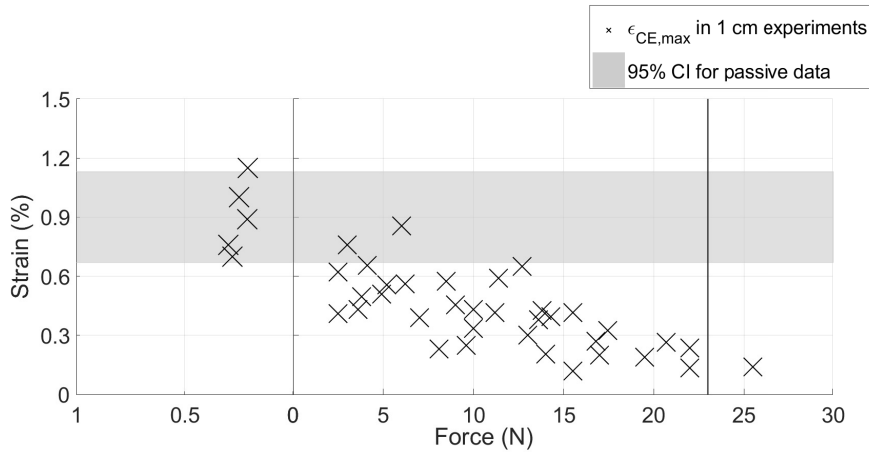


Figure 5.2 | Maximum shock-wave-induced (‘dynamic’) fibre material strain for 1 cm falling height Maximum CE strain data $\epsilon_{CE,max}$ for fully active muscles on the right side of $F = 0$ and for non-stimulated (‘passive’) muscles on the left. The grey-shaded region indicates the range of values from trials with passive muscle with a 95% confidence interval (CI). The two thin vertical, black lines indicates either $F = 0$ or $F = F_{max} = 23$ N (extrapolated F_{max} for 1 cm data, Fig. 4.1).

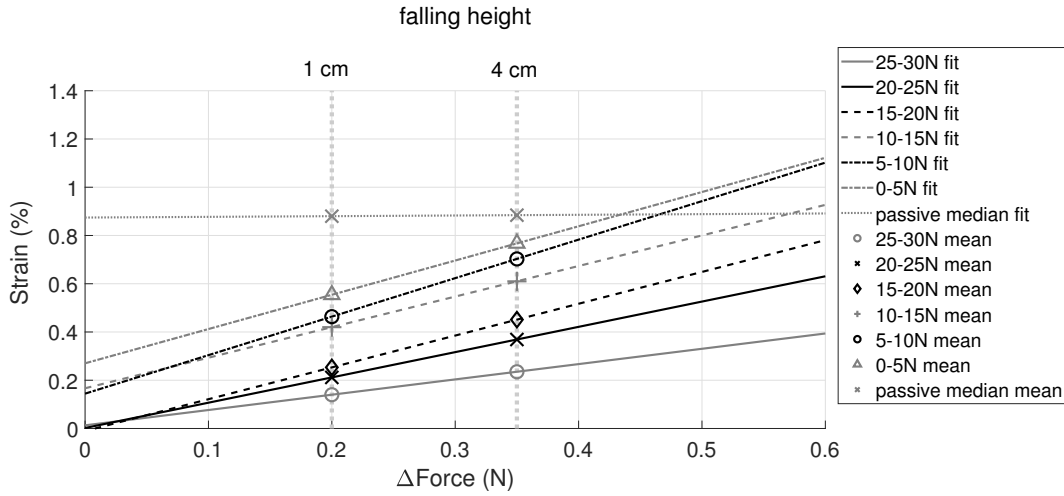


Figure 5.3 | A comparison of the fibre material strain in study 1 (0.35 N) and study 2 (0.2 N). Each marker point represents the arithmetic mean maximum shock-wave-induced (‘dynamic’) fibre material strain in one of the following ranges: passive, 0-5 N, 5-10 N, 10-15 N, 15-20 N, 20-25 N, or 25-30 N. The marker points are either distributed at 0.2 N or 0.35 N, which are the respective peak ΔF at either 1 cm or 4 cm falling height. All CE strains at 0.2 N are from Fig. 5.2, and CE strains at 0.35 N are from Fig. 3.4. All lines (dashed, dotted etc.) are linear regressions fitted separately to the two data points each regression line goes through.

Both *model1* and *model2* assume that the half-sarcomere stiffness consists solely of cross-bridge and myofilament stiffness $k_{hs} = \frac{u \cdot k_{CB,max} \cdot k_{fil}}{u \cdot k_{CB,max} + k_{fil}}$ (Eq. 6.49), an assumption that is also common in literature [1, 53, 146]. According to the linear fits in Fig. 5.3 above an isometric force of 15 N (either grey circles or black crosses or diamonds fitted to 0.2 N and 0.35 N), this simple model assumption holds up to at least $\Delta F = 0.35$ N because all three fits comply with the strain-force relation and intersect at 0,0. However, when the isometric force in GAS starts to decline (either grey plus signs, black circles, or grey triangles), the linear fits no longer intersect at 0,0 suggesting that the fibre strain becomes more dominated by *in-parallel*, passive connective tissue as stiffness seems to be added to the cross-bridge-only value that is

effective at higher isometric force values. In the passive experimental trials, the fibre strain is almost constant regardless of the height from which the frame was dropped (horizontal, grey, dotted line). This trend can either be due to a very scattered set of passive data, whereby the real physiological trend remains unknown or because the passive stiffness that solely acts in passive muscle is non-linear around 0.9% half sarcomere strain. Below an isometric force of 15 N, the ΔF -strain relation must be non-linear because no impact force adds if strain increases. Unfortunately, the number of experiments with variation in the drop heights are too few to determine where exactly the non-linearity exists and how it emerges.

5.3 From quadruped to human locomotion

5.3.1 The fibre strain in human GAS

As seen in Fig. 5.3, the higher the dynamic force change ΔF , the higher the strain in the fibre material (CE part) becomes. A higher dynamic force change must meet a larger ACSA to avoid increasing the fibre strain. If not met, the fibre strain will either increase or decrease depending on the dynamic force change ΔF . Therefore, estimating the fibre strain in human GAS when running, requires known values for both ΔF and the ACSA in humans. The ACSA is in an adult humans male $\approx 4700 \text{ mm}^2$ [159], whereas ΔF , on the other hand, depends on the impact force that causes the muscle to wobble ($\Delta F = \text{mass} \cdot \text{acceleration}$). In skeletal muscle tissue, the fibre material density is $1.06 \frac{\text{g}}{\text{ml}}$ [160] and the mass of rat GAS is 0.002 kg (4 cm experiments: Table 3.1), thus, the volume of rat GAS fibre material is

$$\frac{2 \text{ g}}{1.06 \text{ g (ml)}^{-1}} = 1.9 \text{ cm}^3 \quad . \quad (5.1)$$

This is 215 times lower ($\frac{410 \text{ cm}^3}{1.9 \text{ cm}^3}$) than the volume in human *m. gastrocnemius medialis and lateralis* of 410 cm^3 [161]. With a mass of $0.43 \text{ kg} = 215 \cdot 0.002 \text{ kg}$, the volume ratio between the human GAS and the entire wobbling mass in the posterior of human shank muscles $0.29 = 0.43 \text{ kg} \div [1.5 \text{ kg}]$ [19], is practically the same as determined elsewhere (0.33 , excl. *m. plantaris*) [161]).

Further, the vertical acceleration of the human shank's wobbling mass is 260 m s^{-2} [Fig. 2C] [21] in response to an impact when running at 4.8 m s^{-1} [21]. To estimate the kinematics of the shank's wobbling mass, the authors drew a grid on the posterior part of the lower leg and captured the wobbling movement with high-speed cameras, an approach similar to how the COM of the rat GAS wobbling mass is estimated here. The wobbling mass value of 260 m s^{-2} reached was estimated using a symmetric windowed-sync filter with a seven-point Blackman window, 0.01 s after TD.

If the wobbling mass value of 260 m s^{-2} is representative for the acceleration in the human GAS, as it lies direct beneath the skin and takes up most of the grid in [Fig. 1] [21], then $\Delta F_{hum} = 112 \text{ N} = 260 \text{ m s}^{-2} \cdot 0.43 \text{ kg}$, which is 320 times higher than in rats. Of course, for the same CE reference length of 18 mm (Table 3.1), the stiffness in human GAS is much higher due to the larger ACSA (see also Eq. 2.5 or $k_{CE,hum}$ in Eq. 5.3). In the rat, the ACSA of GAS is 91 mm^2 (Table 3.1), whereas the human maximum ACSA of GAS is 4700 mm^2 [159], which makes the GAS difference between humans and rats a factor of 52 ($\frac{4700 \text{ mm}^2}{91 \text{ mm}^2}$). Therefore, the strain in human GAS seems much higher than in rat, because a factor of 320 is much higher than the factor of 52 difference in the anatomical cross-section area. Even assuming that the human GAS is fully activated at TD, which could be the case in sprinting,

the GAS CE strain in humans ($\epsilon_{GAS,hum}$) may reach 1.3% as

$$\epsilon_{GAS,hum} = 1.3\% = \left(\frac{\Delta F_{hum}}{k_{CE,hum}} \div L_{CE,0} \right) \cdot 100 \quad (5.2)$$

$$= \left(\frac{112 \text{ N}}{9050 \text{ N m}^{-1} \cdot \frac{4700 \text{ mm}^2}{91 \text{ mm}^2}} \div 0.018 \text{ m} \right) \cdot 100 \quad . \quad (5.3)$$

From Eq. 5.2 and Eq. 5.3 it seems simply mandatory for the passive properties to effectively limit the strain in human GAS when sprinting to work properly because the scaling factor between ΔF is higher than the ACSA scaling factor. It is, however, most likely that the fibre strain converges when nearing the critical strain limit (lower border of the grey shaded area in Fig. 3.4) and has an upper limit at about 1% strain, i.e. the upper border of the grey shaded area in Fig. 5.3. For that reason, the CE strain value of 1.3% predicted by scaling is probably unrealistic high, as the passive connective tissue in-parallel to the cross-bridges is supposed to constrain excessive fibre strain. To put the estimated human GAS strain into perspective, $\epsilon_{GAS,hum} = 3.3\%$ would hold if GAS were activated by only 20% at TD, as stated for running at moderate speeds [155]. It is worth noting that the human GAS strain estimations are likely upper estimations or ‘worst-case’ scenarios as the wobbling mass of the shank of 260 m s^{-2} here is assumed to equal the acceleration of GAS’s COM. Two of the most influential reasons for the GAS acceleration being lower than the shank wobbling mass acceleration are that, firstly, not all skin movement is due to muscle wobbling. Secondly, there might well be some degree of interaction between the muscles within the compartment of the posterior shank, and particularly the deeper parts of the GAS may interact with the shank bone. Accordingly, specifying each single calf muscle’s COM acceleration from the entire shank segment’s or possibly just part’s accelerations requires detailed knowledge of each muscle’s

properties (e.g. TAC and CE ratio) and anatomy.

Chapter 6

Conclusion

6.1 Study 1

This present work provides the first experimental data of muscle wobbling during physiological relevant impacts (initial contact phase during running).

The dynamic strain of rat GAS muscle fibres under physiological, shock-wave-induced stretch conditions saturates below a stress of about 40% the maximum isometric value. As the fibres were initially at their optimum lengths, this saturation may be due to counteracting forces by passive, connective tissue within or surrounding the sarcomeres: initial, passive forces are ca. 0.1-0.2 N (Fig. 3.4), which is comparable to the maximum dynamic force change of 0.2-0.4 N (left y-axis of Fig. 3.3). In rat fully active and fresh muscle, the fibre strain is 0.2% in response to impact. Accordingly, cross-bridges are bound down to 11.8 N (40% of the maximum isometric muscle force). Because submaximal muscle force represents the ordinary locomotor condition, the results show that forcible, eccentric cross-bridge detachment is a common, physiological process even during isometric muscle contractions.

Measured MTC stiffness k_{MTC} (2400-3450 Nm⁻¹), calculated CE's Young's

modulus E_{CE} (0.75-1.8 MPa), and inferred stiffness k_{TAC} (5600-6700 Nm⁻¹) of the ‘tendon-aponeurosis complex’ (TAC: arranged in series to the CE) matched well with values from literature (see Sect. 3.2.2.1). From this, it follows that k_{TAC} is dominated by properties of the aponeurosis region rather than the tendon because the values are about 50 times lower than would be expected from mammalian tendons’ Young’s modulus $E_{tendon} \approx 1.5$ GPa [162, 126] and the rats’ anatomical data (Table 3.1).

The calculated wobbling mass eigenfrequency is already predictive regarding the overall muscle and therefore body size. It is, however, descriptive regarding an MTC’s physiological and anatomical design. A model that formulates the eigenfrequency as a function of the corresponding design parameters would, thus allow, to gain further insight into how functional demands under common shock wave conditions formed MTCs during evolution. However, a daring statement thus far is that the frequency spectrum in terrestrial locomotion is broader in bigger animals. Although the found centre of mass acceleration is similar for a running rat’s *m. gastrocnemius medialis* and *lateralis* ≈ 165 m s⁻² and running human’s leg muscles (in shank ≈ 270 m s⁻² and thigh ≈ 160 m s⁻²), phase relations of the leg’s wobbling masses in response to the impact differ. In humans, maximum vertical accelerations of the segmental muscle masses in both thigh (20 ms) and shank (5 ms) have a wider temporal separation of bone and muscular movement compared to rat (0.6 ms). Thus, it seems that wobbling mass dynamics have higher functional relevance during impacts in larger animals because of a larger temporal separation of bone and muscular movement.

6.2 Study 2

In the 1 cm falling height experiments, the estimated energy dissipated per cross-bridge at maximum isometric muscle force F_{max} is 0.6% due to an impact. It is unlikely that the pre-activation required before touch-down generates F_{max} for each stride; instead a lower pre-activation, as found in humans, is more likely. Accordingly, it is very likely that the Wistar *m. gastrocnemius*, *in-vivo* and at intermediate running speed, dissipates by impacts about 16% of the mechanical work available throughout the period of hydrolysing one ATP molecule, and that the GAS is such designed that the entire MTC is critically damped at TD due to the pre-activation. In addition, it is very likely that several structural —such as titin— contributions to passive viscoelasticity act in parallel to the cross-bridges. However, the experiments were not suited to resolve such potential single passive contributions across the isometric force range of active muscles.

Despite the estimated maximum isometric force in a half-sarcomere being estimated at 445 pN and agreeing with estimations in single fibre experiments, the half-sarcomere stiffness is low and declined from 2.2 pN nm^{-1} at maximum isometric muscle force down to 0.4 pN nm^{-1} in a passive half-sarcomere. The scaled half-sarcomere stiffnesses are lower than compared to what has been found in slow ramp experiments for single fibres, and much lower than in rapid step-in-length and 4000 Hz oscillation fibre experiments. The majority of the stiffness difference can be explained by the actuating drive within a cross-bridge being caused by a Coulomb force that is friction-inhibited at very high frequencies, and subsequently by the possibility of local CE compression under an impact. The experiments tried to emulate the impact that a rat would experience at an intermediate speed, which superimposed damped oscillation at roughly 50 Hz to the muscles. It is, therefore,

unlikely that such high perturbations frequencies (≈ 4000 Hz), required to inhibit the suggested Coulomb-originating cross-bridge stiffness, can occur in legged locomotion. It seems there is no getting out of integrating representations of frictional mechanisms, next to muscle inertia, into explanatory models of highly dynamic muscle contraction.

In the passive trials, the measured stiffness scaled to a half-sarcomere is 0.4 pN nm^{-1} . This work probed titin's contribution to passive stiffness with two model assumptions, the first being that titin is solely responsible for the passive half-sarcomere stiffness with the sub-cases being elastic or visco-elastic. If being elastic, then titin accounts for 75% of the work-loop stiffness. In the sub-case of visco-elasticity, titin accounts for 50% of the dissipated energy in a half-sarcomere. The second model assumption is that titin makes up the half-sarcomere stiffness partly in conjunction with myosin filament. For the latter, titin stiffness is equal to the elongation slope in the work-loop, and, if being visco-elastic, then titin makes up 100% of the dissipated energy in passive half-sarcomere.

6.3 Comparing studies

By comparing strain findings here with fibre stiffness, stretch rates and cross-bridge rupture force with literature data, it seems that the critical strain limit for fibre material $\delta_{crit} \approx 0.68\%$ is the same regardless of stretch rates. A possible explanation is that the Coulomb contribution to half-sarcomere stiffness diminish outside the range of a cross-bridge work-stroke (stretching) because the cross-bridge is nearing its mechanical limit. Further, in active GAS, the fibre strain scales linearly with the dynamic force change ΔF when generating an isometric force above $\approx 50\%$ of F_{max} . On the other hand, the

strain data also suggests a non-linearity between fibre strain and ΔF if the half-sarcomere generates an isometric force lower than $\approx 50\%$ of F_{max} because the linear fits to data do not intersect at 0,0. Unfortunately, having only two drop heights are too few to precisely determine the location of that non-linearity.

Scaling the experimental strain findings from rat GAS to human GAS suggests that it is simply mandatory for the passive properties to effectively limit the strain in human GAS when sprinting to work properly because the scaling factor between ΔF is up to 515% ($100 \cdot \frac{320-52}{52}$) higher than the ACSA scaling factor.

6.4 Prospects

This work intended to design an experimental setup that allowed for emulation and capture of single muscle response in bouncy gait. With such an experimental setup, the aim of Study 1 (Chapter 3) was to, for the first time, examine whether cross-bridges in active skeletal muscle are disrupted when strained by shock-waves in the physiological range in legged locomotion. Study 2 (Chapter 4) aimed to better understand the damping and energy dissipation of the whole muscle and the fibre material during wobbling by calculating stiffnesses, damping coefficients, and the energy dissipated during work-loops. From these work-loops, the Study 2 findings were scaled to half-sarcomere level to probe predictions of cross-bridge stiffness values by half-sarcomere models: the first by Fusi *et al.* (2014) [1] and the second by Günther *et al.* (2018) [2].

The results in Fig. 3.4 suggests, that forcible detachment of cross-bridges is common in bouncy gait. However, the fibre strain will likely saturate at higher impact forces (Fig. 5.3), which may be due to counteracting forces by passive connective tissue within or surrounding the sarcomeres, at least at optimal fibre length. Experiments at shorter initial fibre lengths will provide further insight to whether this is an evolutionary well-adapted system design or a result of chosen MTC length.

Inferring the MTC- and, in particular, the CE damping coefficient and energy dissipated was not an easy task. It took quite a long time to properly fine-tune the setup and data processing to estimate these values. However, this tiresome process provided the first experimental data that show the quantity of energy dissipated due to an impact (Fig. 4.3). Consequently, this works findings show that ignoring wobbling in muscle models, especially those emulating legged locomotion [163, 7], can lead to underestimating the energetic costs associated with walking or running. In addition to this, the ability to experimentally show that there is energy dissipated due to wobbling is a vital piece of information when verifying muscle models such as *model2* [2]. However, a particular issue in this model-experiment comparison will be the further comparison to experimental literature data on responses to steps in length and force. The crucial damping strength inconsistency within the structure-based fibre model part, as inferred in Study 2, diverges by more than an order of magnitude from the value inferred from literature data on rapid step responses [141, 34].

This work also examined the scaled titin force-length relation while hypothesising two different, somewhat extreme conditions that may determine the work-loop return path from maximum elongation. This was done to un-

derstand how titin might contribute to the passive fibre material. In the first case (visco-elastic response), titin accounts for approximately half of the dissipated energy in fibre material. In the second case (elastic response), titin would account for 80% of the passive fibre materials stiffness. However, new experiments are needed to accurately map titin's contribution to passive properties in legged locomotion depending on contraction history, falling height, and muscle length.

Finally, the shock-waves that travel through the muscle tissue may cause a mixture of local fibre compression and elongation, as suggested in some experiments (see. Exclusion criteria in Sect. 2.2.4). Accordingly, there may also exist a phase shift between local strains (within the CE region defined in this work). To experimentally verify the existence of any opposing fibre strains and phase shifts, a very local view of the fibre material is needed. An improved camera resolution is a key to answering questions regarding wave propagation. With such an experimental setup, it may be possible to predict longitudinal and transversal waves travel patterns and directions within muscles during impacts. Data that will not increase only the robustness, i.e. verification via stiffness, strains and time constants, but also pinpoint the parameters estimated in Table 4.1 because the CE range for the fibre material might be a mixture of *in-series* local compression and elongation.

Acknowledgements

I would like to thank Prof. Dr. Tobias Siebert and Prof. Dr. Syn Schmitt for providing the interesting topic and securing grants from the ‘Deutsche Forschungs- gemeinschaft’ (DFG) for financial support. I would also like to thank Harald Schubert, previous Direktor des Institute for Laboratory Animal Research und Tierschutz an der Universitätsklinik Jena and his team for the care and anaesthesia of the Animals. Likewise, I would like to thank Dr. O. Till for his help in carrying out the initial experiments.

A special thanks go to Prof. Dr. Tobias Siebert. As my doctoral supervisor and as a muscle physiologist, he gave me the chance to do a doctorate in biomechanics. He gave me the freedom to develop myself what encouraged my independence. Other special thanks go to Dr. Michael Günther. He sharpened my way of thinking through numerous conversations concerning the methodology, results and conclusions drawn therefrom. His high standards in international science shaped my way of working and thinking. Even on the weekend and in the late evening, he willingly answered my questions.

Finally, I will also like to thank the Deutsche Forschungsgemeinschaft for financing me throughout the years it took to complete this work. I am also thankful to all the people, including my family, colleagues, friends, and many more, who gave me valuable input and supported me throughout this work.

Appendix

Pictures of experimental setup and muscle

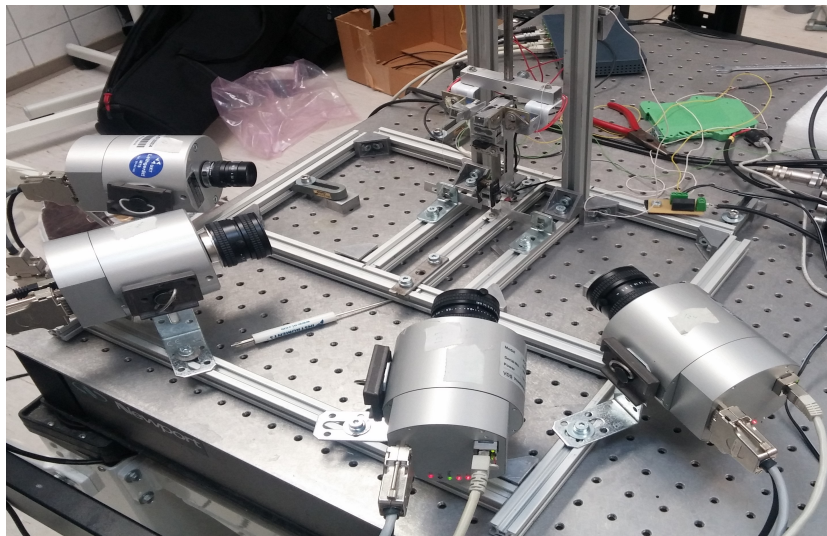


Figure 6.1 | Frontal picture of the experimental setup.

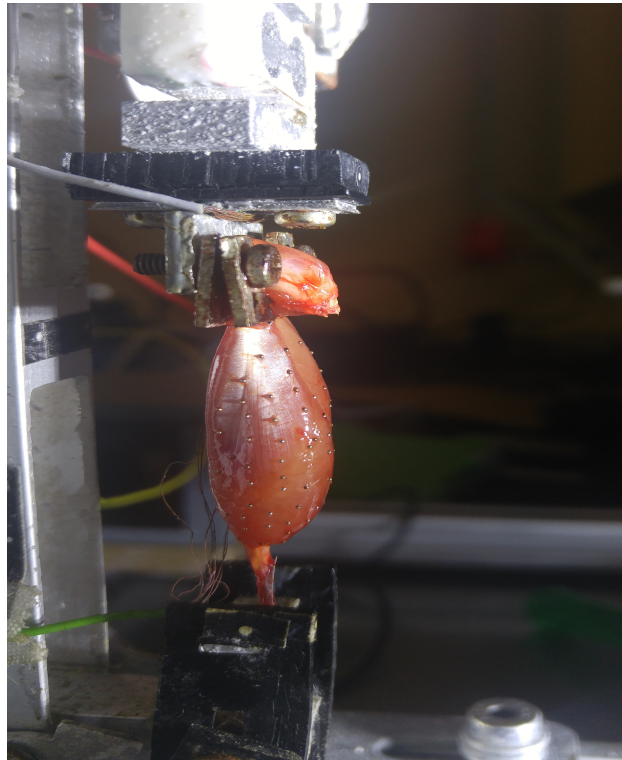


Figure 6.2 | Picture of *m. gastrocnemius lateralis*.

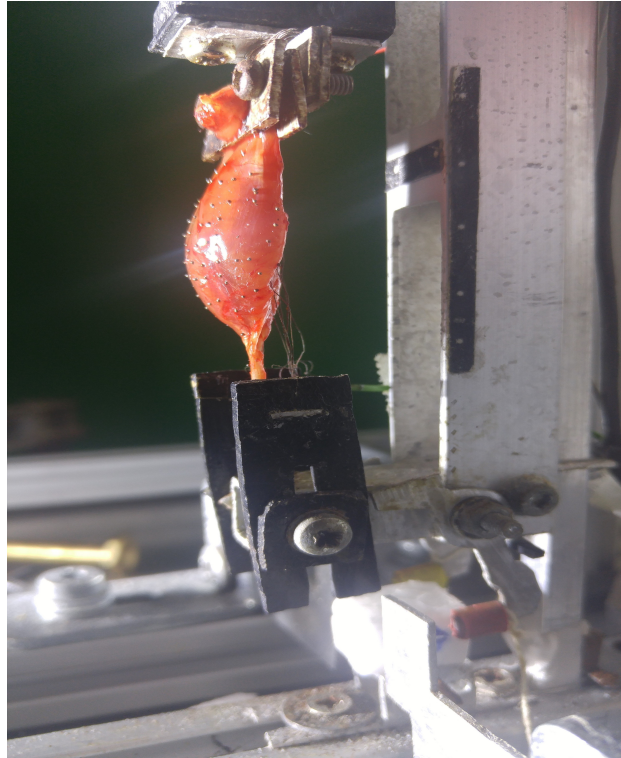


Figure 6.3 | Picture of *m. gastrocnemius medialis*

Installation of HCC Control V5.0.0

The HCC Control software for the HCC-1000 BGE, high-speed VDS Vosskühler cameras is developed for Windows XP operating system. Because VDS Vosskühler has since been incorporated as a branch office of from Allied Vision (Allied Vision Technologies GmbH, 07646 Stadtroda, Deutschland) , there exists no newer version of the software just as the cameras are now legacy cameras with no newer operating system. Currently, the installation steps to make the HCC Control software run on newer OS systems has only been tested on: Windows 7 (x32) and Windows 10 (x32).

- Install HCC Control V5.0.0

- Activation code: B35245396-4AE97-75BE
- Install Acquire Control Setup V4.0.2
 - Choose the Pleora Driver Package Installer (64 version)
- Transfer the content of the 'dll_material' folder to the directory (from USB stick)
- Open HCC Control and click hardware → grabber options
 - Right click on the IP Engine to set IP.
 - Change IP Engine IP Address to 169.254.0.201 (note, for more cameras, each need its own ip from .201 and upwards)

Note: Acquire Control driver:

<https://www.alliedvision.com/en/products/software/acquirecontrol.html>

Static hand-calculations of the frame deflection

For starters, Young's modulus in the aluminium parts were all set to $6.9 \cdot 10^{10}$ Pa. This Young's modulus value is a standard value for aluminium found on the internet¹. Further, although the dimensions and shapes of the frame vary throughout its entirety, the aluminium frame itself can be separated into seven parts, of which three parts are identical. Figure. 6.4a,b and 6.5a,b shows the dimensions of each aluminium part. The latter figure also includes two red dots used to calculate the total deflection of the aluminium frame under an applied force of 25 N (20 N for GAS [83] + 5 N (Eq. 1.48) for the GRF). Note that the separation of each piece is only visual, and it is not physically possible to separate the shown parts.

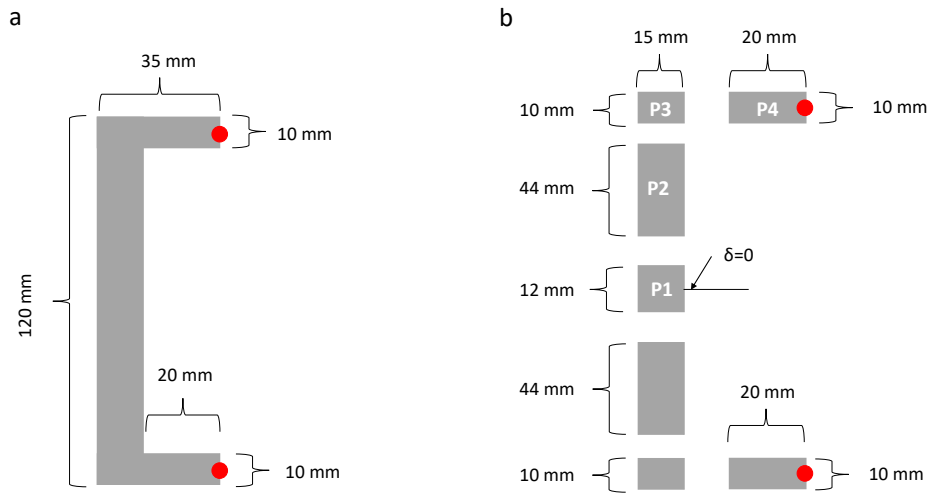


Figure 6.4 |Side view of the frame. Figure **a** shows the profile and dimensions of the aluminium frame backbone and two extrusions. **b** is the aluminium frame segmented into the seven parts used to calculate the deflection of the aluminium frame by hand. In the middle of part *p1* is the deflection of the backbone's centerline $\delta = 0$. The red dots in **a** and **b** are the spots used for calculating the deflection the aluminium frame makes.

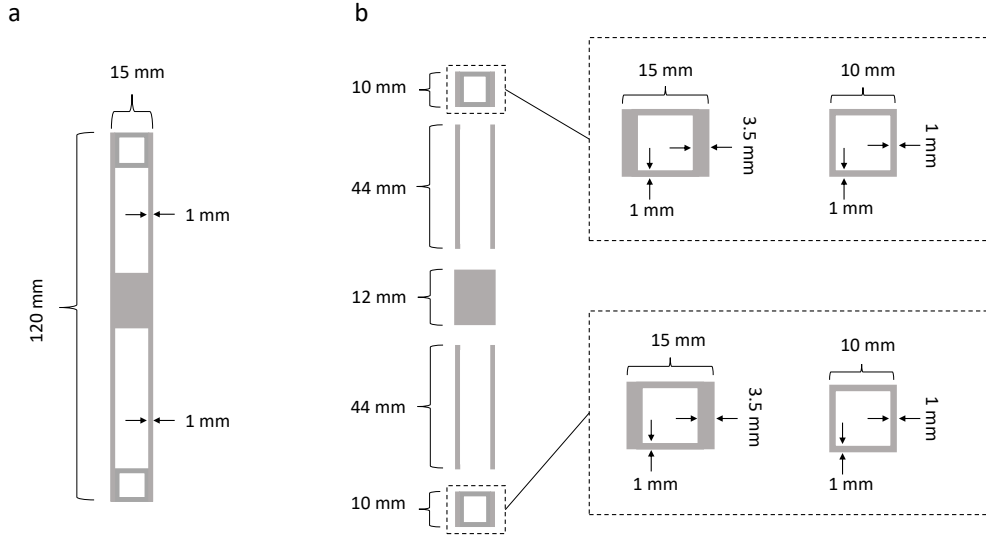


Figure 6.5 |Frontal view of the frame. The frame is shown as a whole in **a** and segmented into five parts in **b**, with the extrusions being further segmented. The dimensions of the separated parts in the zoomed-in views of both extrusions corresponds to $p3$ and $p4$, respectively, in Fig. 6.4b.

Of the seven parts, three of them are identical with their opposite. Therefore, the parts $p1$, $p2$, $p3$, $p4$ can categorise all of the seven parts, where the inertia of each is equal to

$$I_i = \frac{w_i \cdot h_i^3}{12} - \frac{w_{in,i} \cdot h_{in,i}^3}{12} , \quad (6.1)$$

with w and h being outer dimensions of the parts, and w_{in} and h_{in} being the inner dimensions. An example of the inertia for $p4$ is

$$I_{p4} = \frac{0.01 \text{ m} \cdot 0.01^3 \text{ m}}{12} - \frac{0.008 \text{ m} \cdot 0.008^3 \text{ m}}{12} . \quad (6.2)$$

The only exception to finding inertia with Eq. 6.1 is $p2$, which is

$$I_{p2} = 2 \frac{wh^3}{12} = 2 \frac{0.001 \text{ m} \cdot 0.015^3 \text{ m}}{12} \quad (6.3)$$

because p_2 consists of two solid rectangles (Fig. 6.5b). The inertia of all four parts is:

- $I_{p1} = 1.0 \cdot 10^{-9} \text{ m}^4$
- $I_{p2} = 5.6 \cdot 10^{-10} \text{ m}^4$
- $I_{p3} = 3.9 \cdot 10^{-9} \text{ m}^4$
- $I_{p4} = 4.9 \cdot 10^{-10} \text{ m}^4$

When applying a 30 N force at the tip of the frame extrusion, as seen in Fig. 6.5, it creates a bending moment (M_1) of

$$M_1 = F_1 \cdot L_{p4} \cdot \frac{L_{p3}}{2} = 30 \text{ N} \cdot 0.02 \text{ m} \cdot \frac{0.015 \text{ m}}{2} = 0.83 \text{ N m} \quad (6.4)$$

between part p_3 and p_4 . That bending moment will also exist if there is a tangential force (F_2) acting on the tip of the frame backbone being

$$F_2 = \frac{M_1}{L_2} = \frac{0.83 \text{ N m}}{0.005 \text{ m}} = 166 \text{ N} \quad . \quad (6.5)$$

If F_2 acts perpendicular on the frame backbone, then the bending moment at $\delta = 0$ (M_2 , Fig. 6.6) is

$$M_2 = 166 \text{ N} \cdot 0.06 \text{ m} = 10 \text{ N m} \quad . \quad (6.6)$$

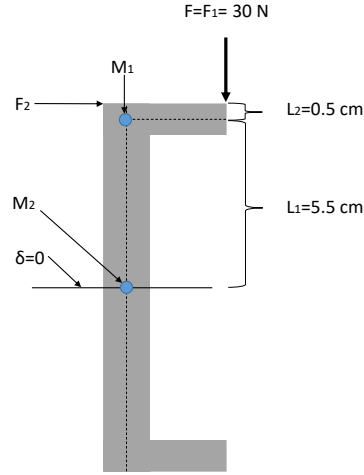


Figure 6.6 | Acting forces and bending moments in the frame. The force F_1 acting at the tip of the upper extrusion creates the bending moments M_1 and M_2 in the centerline (dashed lines). Because the lower part of the frame (beneath the $\delta = 0$ line) is identical to the upper part, all of the 30 N acts at the upper extrusion tip, and the $\delta = 0$ line is fixated when calculating the overall frame deflection. L_1 is the length from the $\delta = 0$ line to the centerline of $p4$, while L_2 is the length from $p4$'s centerline to the top of the aluminium frame.

The angle of rotation in all the frame backbone parts (inferred from Eq. 6.7) is:

$$\theta_i = \frac{F_2 L_i^2}{2 E I_i} + \frac{F_2 L_i L_{add}}{E I_i} \quad (6.7)$$

with L_{add} being the length of the adjacent backbone part. As an example, the angle of rotation at the tip of the part $p1$ is

$$\theta_{p1} = \frac{166 \text{ N} \cdot \frac{(0.012 \text{ m})^2}{2}}{2 \cdot 69 \text{ Pa} \cdot 1 \text{ m}^4} + \frac{166 \text{ N} \cdot \frac{0.012 \text{ m}}{2} \cdot (0.06 \text{ m} - \frac{(0.012 \text{ m})^2}{2})}{69 \text{ Pa} \cdot 1 \text{ m}^4} = 8 \cdot 10^{-4} \quad (6.8)$$

The angle of rotation at the tip of each backbone part is:

- $\theta_{p1} = 8.1 \cdot 10^{-4}$

- $\theta_{p2} = 60 \cdot 10^{-4}$
- $\theta_{p3} = 3 \cdot 10^{-5}$

Knowing the angle of rotation in part $p1$, $p2$ and $p3$ and that the bend centerline arc length is equal to the unbent centerline (L_1 , Fig. 6.6), the vertical deflection of the backbone due to rotation becomes

$$\delta_{\theta,p1,p2,p3} = (L_1 + L_2) \left(\cos \left(\sum \theta_i \right) \cdot (L_1 + L_2) \right) \quad (6.9)$$

$$= 0.06 \text{ m} \cdot \left(\cos \left(6.9 \cdot 10^{-3} \cdot \frac{\pi}{180} \right) \cdot 0.06 \text{ m} \right) \quad (6.10)$$

$$= 4.3 \cdot 10^{-10} \text{ m} \quad . \quad (6.11)$$

In Eq. 6.9, the centerline length L_1 is the same as the arc length ds in a bent centerline because the centerline is not under stress (Eq. 1.9). Lastly, the deflection in part $p4$ due to rotation is

$$\delta_{\theta,p4} \quad (6.12)$$

$$= \tan \left(\sum \theta_i \right) \cdot L_{p4} \quad (6.13)$$

$$= \tan \left(6.9 \cdot 10^{-3} \cdot \frac{\pi}{180} \right) \cdot 0.02 \text{ m} \quad (6.14)$$

$$= 2.4 \cdot 10^{-6} \text{ m} \quad (6.15)$$

at the tip. The deflection of $p4$ (Eq. 1.25) is

$$\delta_4 = \frac{F L_{p4}^3}{3 E_{p4} I_{p4}} = \frac{30 \text{ N} \cdot 0.02^3 \text{ m}}{3 \cdot (6.9 \cdot 10^{10} \text{ Pa}) \cdot (4.9 \cdot 10^{-10} \text{ m}^4)} = 2.4 \cdot 10^{-6} \text{ m} \quad . \quad (6.16)$$

calculated with Euler–Bernoulli beam theory, however, as indirectly hinted to in Fig. 1.5b ($d\theta, dx \approx x$) and Eq. 1.2, the Euler–Bernoulli beam theory relies on the assumption that any plane perpendicular to the centerline will

remain so after the beam is bend. I.e. the Euler–Bernoulli beam theory assumes no transverse shear force in the infinite small sections. Although this is not true, the shear force is negligible when considering slender beams or small deflections. Conversely, if the length thickness ratio of $p4$ is under six or there are large deflections, then the transverse shear forces might no longer be negligible [164, 165]. For these situations, the Timoshenko beam theory takes the shear force into account, which in the case of a cantilever beam, lead to an addition [164] to the Eq. 1.25 expression. Thus the deflection in $p4$ is equal to

$$\delta = \frac{F L^3}{3 E I} + \frac{F L}{k G A} \quad (6.17)$$

where G is the shear modulus, A is the cross-section area, and K is the structures shear coefficient. The latter is very difficult to keep constant because it is a function of frequency, and there is no definitive consensus of the K value. Though, for a thin-walled square tube, the K is estimated [166] to

$$K = \frac{20(I + v)}{48 + 39 v} \quad , \quad (6.18)$$

where v is Poisson’s ratio, which is $v = 0.34$ in aluminium². Even though the parts $p1$ and $p3$ also have high length to thickness ratios, their potential wrong estimated contribution to the vertical deflections are considered negligible, thus, integrating Eq. 6.18 in Eq. 6.17 and the corrected deflection of $p4$ becomes

$$4.4 \cdot 10^{-6} \text{ m} = \frac{30 \text{ N} \cdot 0.02^3 \text{ m}}{3 \cdot (6.9 \cdot 10^{10} \text{ Pa}) \cdot (4.9 \cdot 10^{-10} \text{ m}^4)} + \frac{30 \text{ N} \cdot 0.02 \text{ m}}{0.11 \cdot (2.6 \cdot 10^{10} \text{ Pa}) \cdot 0.0001 \text{ m}^2} \quad (6.19)$$

with $G \doteq 27 \text{ GPa}$ in aluminium³. Adding $4.4 \cdot 10^{-6} \text{ m}$ to the vertical

³<https://www.engineeringtoolbox.com/poissons-ratio-d1224.html>

³<https://www.engineeringtoolbox.com/modulus-rigidity-d946.html>

deflection contributions of parts $p1$, $p2$, $p3$, and the overall deflection of both tips is $2.9 \cdot 10^{-5}$ m:

$$\delta_{max} = 2 \cdot (\delta_{\theta,p1,p2,p3} + \delta_{\theta,p4} + \delta_4) = 1.4 \cdot 10^{-5} \text{ m} \quad . \quad (6.20)$$

To calculate the vertical deflection contribution from $p1$, $p2$ and $p3$ without applying Timoshenko's beam theory might be wrong considering the difference in Eq. 6.16 and Eq. 6.19. However, the difference in vertical deflection is negligible compared to the added deflection from the force transducer, clamps and insulators (Fig. 1.8). On a final note, even though the part $p1$ design is so that it reduces any potential torsion in this critical location. The actual frame torsion was not calculated because any force acting on the frame is limited to the vertical direction.

Least-square fitting

As an example, the black, thick line in Fig. 3.4 is a 2-parameter (Eq. 6.21) least-square fit of all data $F > 12$ N

$$y = a + b \cdot x \quad . \quad (6.21)$$

That can be written in linear matrix form ($y = A \cdot x$) as

$$y = \begin{bmatrix} y_1 \\ y_2 \\ \vdots \\ y_n \end{bmatrix}, A = \begin{bmatrix} 1 & x_1 \\ 1 & x_2 \\ \vdots & \vdots \\ 1 & x_n \end{bmatrix}, x = \begin{bmatrix} a \\ b \end{bmatrix} \quad , \quad (6.22)$$

with $\text{rank}(A) = 1$ with independent columns. a and b are the slope and intersection, respectively. Because the system for A also fulfils $m > n$, i.e. A has more rows than columns, the *left-pseudo-inverse* (or Moore-Penrose inverse)

$$A^+ = (A^t A)^{-1} A^t \quad (6.23)$$

of A can be used to solve Eq. 6.22. In Eq. 6.23, A^t is the transpose of A . With the Moore-Penrose inverse, x in the linear matrix form is equal to

$$x = A^+ y \quad (6.24)$$

$$= (A^t A)^{-1} A^t y \quad , \quad (6.25)$$

where the term $A^t A$ is equal to

$$A^t A = \begin{bmatrix} 1 & 1 & \dots & 1 \\ x_1 & x_1 & \dots & x_n \end{bmatrix} \begin{bmatrix} 1 & x_1 \\ 1 & x_2 \\ \vdots & \vdots \\ 1 & x_n \end{bmatrix} = \begin{bmatrix} n & \sum_{i=1}^n x_i \\ \sum_{i=1}^n x_i & \sum_{i=1}^n (x_i)^2 \end{bmatrix} \quad (6.26)$$

and $A^t y$ to

$$A^t y = \begin{bmatrix} 1 & 1 & \dots & 1 \\ x_1 & x_1 & \dots & x_n \end{bmatrix} \begin{bmatrix} y_1 \\ y_2 \\ \vdots \\ y_n \end{bmatrix} = \begin{bmatrix} \sum_{i=1}^n y_i \\ \sum_{i=1}^n x_i y_i \end{bmatrix} \quad . \quad (6.27)$$

Integrating Eq. 6.26 and 6.27 into 6.24 becomes

$$\begin{bmatrix} n & \sum_{i=1}^n x_i \\ \sum_{i=1}^n x_i & \sum_{i=1}^n (x_i)^2 \end{bmatrix} \begin{bmatrix} a \\ b \end{bmatrix} = \begin{bmatrix} \sum_{i=1}^n y_i \\ \sum_{i=1}^n x_i y_i \end{bmatrix}, \quad (6.28)$$

which rewritten to $x = A^+ y$ for calculating a and b (Eq. 6.29) becomes

$$\begin{bmatrix} a \\ b \end{bmatrix} = \begin{bmatrix} n & \sum_{i=1}^n x_i \\ \sum_{i=1}^n x_i & \sum_{i=1}^n (x_i)^2 \end{bmatrix}^{-1} \begin{bmatrix} \sum_{i=1}^n y_i \\ \sum_{i=1}^n x_i y_i \end{bmatrix}. \quad (6.29)$$

With the inverse in Eq. 6.29 being

$$\begin{bmatrix} n & \sum_{i=1}^n x_i \\ \sum_{i=1}^n x_i & \sum_{i=1}^n (x_i)^2 \end{bmatrix}^{-1} = \frac{1}{n \cdot \sum_{i=1}^n (x_i)^2 + \sum_{i=1}^n x_i \cdot \sum_{i=1}^n x_i} \begin{bmatrix} \sum_{i=1}^n (x_i)^2 & -\sum_{i=1}^n x_i \\ -\sum_{i=1}^n x_i & n \end{bmatrix}. \quad (6.30)$$

Eq. 6.30 reveals, that the system can not be solved, if the determinant is 0.

Solving Eq. 6.29 with the data values $F > 12 N$ extracted from Fig. 3.4, the slope and intersect

$$\begin{bmatrix} -0.03 \\ 0.98 \end{bmatrix} = \begin{bmatrix} 16 & 287.73 \\ 287.73 & 5178.70 \end{bmatrix}^{-1} \begin{bmatrix} 7.52 \\ 121.91 \end{bmatrix} \quad (6.31)$$

is -0.03 and 0.98, respectively.

Model ideas(extended)

model1 [1] According to *model1* (Eq. 6.32), all cross-bridges act *in parallel*, and they are assumed to be arranged *in series* with the myofilaments (actin and myosin), to make up the half-sarcomere stiffness

$$k_{hs}(F_{CB}) = \frac{1}{C_{fil} + \frac{\Delta L_{CB}}{F_{CB}}} \quad . \quad (6.32)$$

Here, $C_{fil} = \frac{1}{k_{fil}}$ is the overall compliance of the myofilaments (k_{fil} their stiffness) and $\frac{\Delta L_{CB}}{F_{CB}} = \frac{1}{k_{CB}}$ the overall compliance of the ensemble of n_{CB} cross-bridges (k_{CB} their stiffness) in a half-sarcomere.

The force generated by a single cross-bridge ($F_{CB,1}$) is assumed to be a constant, with an associated constant deflection (ΔL_{CB}). The overall stiffness of the cross-bridge ensemble, which generates the half-sarcomere force

$$F_{hs}(n_{CB}) = F_{CB}(n_{CB}) = n_{CB} \cdot F_{CB,1} \quad , \quad (6.33)$$

scales linearly, just like the force, with the number of cross-bridges:

$$k_{CB}(n_{CB}) = \frac{F_{CB}}{\Delta L_{CB}} = n_{CB} \cdot k_{CB,1} \quad , \quad (6.34)$$

where $k_{CB,1} = \frac{F_{CB,i}}{\Delta L_{CB}}$ is the stiffness of a single cross-bridge. With known values for k_{fil} and n_{CB} , the overall half-sarcomere stiffness (Eq. 6.32) can also be written as

$$k_{hs}(n_{CB}) = \frac{k_{CB}(n_{CB}) \cdot k_{fil}}{k_{CB}(n_{CB}) + k_{fil}} \quad . \quad (6.35)$$

Since ΔL_{CB} of each cross-bridge is fixed at $\Delta L_{CB} = 1.5 \text{ nm}$ [1], and cross-bridges and filaments are arranged *in series*, the half-sarcomere elongation

is

$$\Delta L_{hs}(n_{CB}) = \Delta L_{CB} + \Delta L_{fil}(n_{CB}) \quad , \quad (6.36)$$

with the filament elongation being

$$\Delta L_{fil}(n_{CB}) = \Delta L_{CB} \cdot \frac{k_{CB}(n_{CB})}{k_{fil}} \quad . \quad (6.37)$$

In accordance with *model1*, the cross-bridge force F_{CB} is transmitted by the filament ($F_{CB} = F_{hs} = F_{fil}$); thus,

$$F_{CB}(n_{CB}) = k_{hs}(n_{CB}) \cdot (\Delta L_{CB} + \Delta L_{fil}(n_{CB})) \quad . \quad (6.38)$$

To reproduce [Fig. 3 A,B,C] [1], k_{hs} can be calculated from Eq. 6.35— and further using Eq. 6.34— with k_{fil} values of either 150 pN nm^{-1} and $k_{CB,1} = 3 \text{ pN nm}^{-1}$ (solid, black line in Fig. 6.7) or $k_{fil} = 90 \text{ pN nm}^{-1}$ and $k_{CB,1} = 1 \text{ pN nm}^{-1}$ (dashed, black line in Fig. 6.7); for this, both k_{hs} variations assume $\Delta L_{CB} = 1.5 \text{ nm}$ [1], thus, $F_{CB,1} = 4.5 \text{ pN}$ or 1.5 pN , respectively. For all four graphs in Fig. 6.7 (including *model2* and an alternative *model2* version), it is assumed that the maximally possible number of cross-bridges in a half-sarcomere sub-unit (i.e. one half-myosin and two actin filaments) is $n_{CB} = n_{CB,max} = 90$ [53].

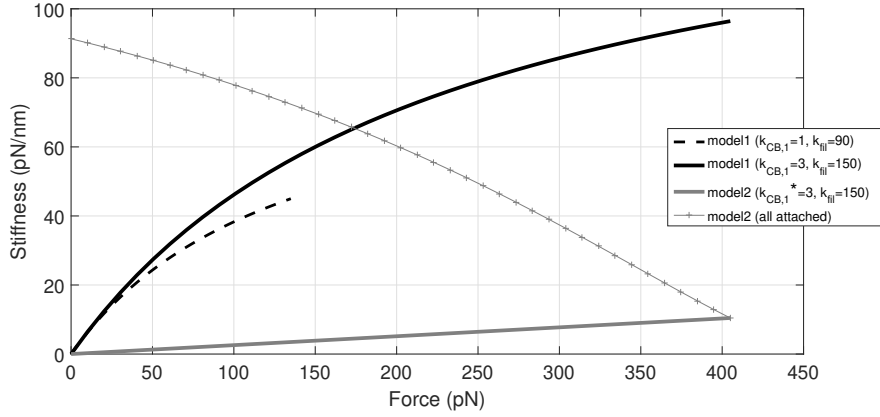


Figure 6.7 | Model predicted stiffnesses as function of half-sarcomere force. The solid, black line is the predicted half-sarcomere stiffness k_{hs} for *model1* if $k_{CB,1} = 3 \text{ pN nm}^{-1}$ (stiffness of a single cross-bridge), $k_{fil} = 150 \text{ pN nm}^{-1}$ (filament stiffness) and a constant $\Delta L_{CB} = 1.5 \text{ nm}$. The dashed, black line is the predicted k_{hs} for *model1* with $k_{CB,1} = 1 \text{ pN nm}^{-1}$, $k_{fil} = 90 \text{ pN nm}^{-1}$ and $\Delta L_{CB} = 1.5 \text{ nm}$. The solid, grey line is the predicted *model2* k_{hs} if parameter values are the same (except $F_{CB,opt,1} = 4.5 \text{ pN}$, see *) as in the original paper for the non-linear $F_{CB}(L_{CB})$ ($k_{CB,1}^* = 3 \text{ pN nm}^{-1}$, $k_{fil} = 150 \text{ pN nm}^{-1}$, $L_{CB,opt} = 7 \text{ nm}$, $c_3 = 4 \text{ nm}$), and force is proportional to number of cross-bridges, with the latter all at their optimal lever coordinate $L_{CB,opt}$. The solid, thin, plus-sign, grey line is k_{hs} predicted from *model2* if the work-stroke changes the generated force with the (representative) lever coordinate instead of the number of attached cross-bridges ($n_{CB,max}$ myosin heads attached). For all calculations, it was assumed $n_{CB,max} = 90$ [53] as the maximum number of cross-bridges. This figure is from Christensen *et al.* (2021) [94], reproduced with permission from Springer Nature.

* $k_{CB,1}$ as in Eq. 6.34 and subsequently used to estimate F_{CB} in Eq. 6.38, which is equal to F_{CB} in Eq. 6.48 that is used to calculate k_{CB} for *model2*.

model2 [2]

The overall idea for *model2* is that a half-sarcomere consists of an active element (AE), a parallel damping element, a serial elastic element and a serial damping element. In particular, the cross-bridge itself is divided into

a catalytic domain and a light chain domain that can rotate, assumed to be actuated by a Coulomb force drive (the AE) with respect to the catalytic domain (together, they represent the S1 part of a myosin molecule). The levered light chain, in turn, generates force (F_{AE}) between the actin and the myosin filaments, which is a non-linear function of the internal lever arm coordinate (L_{AE}) [2]. The serial elastic element in the model includes all parts other than AE (like S1, S2, filaments) in series to the rotational degree of freedom constituting the AE.

To compare *model1* and *model2*, AE and the serial elastic element was the only inclusions of *model2*—leaving out the dampers. It was further assumed that the AE is the same as the cross-bridge in *model1* ($AE \hat{=} CB$) and that the serial elastic element of *model2* corresponds to the filament stiffness k_{fil} in *model1*. With this, the sum force

$$F_{CB}(L_{CB}) = F_{CB,max} \cdot \left(\frac{c_1}{(L_{CB} + c_3)^2} + c_2 \right) \quad (6.39)$$

of all cross-bridges in a *model2*-like half-sarcomere is a non-linear function of the L_{CB} position of the representative cross-bridge. In Eq. 6.39, c_1, c_2, c_3 are parameters and $F_{CB,max}$ is the maximum force that the cross-bridge drive of a half-sarcomere can generate at a corresponding optimal lever coordinate ($L_{CB} = L_{CB,opt}$ see Fig. 6.8); c_1 can be written in terms of c_3 and the optimal cross-bridge lever coordinate:

$$c_1 = \frac{c_3^2 \cdot (L_{CB,opt} + c_3)^2}{c_3^2 - (L_{CB,opt} + c_3)^2} \quad ; \quad (6.40)$$

c_2 (> 1) can be written in terms of c_1 (< 0) and c_3 (> 0):

$$c_2 = \frac{-c_1}{c_3^2} \quad ; \quad (6.41)$$

c_3 fixes the pole coordinate for the model function $F_{CB}(L_{CB})$ where F_{CB} approaches infinity ($L_{CB} = -c_3$).

For Eq. 6.39, the length-derivative of F_{CB} , i.e. k_{CB} , can be expressed as

$$k_{CB} = F'_{CB} = \frac{d}{dL_{CB}} \cdot \left(F_{CB,max} \cdot \left(\frac{c_1}{(L_{CB} + c_3)^2} + c_2 \right) \right) \quad (6.42)$$

$$= F_{CB,max} \cdot c_1 \cdot \frac{d}{dL_{CB}} \cdot ((L_{CB} + c_3)^{-2}) \quad . \quad (6.43)$$

Eq. 6.43, can express the stiffness of the cross-bridges' part as a function of L_{CB} :

$$k_{CB}(L_{CB}) = -\frac{2 \cdot c_1 \cdot F_{CB,max}}{(L_{CB} + c_3)^3} \quad . \quad (6.44)$$

To enable an immediate comparison with the half-sarcomere stiffness predicted by *model1*, it is necessary to replace—by solving Eq. 6.39 for $(L_{CB} + c_3)^2$ and inserting this into Eq. 6.44—the variable length L_{CB} by the force F_{CB} in Eq. 6.44, and find

$$k_{CB}(F_{CB}) = -\frac{2 \cdot c_1 \cdot F_{CB,max}}{\left(\frac{c_1}{\frac{F_{CB}}{F_{CB,max}} - c_2} \right)^{\frac{3}{2}}} \quad (6.45)$$

$$= -2 \cdot c_1 \cdot F_{CB,max} \cdot \left(\frac{\frac{F_{CB}}{F_{CB,max}} - c_2}{c_1} \right)^{\frac{3}{2}} \quad (6.46)$$

$$= \frac{2 \cdot c_2 \cdot F_{CB,max}}{c_3} \cdot \left(1 - \frac{F_{CB}}{c_2 \cdot F_{CB,max}} \right)^{\frac{3}{2}} \quad , \quad (6.47)$$

with the last form (Eq. 6.47) resulting from substituting $c_1 = -c_2 \cdot c_3^2$ (according to Eq. 6.41) into Eq. 6.46 and eventually extracting c_3 and, as much as possible, c_2 from the $(\dots)^{\frac{3}{2}}$ -term. For the values $L_{CB,opt} = 7$ nm and $c_3 = 1.2$ (Table 2) to 4 nm [2], which are characteristics for a cross-bridge, the values of parameter c_2 are close to unity: $c_2 = 1.02$ to 1.15 [2].

Both *model2* and *model1* assume that the stiffnesses of the cross-bridge and filament parts arranged *in series* make up the overall half-sarcomere stiffness. Also in *model2*, just like in *model1*, the isometric force F_{CB} (of a half-sarcomere: $F_{CB} = F_{hs}$) scales linearly with the number of cross-bridges (in a half-sarcomere: n_{CB}), which are all acting at the optimal lever coordinate $L_{CE,opt}$:

$$F_{hs}(n_{CB}) = F_{hs}(u) = u \cdot F_{CB,max} \quad , \quad (6.48)$$

with $u = \frac{n_{CB}}{n_{CB,max}}$ being a normalised factor. Therefore, the stiffness of the cross-bridge part scales likewise linearly with $n_{CB} = \frac{F_{CB}}{F_{CB,max}}$, and the stiffness of the serial arrangement in the half-sarcomere becomes

$$k_{hs}(n_{CB}) = k_{hs}(u) = \frac{u \cdot k_{CB,max} \cdot k_{fil}}{u \cdot k_{CB,max} + k_{fil}} \quad , \quad (6.49)$$

with $k_{CB,max} = k_{CB}(F_{CB,max})$ (Eq. 6.47). In Fig. 6.7, Eq. 6.49 was used to calculate k_{hs} with $n_{CB} = n_{CB,max} 90$, $L_{CB,opt} = 7$ nm and $k_{fil} = 150$ pN nm⁻¹. An alternative version of *model2* (all attached) is also plotted in Fig. 6.7, where the term $u \cdot k_{CB,max}$ in Eq. 6.49 is substituted with Eq. 6.44. Thus, the force per half-sarcomere no longer scales with the number of cross-bridges but with the lever arm coordinate of the representative cross-bridge: all myosin heads are assumed to be always attached ($u = 1 : n_{CB} = n_{CB,max}$) and deflected in their work-stroke so as to generate exactly the force $F_{CB} \leq F_{CB,max}$ demanded.

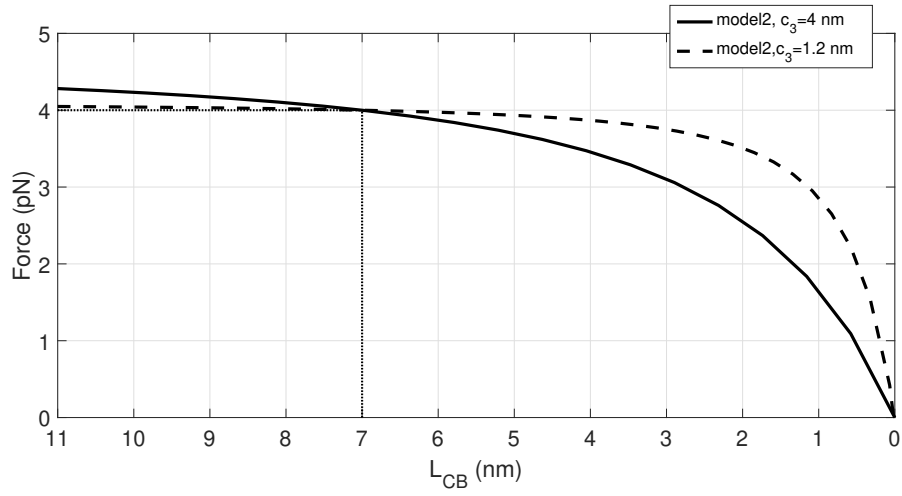


Figure 6.8 | Non-linear $F_{CB}(L_{CB})$ (*model2*). Solid line is the force for a single cross-bridge $F_{CB,1}$ as a function of its lever arm coordinate L_{CB} as originally estimated [2]. Dashed line is $F_{CB,1}(L_{CB})$ as predicted for the measured impact responses (see also Table 2). Horizontal, thin, dotted line and vertical, thin, dotted line indicate optimal force $F_{CB,opt,1}$ and length $L_{CB,opt}$, respectively, for a single cross-bridge as originally given [2]. This figure is from Christensen *et al.* (2021) [94], reproduced with permission from Springer Nature.

Sub-pixel resolution

The term *pixel resolution* describes the amount of detail each image holds, and a higher resolution equals a higher level of detail. Thus, *pixel resolution* refers to the total number of pixels in an image, while *spatial resolution* defines the blurriness or sharpness of each captured image. This means that the clarity of an image is not determined by the number of pixels, but the spatial resolution that also sometimes is given by the unit length of an pixel. The sharpness of an image is determined by shutter speed, focal point and DOF. The shutter speed or exposure time is the time duration exposing the camera sensor to light. The amount of light that reaches the film or image sensor is proportional to the exposure time. The focal point is the point at which light arrays converge, and the DOF is the depth wherein the object is still in focus. The latter is directly related to the focal length, which is the distance from the focal point to the sensor (Fig. 2.2).

In many applications, it is desirable to increase the accuracy of a pixel, i.e. approximate more detail than the camera can allow. Mathematically [167], the resolution can exceed the traditionally limited pixel resolution because the upper limit of an expectable resolution factor r is

$$r < \sqrt{\frac{M}{2\epsilon}} ATS \quad . \quad (6.50)$$

where ATS is the mean amplitude-template-step, M is the size of the template, and ϵ is a grey-noise factor [167]. Choosing 1 as an arbitrary value for both ATS and ϵ with $M = 100$, the expected resolution is

$$0.1 \text{ pixel} = \sqrt{\frac{100}{1 \cdot 1}} \cdot 1^{-1} \quad . \quad (6.51)$$

Radial distances between myosin and actin

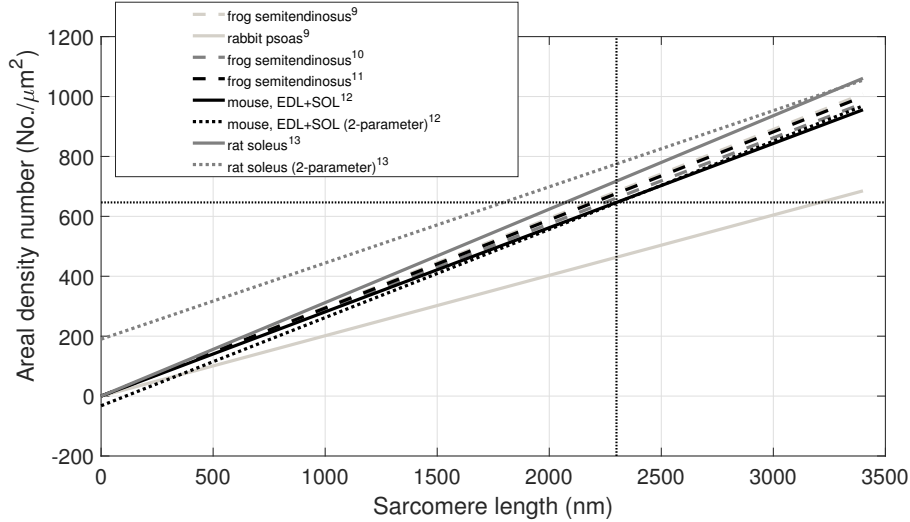


Figure 6.9 | The radial areal density number of myosins in cross-sections of the A-band. The dashed, light-grey line and the solid light-grey line are 1-parameter ($a \cdot x$) fits of frog semitendinosus and rabbit psoas data, respectively (species unknown)[168]. The dashed, grey line is the 1-parameter fit of frog, *Rana temporaria*, semitendinosus[169], and the dashed, black line is the 1-parameter fit of frog semitendinosus (species unknown)[170]. The solid, black and grey lines are 1-parameter fits to data of normal mouse soleus (SOL) combined with extensor digitorum longus (EDL)[171] and rat SOL[172], respectively (both species are unknown). The dotted lines are 2-parameter fits ($a \cdot x + b$) to data of normal mouse EDL combined with SOL [171] and to *Sprague-Dawley* SOL [172] data, respectively. In this work, the radial areal density number of myosins for the combined mouse SOL and EDL data to estimate A_{hs} . The choice of the 1-parameter fit of combined mouse SOL and EDL was due to three criteria: I. The mouse is a mammal. II. Of all animals considered here, the mouse has the most anatomical similarities to the rat of the animals presented here. III. The 2-parameter fit to the data of the mouse is in better agreement with fibril volume constancy (intercept at 0,0) than the 2-parameter fit of the *Sprague-Dawley* SOL data. In addition, the *Sprague-Dawley* data are measured with electron micrographs instead of x-ray diffraction, which typically overestimates the radial areal density number of myosins by 10-20%[173]. The dotted, thin, vertical line marks the optimal sarcomere length ($2.3 \mu\text{m}$) [95, 174] for a Wistar rat gastrocnemius, and the dotted, thin, horizontal line is the corresponding radial areal density number of myosins based on the 1-parameter mouse SOL+EDL fit ($1540 \text{ nm}^2 = \frac{1}{649 \mu\text{m}^2}$). This figure is from Christensen *et al.* (2021) [94], reproduced with permission from Springer Nature.

Author contributions

This work was funded by the Deutsche Forschungsgemeinschaft (DFG) under Grants SI841/7–1,2 and SCHM2392/5–1,2 given to Prof. Dr. Tobias Siebert and Prof. Dr. Syn Schmitt, respectively. Prof. Dr. Tobias Siebert and Prof. Dr. Syn Schmitt, together with Dr. Michael Günther, obtained both grants by drafting and presenting the base idea of this work to DFG, i.e. using high-speed cameras to capture muscle kinematics under impacts. I developed, built the impact apparatus and performed all experiments needed for translating the draft into an experimental design, and in consultation with Dr. Michael Günther, Prof. Dr. Tobias Siebert and Prof. Dr. Syn Schmitt, we developed the scientific questions and aims that this experimental design needed to address.

I drafted chapters 1 - 2.1 and chapter 5 of this work. However, throughout the course of this work, some parts (Study 1 and Study 2) were published in an international scientific journal. The colleagues that contributed to the publications were involved in different ways: through repeated consultation with Dr. Michael Günther, he and I interpreted the data and drafted the manuscript(s). Prof. Dr. Tobias Siebert and Prof. Dr. Syn Schmitt repeatedly revised the manuscript and provided valuable input into the final versions of these publications.

List of publications

Publications in peer-reviews journals

- Christensen, K. B., Günther, M., Schmitt, S. & Siebert, T. Strain in shock-loaded skeletal muscle and the time scale of muscular wobbling mass dynamics. Scientific Reports, 7 (1): 13266, 2017. DOI: 10.1038/s41598-017-13630-7
- Christensen, K. B., Günther, M., Schmitt, S. & Siebert, T. Cross-bridge mechanics estimated from skeletal muscles' work-loop responses to impacts in legged locomotion. Scientific Reports, 11 (1): 23638, 2021. DOI : 10.1038/s41598-021-02819-6

Bibliography

1. L Fusi, E Brunello, M Reconditi, G Piazzesi, and V Lombardi. The non-linear elasticity of the muscle sarcomere and the compliance of myosin motors. The Journal of Physiology, 592(Pt 5):1109–1118, 2014.
2. M Günther, D F B Haeufle, and S Schmitt. The basic mechanical structure of the skeletal muscle machinery: One model for linking microscopic and macroscopic scales. Journal of Theoretical Biology, 456:137–167, 2018.
3. E Ramasamy, O Avci, B Dorow, S Y Chong, L Gizzi, G Steidle, F Schick, and O Röhrle. An efficient modelling-simulation-analysis workflow to investigate stump-socket interaction using patient-specific, three-dimensional, continuum-mechanical, finite element residual limb models. Frontiers in bioengineering and biotechnology, 6:126, 2018.
4. D Suissa, M Günther, A Shapiro, I Melzer, and S Schmitt. On laterally perturbed human stance: experiment, model, and control. Applied bionics and biomechanics, 2018, 2018.
5. I Wochner, D Driess, H Zimmermann, D F B Haeufle, M Toussaint, and S Schmitt. Optimality principles in human point-to-manifold

- reaching accounting for muscle dynamics. Frontiers in computational neuroscience, 14:38, 2020.
6. R R Neptune, C P McGowan, and J M Fiaidt. The influence of muscle physiology and advanced technology on sports performance. Annual review of biomedical engineering, 11, 2009.
 7. Ajay Seth, Jennifer L Hicks, Thomas K Uchida, Ayman Habib, Christopher L Dembia, James J Dunne, Carmichael F Ong, Matthew S DeMers, Apoorva Rajagopal, Matthew Millard, et al. Opensim: Simulating musculoskeletal dynamics and neuromuscular control to study human and animal movement. PLoS computational biology, 14(7):e1006223, 2018.
 8. A V Hill. The effect of load on the heat of shortening of muscle. Proceedings of the Royal Society of London. Series B. Biological sciences, 159(975):297–318, 1964.
 9. A F Huxley. Muscle structure and theories of contraction. Progress in Biophysics and Biophysical Chemistry, 7:255–318, 1957.
 10. A V Hill. The heat of shortening and the dynamic constants of muscle. Proceedings of the Royal Society of London. Series B-Biological Sciences, 126(843):136–195, 1938.
 11. G J C Ettema and K Meijer. Muscle contraction history: modified Hill versus an exponential decay model. Biological Cybernetics, 83(6):491–500, 2000.
 12. Michael Günther and Syn Schmitt. A macroscopic ansatz to deduce the hill relation. Journal of theoretical biology, 263(4):407–418, 2010.

13. J Denoth, E Stüssi, G Csucs, and G Danuser. Single muscle fiber contraction is dictated by inter-sarcomere dynamics. Journal of theoretical biology, 216(1):101–122, 2002.
14. I A Telley and J Denoth. Sarcomere dynamics during muscular contraction and their implications to muscle function. Journal of muscle research and cell motility, 28(1):89–104, 2007.
15. J Stålhand, A Klarbring, and G A Holzapfel. Smooth muscle contraction: mechanochemical formulation for homogeneous finite strains. Progress in biophysics and molecular biology, 96(1-3):465–481, 2008.
16. J E Baker and D D Thomas. A thermodynamic muscle model and a chemical basis for AV Hill’s muscle equation. Journal of Muscle Research & Cell Motility, 21(4):335–344, 2000.
17. J Denoth, K Gruber, M Keppler, and H Ruder. Forces and torques during sport activities with high accelerations. In S Perren and E Schneider, editors, Biomechanics: Current Interdisciplinary Research, Developments in Biomechanics, pages 663–668. Springer Netherlands, 1985.
18. K Gruber, J Denoth, E Stuessi, and H Ruder. The wobbling mass model. Biomechanics XB, 6:1095–1099, 1987.
19. M Günther, V A Sholukha, D Keßler, V Wank, and R Blickhan. Dealing with skin motion and wobbling masses in inverse dynamics. Journal of Mechanics in Medicine and Biology, 3(3/4):309–335, 2003.
20. A M Holmes and D M Andrews. The effect of leg muscle activation state and localized muscle fatigue on tibial response during impact. Journal of applied biomechanics, 22(4):275–284, 2006.

21. S Schmitt and M Günther. Human leg impact: energy dissipation of wobbling masses. Archive of Applied Mechanics, 81(7):887–897, 2011.
22. M T G Pain and J H Challis. The role of the heel pad and shank soft tissue during impacts: a further resolution of a paradox. Journal of biomechanics, 34(3):327–333, 2001.
23. M T G Pain and J H Challis. Wobbling mass influence on impact ground reaction forces: A simulation model sensitivity analysis. Journal of Applied Biomechanics, 20(3):309–316, 2004.
24. B M Nigg and W Liu. The effect of muscle stiffness and damping on simulated impact force peaks during running. Journal of biomechanics, 32(8):849–856, 1999.
25. M J R Gittoes, M A Brewin, and D G Kerwin. Soft tissue contributions to impact forces simulated using a four-segment wobbling mass model of forefoot-heel landings. Human movement science, 25(6):775–787, 2006.
26. Z Yue and J Mester. A model analysis of internal loads, energetics, and effects of wobbling mass during the whole-body vibration. Journal of biomechanics, 35(5):639–647, 2002.
27. Z Yue and J Mester. A Modal Analysis of Resonance during the Whole-Body Vibration. Studies in Applied Mathematics, 112(3):293–314, 2004.
28. J M Wakeling and B M Nigg. Modification of soft tissue vibrations in the leg by muscular activity. Journal of Applied Physiology, 90(2):412–420, 2001.

29. B M Nigg and J M Wakeling. Impact forces and muscle tuning: a new paradigm. Exercise and sport sciences reviews, 29(1):37–41, 2001.
30. K Gruber, H Ruder, J Denoth, and K Schneider. A comparative study of impact dynamics: wobbling mass model versus rigid body models. Journal of Biomechanics, 31(5):439–444, 1998.
31. A M Wilson, M P McGuigan, A Su, and A J van den Bogert. Horses damp the spring in their step. Nature, 414(6866):895–899, 2001. Comment in 414(6866):855-857.
32. J M Wakeling and B M Nigg. Soft-tissue vibrations in the quadriceps measured with skin mounted transducers. Journal of Biomechanics, 34(4):539–543, 2001.
33. M Günther, O Röhrle, D F B Haeufle, and S Schmitt. Spreading out muscle mass within a Hill-type model: a computer simulation study. Computational and mathematical methods in medicine, 2012, 2012.
34. G Piazzesi and V Lombardi. A cross-bridge model that is able to explain mechanical and energetic properties of shortening muscle. Biophysical Journal, 68(5):1966–1979, 1995.
35. T Nishizaka, H Miyata, H Yoshikawa, S Ishiwata, and Kjr. Kinoshita. Unbinding force of a single motor molecule of muscle measured using optical tweezers. Nature, 377(6546):251–254, 1995.
36. R C Woledge, N A Curtin, and E Homsher. Energetic aspects of muscle contraction. In Monographs of the Physiological Society 41, pages 1–357. Academic Press, London, 1985.

37. E V Rosenfeld. The interrelation between mechanical characteristics of contracting muscle, cross-bridge internal structure, and the mechanism of chemomechanical energy transduction. European Biophysics Journal, 41(9):733–753, 2012.
38. G Piazzesi, M Dolfi, E Brunello, L Fusi, M Reconditi, P Bianco, M Linari, and V Lombardi. The myofilament elasticity and its effect on kinetics of force generation by the myosin motor. Archives of Biochemistry and Biophysics, 552-553:108–116, 2014.
39. B Katz. The relation between force and speed in muscular contraction. The Journal of Physiology, 96:45–64, 1939.
40. H Mashima, K Akazawa, H Kushima, and K Fujii. The force-load-velocity relation and the viscous-like force in the frog skeletal muscle. Japanese Journal of Physiology, 22(1):103–120, 1972.
41. O Till, T Siebert, C Rode, and R Blickhan. Characterization of isoveLOCITY extension of activated muscle: a Hill-type model for eccentric contractions and a method for parameter determination. Journal of theoretical biology, 255(2):176–187, 2008.
42. R Rockenfeller and M Günther. Extracting low-velocity concentric and eccentric dynamic muscle properties from isometric contraction experiments. Mathematical Biosciences, 278:77–93, 2016.
43. A A Zadpoor and A A Nikooyan. Modeling muscle activity to study the effects of footwear on the impact forces and vibrations of the human body during running. Journal of biomechanics, 43(2):186–193, 2010.

44. G J C Ettema and P A Huijing. Frequency response of rat gastrocnemius medialis in small amplitude vibrations. Journal of Biomechanics, 27(8):1015–1022, 1994.
45. A F Huxley and R M Simmons. Proposed mechanism of force generation in striated muscle. Nature, 233(5321):533–538, 1971.
46. M Caruel and L Truskinovsky. Physics of muscle contraction. Reports on Progress in Physics, 81(3):036602, 2018.
47. M A Wallig, B Bolon, W M Haschek, and C G Rousseaux. Fundamentals of toxicologic pathology. Academic press, 2017.
48. M P E Wenger, L Bozec, M A Horton, and P Mesquida. Mechanical properties of collagen fibrils. Biophysical journal, 93(4):1255–1263, 2007.
49. T J Burkholder and R L Lieber. Sarcomere length operating range of vertebrate muscles during movement. Journal of Experimental Biology, 204(9):1529–1536, 2001.
50. M Reconditi. Recent improvements in small angle X-ray diffraction for the study of muscle physiology. Reports on Progress in Physics, 69(10):2709–2759, 2006.
51. A F Huxley and R Niedergerke. Structural changes in muscle during contraction. Interference microscopy of living muscle fibres. Nature, 173(4412):971–973, 1954.
52. J Hanson and H E Huxley. Structural basis of the cross-striations in muscle. Nature, 172(4377):530–532, 1953.

53. G Piazzesi, S Reconditi, M Linari, L Lucii, P Bianco, E Brunello, V Decostre, A Stewart, D B Gore, T C Irving, M Irving, and V Lombardi. Skeletal muscle performance determined by modulation of number of myosin motors rather than motor force or stroke size. Cell, 131(4):784–795, 2007.
54. Z Mártonfalvi, P Bianco, M Linari, M Caremani, A Nagy, V Lombardi, and M Kellermayer. Low-force transitions in single titin molecules reflect a memory of contractile history. Journal of Cell Science, 127(Pt 4):858–870, 2014. Figure S4c.
55. L Tskhovrebova and J Trinick. Titin and nebulin in thick and thin filament length regulation. In Parry D A D and J M Squire, editors, Fibrous Proteins: Structures and Mechanisms, volume 82 of Subcellular Biochemistry, pages 285–318. Springer, Cham, 2017.
56. K Maruyama, S Matsubara, R Natori, Y Nonomura, S Kimura, K Ohashi, F Murakami, S Handa, and G Eguchi. Connectin, an elastic protein of muscle: characterization and function. The Journal of biochemistry, 82(2):317–337, 1977.
57. Samrat Dutta, Christopher Tsiros, Sai Lavanyaa Sundar, Humra Athar, Jeffrey Moore, Brent Nelson, Matthew J Gage, and Kiisa Nishikawa. Calcium increases titin N2A binding to F-actin and regulated thin filaments. Scientific reports, 8(1):1–11, 2018.
58. K Nishikawa. Titin: a tunable spring in active muscle. Physiology, 35(3):209–217, 2020.
59. W Herzog. The multiple roles of titin in muscle contraction and force production. Biophysical reviews, 10(4):1187–1199, 2018.

60. A D Liversage, D Holmes, P J Knight, L Tskhovrebova, and J Trinick. Titin and the sarcomere symmetry paradox. Journal of molecular biology, 305(3):401–409, 2001.
61. K Nishikawa, S Dutta, M DuVall, B Nelson, M J Gage, and J A Monroy. Calcium-dependent titin–thin filament interactions in muscle: observations and theory. Journal of Muscle Research and Cell Motility, page published online, 2019.
62. J A Herzog, T R Leonard, A Jinha, and W Herzog. Titin (visco-)elasticity in skeletal muscle myofibrils. Cellular Biomechanics, 11(1):1–17, 2014.
63. Christian Rode, Tobias Siebert, Andre Tomalka, and Reinhard Blickhan. Myosin filament sliding through the Z-disc relates striated muscle fibre structure to function. Proceedings of the royal society B: biological sciences, 283(1826):20153030, 2016.
64. H E Huxley and W Brown. The low-angle X-ray diagram of vertebrate striated muscle and its behaviour during contraction and rigor. Journal of Molecular Biology, 30(2):383–434, 1967.
65. John M Squire. Symmetry and three-dimensional arrangement of filaments in vertebrate striated muscle. Journal of Molecular Biology, 90(1):153–160, 1974.
66. C Knupp, P K Luther, and J M Squire. Titin organisation and the 3D architecture of the vertebrate-striated muscle I-band. Biophysical Journal, 322(4):731–739, 2002.
67. JW Pringle. Mechano-chemical transformation in striated muscle. In

- Symposia of the Society for Experimental Biology, volume 22, page 67, 1968.
68. V Lombardi, Piazzesi G, and M Linari. Rapid regeneration of the actin-myosin power stroke in contracting muscle. Nature, 355(6361):638–641, 1992.
 69. HH Tsang, KM Tse, KY Chan, Guoxing Lu, and Alan KT Lau. Energy absorption of muscle-inspired hierarchical structure: Experimental investigation. Composite Structures, 226:111250, 2019.
 70. J J Feher. Quantitative human physiology: an introduction. Academic press, 2017.
 71. S M Mijailovich, M Prodanovic, and T C Irving. Estimation of forces on actin filaments in living muscle from x-ray diffraction patterns and mechanical data. International Journal of Molecular Sciences, 20(23):6044, 2019.
 72. R Craig and R Padrón. Molecular structure of the sarcomere. Myology, 3:129–144, 2004.
 73. K Oshima, Y Takezawa, Y Sugimoto, M Kiyotoshi, and K Wakabayashi. MODELING ANALYSIS OF MYOSIN-BASED MERIDIONAL X-RAY REFLECTIONS FROM FROG SKELETAL MUSCLES IN RELAXED AND CONTRACTING STATES . In Sugi H, editor, MOLECULAR AND CELLULAR ASPECTS OF MUSCLE CONTRACTION, pages 243–249. Kluwer Academic / Plenum Publishers, New York, 2003.

74. J T Mortimer, R Magnusson, and I Petersén. Conduction velocity in ischemic muscle: effect on EMG frequency spectrum. American Journal of Physiology, 219(5):1324–1329, 1970.
75. A Chervu, W S Moore, E Homsher, and W J Quinones-Baldrich. Differential recovery of skeletal muscle and peripheral nerve function after ischemia and reperfusion. Journal of Surgical Research, 47(1):12–19, 1989.
76. R Labbe, T Lindsay, and P M Walker. The extent and distribution of skeletal muscle necrosis after graded periods of complete ischemia. Journal of vascular surgery, 6(2):152–157, 1987.
77. Z Turóczi, P Arányi, Á Lukáts, D Garbaisz, G Lotz, L Harsány, and Szijártó A. Muscle fiber viability, a novel method for the fast detection of ischemic muscle injury in rats. PLoS One, 9(1):e84783, 2014.
78. J S Fish, N H McKee, W M Kuzon Jr, and M J Plyley. The effect of hypothermia on changes in isometric contractile function in skeletal muscle after tourniquet ischemia. The Journal of hand surgery, 18(2):210–217, 1993.
79. M M Lorist, D Kernell, T F Meijman, and I Zijdewind. Motor fatigue and cognitive task performance in humans. The Journal of physiology, 545(1):313–319, 2002.
80. S A Edgley and A P Winter. Different effects of fatiguing exercise on corticospinal and transcallosal excitability in human hand area motor cortex. Experimental brain research, 159(4):530–536, 2004.
81. L A C Kallenberg, E Schulte, C Disselhorst-Klug, and H J Hermens.

- Myoelectric manifestations of fatigue at low contraction levels in subjects with and without chronic pain. Journal of Electromyography and Kinesiology, 17(3):264–274, 2007.
82. D G Allen and H Westerblad. Role of phosphate and calcium stores in muscle fatigue. Journal of Physiology, 536(3):657–665, 2001.
83. T Siebert, O Till, and R Blickhan. Work partitioning of transversally loaded muscle: experimentation and simulation. Computer Methods in Biomechanics and Biomedical Engineering, 17(3):217–229, 2014.
84. Jan Celichowski. Motor units of medial gastrocnemius muscle in the rat during the fatigue test. ii. changes in the time course of sequential tetani of fatigue test. Acta Neurobiol. Exp, 52:99–111, 1992.
85. K B MacDougall, A N Devrome, A M Kristensen, and B R MacIntosh. Force-frequency relationship during fatiguing contractions of rat medial gastrocnemius muscle. Scientific Reports, 10:11575, 2020.
86. A A Webb, B Kerr, T Neville, S Ngan, and H Assem. Kinematics and ground reaction force determination: a demonstration quantifying locomotor abilities of young adult, middle-aged, and geriatric rats. JoVE (Journal of Visualized Experiments), (48):e2138, 2011.
87. H Witte, J Biltzinger, R Hackert, N Schilling, M Schmidt, C Reich, and M S Fischer. Torque patterns of the limbs of small therian mammals during locomotion on flat ground. The Journal of Experimental Biology, 205(Pt 9):1339–1353, 2002.

88. A Schmidt and A R Biknevičius. Structured variability of steady-speed locomotion in rats. The Journal of Experimental Biology, 217(Pt 8):1402–1406, 2014.
89. Michael P Greenwood, Mingkwan Greenwood, Elena V Romanova, Andre S Mecawi, Alex Paterson, Olivera Sarenac, Nina Japundžić-Žigon, José Antunes-Rodrigues, Julian FR Paton, Jonathan V Sweedler, et al. The effects of aging on biosynthetic processes in the rat hypothalamic osmoregulatory neuroendocrine system. Neurobiology of aging, 65:178–191, 2018.
90. Elza Maria Santos da Silveira, Adarly Kroth, Maria do Carmo Quevedo Santos, Thaisla Cristiane Borella da Silva, D Silveira, Ana Paula Konzen Riffel, Taina Scheid, Márcia Trapp, and Wania Aparecida Partata. Age-related changes and effects of regular low-intensity exercise on gait, balance, and oxidative biomarkers in the spinal cord of Wistar rats. Brazilian Journal of Medical and Biological Research, 52(7), 2019.
91. H Stark and N Schilling. A novel method of studying fascicle architecture in relaxed and contracted muscles. Journal of Biomechanics, 43(15):2897–2890, 2010.
92. K B Christensen, M Günther, S Schmitt, and T Siebert. Strain in shock-loaded skeletal muscle and the time scale of muscular wobbling mass dynamics. Scientific Reports, 7(1):13266, 2017.
93. Paddleford, R R and Erhardt, W. Anästhesie bei Kleinieren. Schattauer, Hölderlinstraße 3, 70174, Stuttgart, 1992.

94. K B Christensen, M Günther, S Schmitt, and T Siebert. Cross-bridge mechanics estimated from skeletal muscles' work-loop responses to impacts in legged locomotion. Scientific reports, 11(1):1–12, 2021.
95. C J Zuurbier, J W Heslinga, M B E Lee-de Groot, and W J Van der Laarse. Mean sarcomere length-force relationship of rat muscle fibre bundles. Journal of Biomechanics, 28(1):83–87, 1995.
96. B A Mobley and B R Eisenberg. Sizes of components in frog skeletal muscle measured by methods of stereology. The Journal of General Physiology, 66(1):31–45, 1975.
97. R D Mateja, M L Greaser, and P P de Tombe. Impact of titin isoform on length dependent activation and cross-bridge cycling kinetics in rat skeletal muscle. Biochimica et Biophysica Acta, 1833(4):804–811, 2013. Figure 2B,C.
98. T Irving, Y Wu, T Bekyarova, G P Farman, N Fukuda, and H Granzier. Thick-filament strain and interfilament spacing in passive muscle: effect of titin-based passive tension. Biophysical Journal, 100(6):1499–1508, 2011.
99. C J Zuurbier and P A Huijing. Changes in geometry of actively shortening unipennate rat gastrocnemius muscle. Journal of Morphology, 218(2):167–180, 1993.
100. E B Cady, D A Jones, J Lynn, and D J Newham. Changes in force and intracellular metabolites during fatigue of human skeletal muscle. The Journal of Physiology, 418(1):311–325, 1989.
101. Russ D W and J A Kent-Braun. Sex differences in human

- skeletal muscle fatigue are eliminated under ischemic conditions. Journal of Applied Physiology, 94(6):2414–2422, 2003.
102. I Dobbie, M Linari, G Piazzesi, M Reconditi, N Koubassova, M A Ferenczi, V Lombardi, and M Irving. Elastic bending and active tilting of myosin heads during muscle contraction. Nature, 396(6709):383–387, 1998.
 103. M Linari, I Dobbie, M Reconditi, N Koubassova, M Irving, G Piazzesi, and V Lombardi. The stiffness of skeletal muscle in isometric contraction and rigor: the fraction of myosin heads bound to actin. Biophysical Journal, 74(5):2459–2473, 1998.
 104. V Decostre, P Bianco, V Lombardi, and G Piazzesi. Effect of temperature on the working stroke of muscle myosin. Proceedings of the National Academy of Sciences of the USA, 102(39):13927–13932, 2005.
 105. P L Powell, R R Roy, P Kanim, M A Bello, and V R Edgerton. Predictability of skeletal muscle tension from architectural determinations in guinea pig hindlimbs. Journal of Applied Physiology, 57(6):1715–1721, 1984.
 106. C M Eng, L H Smallwood, M P Rainiero, M Lahey, S R Ward, and R L Lieber. Scaling of muscle architecture and fiber types in the rat hindlimb. The Journal of Experimental Biology, 211(Pt 14):2336–2345, 2008.
 107. V A Kadhiresan, C A Hassett, and J A Faulkner. Properties of single motor units in medial gastrocnemius muscles of adult and old rats. The Journal of Physiology, 493(Pt 2):543–552, 1996.

108. G Piazzesi, L Lucii, and V Lombardi. The size and the speed of the working stroke of muscle myosin and its dependence on the force. The Journal of Physiology, 545(Pt 1):145–151, 2002.
109. C Rode, T Siebert, and R Blickhan. Titin-induced force enhancement and force depression: a ‘sticky-spring’ mechanism in muscle contractions? Journal of theoretical biology, 259(2):350–360, 2009.
110. K Maruyama, R Natori, and Y Nonomura. New elastic protein from muscle. Nature, 262(5563):58–60, 1976.
111. K Tawada and K Sekimoto. Protein friction exerted by motor enzymes through a weak-binding interaction. Journal of theoretical biology, 150(2):193–200, 1991.
112. K Tawada and K Sekimoto. A physical model of ATP-induced actin-myosin movement in vitro. Biophysical journal, 59(2):343–356, 1991.
113. M E Fisher and A B Kolomeisky. The force exerted by a molecular motor. Proceedings of the National Academy of Sciences, 96(12):6597–6602, 1999.
114. H Suda. Origin of friction derived from rupture dynamics. Langmuir, 17:6045–6047, 2001.
115. V Bormuth, V Varga, J Howard, and E Schäffer. Protein friction limits diffusive and directed movements of kinesin motors on microtubules. Science, 325(5942):870–873, 2009.
116. V Lombard, G Piazzesi, M A Ferenczi, H Thirlwell, I Dobbie, and M Irving. Elastic distortion of myosin heads and repriming of the working stroke in muscle. Nature, 374(6522):553–555, 1995.

117. T Kardel. Niels Stensen's geometrical theory of muscle contraction (1667): a reappraisal. Journal of Biomechanics, 23(10):953–965, 1990.
118. J Swammerdam. Earliest known experimental evidence for volume constancy of skeletal muscle during contraction. after [121]; first published by quotation not before 1669, see also: [117], 1663.
119. N Stensen (Stenonis). Elementorum Myologiae Specimen, seu Muscili Descriptio Geometrica volume 2. Stellae, Florence, 1667. pp. 61-111; see [117].
120. R J Baskin and P J Paolini. Volume change and pressure development in muscle during contraction. American Journal of Physiology, 213(4):1025–1030, 1967.
121. T A McMahon. Muscles, Reflexes, and Locomotion. Princeton University Press, Princeton, NJ, 1984. Table 9.7.
122. I V Ogneva, D V Lebedev, and B S Shenkman. Transversal stiffness and Young's modulus of single fibers from rat soleus muscle probed by atomic force microscopy. Biophysical Journal, 98(3):418–424, 2010.
123. D R Wilkie. The relation between force and velocity in human muscle. The Journal of Physiology, 110(3-4):249–280, 1949.
124. A V Hill. The abrupt transition from rest to activity in muscle. Proceedings of the Royal Society B, 136(884):399–420, 1949.
125. A V Hill. The series elastic component of muscle. Proceedings of the Royal Society B, 137:273–280, 1950.
126. R F Ker. Mechanics of tendon, from an engineering perspective. International Journal of Fatigue, 29(6):1001–1009, 2007.

127. R F Ker. Dynamic tensile properties of the plantaris tendon of sheep (*Ovis aries*). The Journal of Experimental Biology, 93:283–302, 1981.
128. M B Bennett, R F Ker, N J Dimery, and R McN Alexander. Mechanical properties of various mammalian tendons. Journal of Zoology, 209:537–548, 1986.
129. C M Pollock and R E Shadwick. Relationship between body mass and biomechanical properties of limb tendons in adult mammals. American Journal of Physiology, 266(3 Pt 2):R1016–1021, 1994.
130. G D Muir and I Q Whishaw. Complete locomotor recovery following corticospinal tract lesions: measurement of ground reaction forces during overground locomotion in rats. Behavioural brain research, 103(1):45–53, 1999.
131. J Denoth, K Gruber, M Keppler, and H Ruder. Forces and torques during sport activities with high accelerations. In S Perren and E Schneider, editors, Biomechanics: Current Interdisciplinary Research, Developments in Biomechanics, pages 663–668. Springer Netherlands, 1985.
132. S W Lipfert, M Günther, D Renjewski, and A Seyfarth. Impulsive ankle push-off powers leg swing in human walking. The Journal of Experimental Biology, 217(Pt 8):1218–1228, 2014.
133. J J De Koning, H F van der Molen, R D Woittiez, and P A Huijing. Functional characteristics of rat gastrocnemius and tibialis anterior muscles during growth. Journal of Morphology, 194(1):75–84, 1987.
134. T Weis-Fogh and R McN Alexander. The sustained power output obtainable from striated muscle. In T J Pedley, editor,

- Scale Effects in Animal Locomotion, pages 511–526. Academic Press, London, 1977. p. 518.
135. M Schoenberg. Geometrical factors influencing muscle force development. II. Radial forces. Biophysical Journal, 30(1):69–78, 1980.
 136. J A Rivas-Pardo, E C Eckels, I Popa, P Kosuri, W A Linke, and J M Fernández. Work done by titin protein folding assists muscle contraction. Cell Reports, 14(6):1339–1347, 2016.
 137. M Krüger and W A Linke. The giant protein titin: a regulatory node that integrates myocyte signaling pathways. Journal of Biological Chemistry, 286(12):9905–9912, 2011.
 138. P Tonino, B Kiss, J Strom, M Methawasin, J E Smith III, J Kolb, S Labeit, and H Granzier. The giant protein titin regulates the length of the striated muscle thick filament. Nature Communications, 8(1):1041, 2017. Figure 4c.
 139. A Freiburg, K Trombitas, W Hell, O Cazorla, F Fougousse, T Centner, B Kolmerer, C Witt, J S Beckmann, C C Gregorio, H Granzier, and S Labeit. Series of exon-skipping events in the elastic spring region of titin as the structural basis for myofibrillar elastic diversity. Circulation Research, 86(11):1114–1121, 2000.
 140. M Lakie and K S Campbell. Muscle thixotropy—where are we now? Journal of Applied Physiology, 126(6):1790–1799, 2019.
 141. L E Ford, A F Huxley, and R M Simmons. Tension responses to sudden length change in stimulated frog muscle fibres near slack length. The Journal of Physiology, 269(2):441–515, 1977.

142. M Irving, V Lombardi, G Piazzesi, and M A Ferenczi. Myosin head movements are synchronous with the elementary force-generating process in muscle. Nature, 357(6374):156–158, 1992.
143. M Kaya and H Higuchi. Nonlinear elasticity and an 8-nm working stroke of single myosin molecules in myofilaments. Science, 329(5992):686–689, 2010.
144. I Adamovic, S M Mijailovich, and M Karplus. The elastic properties of the structurally characterized myosin II S2 subdomain: a molecular dynamics and normal mode analysis. Biophysical Journal, 94(10):3779–3789, 2008.
145. M Linari, G Piazzesi, and V Lombardi. The effect of myofilament compliance on kinetics of force generation by myosin motors in muscle. Biophysical Journal, 96(2):583–592, 2009.
146. B Colombini, M Nocella, M A Bagni, P J Griffiths, and G Cecchi. Is the cross-bridge stiffness proportional to tension during muscle fiber activation? Biophysical Journal, 98:2582–2590, 2010.
147. M A Bagni, B Colombini, H Amenitsch, S Bernstorff, C C Ashley, G Rapp, and P J Griffiths. Frequency-dependent distortion of meridional intensity changes during sinusoidal length oscillations of activated skeletal muscle. Biophysical Journal, 80(6):2809–2822, 2001.
148. A Ishijima, H Kojima, H Higuchi, Y Harada, T Funatsu, and T Yanagida. Multiple- and single-molecule analysis of the actomyosin motor by nanometer-picoNewton manipulation with a microneedle: unitary steps and forces. Biophysical Journal, 70(1):383–400, 1996.

149. A Tomalka, C Rode, J Schumacher, and T Siebert. The active force-length relationship is invisible during extensive eccentric contractions in skinned skeletal muscle fibres. Proceedings of the Royal Society of London B, 284(1854):20162497, 2017.
150. J J Woods and B Bigland-Ritchie. Linear and non-linear surface EMG/-force relationships in human muscles. An anatomical/functional argument for the existence of both. American journal of physical medicine, 62(6):287–299, 1983.
151. S Park-Holohan, M Linari, M Reconditi, L Fusi, E Brunello, M Irving, M Dolfi, V Lombardi, TG West, NA Curtin, et al. Mechanics of myosin function in white muscle fibres of the dogfish, *Scyliorhinus canicula*. The Journal of physiology, 590(8):1973–1988, 2012.
152. G Wang and M Kawai. Effect of temperature on elementary steps of the cross-bridge cycle in rabbit soleus slow-twitch muscle fibres. The Journal of Physiology, 531(1):219–34, 2001.
153. C J Barclay. Energetics of contraction. Comprehensive Physiology, 5:961–995, 2015.
154. P Mettikolla, N Calander, R Luchowski, I Gryczynski, Z Gryczynski, and J Borejdo. Observing cycling of a few cross-bridges during isometric contraction of skeletal muscle. Cytoskeleton (Hoboken, N.J.), 67(6):400–411, 2010.
155. R Müller, D F B Haeufle, and R Blickhan. Preparing the leg for ground contact in running: the contribution of feed-forward and visual feedback. The Journal of Experimental Biology, 218(Pt 3):451–457, 2015.

156. G D Muir and I Q Wishaw. Ground reaction forces in locomoting hemiparkinsonian rats: a definitive test for impairments and compensations. Experimental Brain Research, 126(3):307–314, 1999.
157. B Colombini, M A Bagni, and P J Griffiths. Effects of solution tonicity on crossbridge properties and myosin lever arm disposition in intact frog muscle fibres. The Journal of Physiology, 578(1):337–346, 2007.
158. M A Bagni, G Cecchi, and B Colombini. Crossbridge properties investigated by fast ramp stretching of activated frog muscle fibres. The Journal of Physiology, 565(1):261–268, 2005.
159. Kirsten Albracht, A Arampatzis, and V Baltzopoulos. Assessment of muscle volume and physiological cross-sectional area of the human triceps surae muscle in vivo. Journal of biomechanics, 41(10):2211–2218, 2008.
160. M G Urbanchek, E B Picken, L K Kalliainen, and W M Kuzon Jr. Specific force deficit in skeletal muscles of old rats is partially explained by the existence of denervated muscle fibers. The Journals of Gerontology Series A: Biological Sciences and Medical Sciences, 56(5):B191–B197, 2001.
161. Geoffrey G Handsfield, Craig H Meyer, Joseph M Hart, Mark F Abel, and Silvia S Blemker. Relationships of 35 lower limb muscles to height and body mass quantified using mri. Journal of biomechanics, 47(3):631–638, 2014.
162. R M Alexander. Tendon elasticity and muscle function. Comparative biochemistry and physiology part a: Molecular & integrative physiology, 133(4):1001–1011, 2002.

163. T Siebert, H R C Screen, and C Rode. Computational modelling of muscle, tendon, and ligaments biomechanics. In Computational Modelling of Biomechanics and Biotribology in the Musculoskeletal System, pages 155–186. Elsevier, 2021.
164. E Carrera, G Giunta, and M Petrolo. Beam structures: classical and advanced theories. John Wiley & Sons, 2011.
165. K S Pakhare, R P Shimpi, and P J Guruprasad. Buckling analysis of thick isotropic shear deformable beams. In Recent Advances in Theoretical, Applied, Computational and Experimental Mechanics, pages 59–65. Springer, 2020.
166. G R Cowper. The shear coefficient in Timoshenko’s beam theory. 1966.
167. R W Frischholz and K P Spinnler. Class of algorithms for real-time subpixel registration. In Computer Vision for Industry, volume 1989, pages 50–59. International Society for Optics and Photonics, 1993.
168. G F Elliott, J Lowy, and C R Worthington. An X-ray and light-diffraction study of the filament lattice of striated muscle in the living state and in rigor. Journal of Molecular Biology, 6(4):295–305, 1963.
169. I. Matsubara and G.F. Elliott. X-ray diffraction studies on skinned single fibres of frog skeletal muscle. Journal of Molecular Biology, 72(3):657–669, 1972.
170. P W Brandt, E Lopez, J P Reuben, and H Grundfest. The relationship between myofilament packing density and sarcomere length in frog striated muscle. The Journal of Cell Biology, 33(2):255–263, 1967.

171. T Kurg, R H Stinson, and B M Millman. X-ray diffraction from striated muscles and nerves in normal and dystrophic mice. Muscle & Nerve, 5(3):238–246, 1982.
172. M A Goldstein, L H Michael, J P Schroeter, and R L Sass. Z band dynamics as a function of sarcomere length and the contractile state of muscle. Federation of American Societies for Experimental Biology, 1(2):133–142, 1987.
173. B M Millman. The filament lattice of striated muscle. Physiological Reviews, 78(2):359–391, 1998.
174. J W Heslinga and P A Huijing. Effects of growth on architecture and functional characteristics of adult rat gastrocnemius muscle. Journal of Morphology, 206(1):119–132, 1990.

Declaration of agreement(s)

Einverständniserklärung

Die Co-Autoren der in dieser Dissertation verwendeten Manuskripte (Studie 1 und Studie 2) sind sowohl über die Nutzung, als auch über die entsprechend angegebenen Eigenanteile informiert und stimmen dem zu.

”Ich bin mit der Verwendung der Publikation/-en (nachstehend zitiert), bei denen Ich als Mitautor erscheine, im Rahmen der Dissertationsschrift des Promovenden (Kasper B. Christensen), und der damit einhergehenden Erklärung zum Eigenanteil, einverstanden”.

- Christensen, K. B., Günther, M., Schmitt, S. & Siebert, T. Strain in shock-loaded skeletal muscle and the time scale of muscular wobbling mass dynamics. Scientific Reports, 7 (1): 13266, 2017. DOI: 10.1038/s41598-017-13630-7
- Christensen, K. B., Günther, M., Schmitt, S. & Siebert, T. Cross-bridge mechanics estimated from skeletal muscles' work-loop responses to impacts in legged locomotion. Scientific Reports, 11 (1): 23638, 2021. DOI: 10.1038/s41598-021-02819-6

9.17.2021 T. Siebert

gez. Prof. Dr. Tobias Siebert

Einverständniserklärung

Die Co-Autoren der in dieser Dissertation verwendeten Manuskripte (Studie 1 und Studie 2) sind sowohl über die Nutzung, als auch über die entsprechend angegebenen Eigenanteile informiert und stimmen dem zu.

”Ich bin mit der Verwendung der Publikation/-en (nachstehend zitiert), bei denen Ich als Mitautor erscheine, im Rahmen der Dissertationsschrift des Promovenden (Kasper B. Christensen), und der damit einhergehenden Erklärung zum Eigenanteil, einverstanden”.

- Christensen, K. B., Günther, M., Schmitt, S. & Siebert, T. Strain in shock-loaded skeletal muscle and the time scale of muscular wobbling mass dynamics. Scientific Reports, 7 (1): 13266, 2017. DOI: 10.1038/s41598-017-13630-7
- Christensen, K. B., Günther, M., Schmitt, S. & Siebert, T. Cross-bridge mechanics estimated from skeletal muscles’ work-loop responses to impacts in legged locomotion. Scientific Reports, 11 (1): 23638, 2021. DOI: 10.1038/s41598-021-02819-6



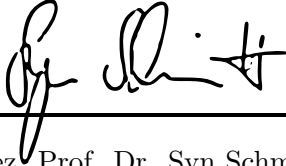
gez. Dr. Michael Günther

Einverständniserklärung

Die Co-Autoren der in dieser Dissertation verwendeten Manuskripte (Studie 1 und Studie 2) sind sowohl über die Nutzung, als auch über die entsprechend angegebenen Eigenanteile informiert und stimmen dem zu.

”Ich bin mit der Verwendung der Publikation/-en (nachstehend zitiert), bei denen Ich als Mitautor erscheine, im Rahmen der Dissertationsschrift des Promovenden (Kasper B. Christensen), und der damit einhergehenden Erklärung zum Eigenanteil, einverstanden”.

- Christensen, K. B., Günther, M., Schmitt, S. & Siebert, T. Strain in shock-loaded skeletal muscle and the time scale of muscular wobbling mass dynamics. Scientific Reports, 7 (1): 13266, 2017. DOI: 10.1038/s41598-017-13630-7
- Christensen, K. B., Günther, M., Schmitt, S. & Siebert, T. Cross-bridge mechanics estimated from skeletal muscles’ work-loop responses to impacts in legged locomotion. Scientific Reports, 11 (1): 23638, 2021. DOI: 10.1038/s41598-021-02819-6



gez. Prof. Dr. Syn Schmitt

Declaration

I hereby declare, that this dissertation is solely my original work. I have used only the sources and materials indicated and have not received any unauthorised assistance from others. All quotations from other works as well as paraphrases or summaries of other works have been identified as such and properly acknowledged in the dissertation.

Ich erkläre, dass ich die Arbeit selbständig erstellt und nur die angegebenen Hilfsmittel verwendet habe. Alle Stellen, die dem Wortlaut oder dem Sinn nach anderen Werken, gegebenenfalls auch elektronischen Medien, entnommen sind, sind von mir durch Angabe der Quelle als Entlehnung kenntlich gemacht.

Stuttgart, November, 2021



Kasper B. Christensen,

November 12, 2021